Univerzita Karlova v Praze
Matematicko-fyzikální fakulta

DIPLOMOVÁ PRÁCE

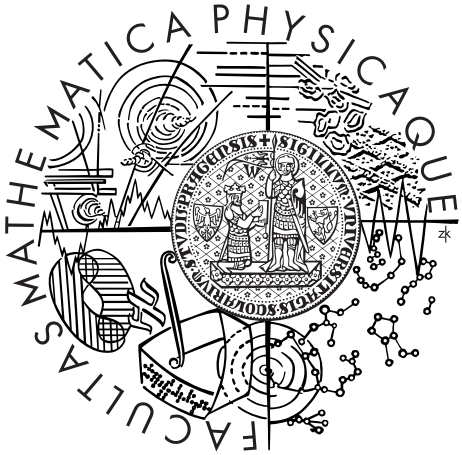

Pavel Zháňal

Studium fázových transformací ve slitinách Ti

Katedra fyziky materálů

Vedoucí diplomové práce: RNDr. Petr Harcuba
Studijní program: Fyzika
Studijní obor: Fyzika kondenzovaných soustav a materiálů

Praha 2014

Charles University in Prague
Faculty of Mathematics and Physics

MASTER THESIS

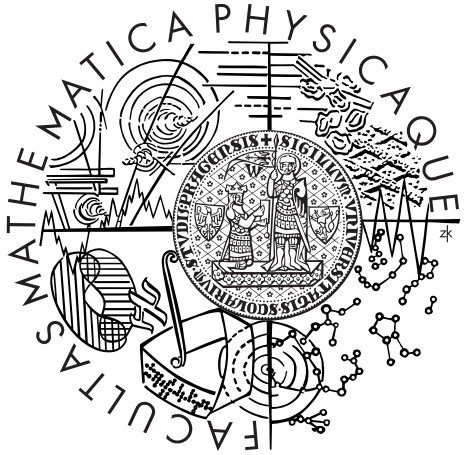

Pavel Zháňal

Study of Phase Transformations in Ti Alloys

Department of Physics of Materials

Supervisor of the master thesis: RNDr. Petr Harcuba
Study programme: Physics
Specialization: Physics of Condensed Matter and Materials

Prague 2014

Acknowledgements

In the first place, I would like to express my gratitude to my supervisor, RNDr. Petr Harcuba for his support of my work, his help and encouragement during my studies. My sincere thanks are also extended to my colleagues from the Department of Physics of Materials for their help, which made me understand many interesting problems investigated in the field of material research. Especially I would like to mention Mgr. Jana Šmilauerová, whose advices helped me a lot with completing this work. I have to appreciate Mgr. Michal Hájek, Ph.D. and Mgr. Josef Veselý, Ph.D. for their work on creating control program for measurement of electrical resistance at cryogenic temperatures. I am also thankfull to Doc. RNDr. Bohumil Smola, CSc. for his help during TEM observations.

I declare that I carried out this master thesis independently, and only with the cited sources, literature and other professional sources.

I understand that my work relates to the rights and obligations under the Act No. 121/2000 Coll., the Copyright Act, as amended, in particular the fact that the Charles University in Prague has the right to conclude a license agreement on the use of this work as a school work pursuant to Section 60 paragraph 1 of the Copyright Act.

In Prague date ..... Pavel Zháňal .....

Název práce: Studium fázových transformací ve slitinách Ti

Autor: Pavel Zháňal

Katedra: Katedra fyziky materiálů

Vedoucí diplomové práce: RNDr. Petr Harcuba, Katedra fyziky materiálů

Abstrakt: V předložené práci byly prostřednictvím měření elektrického odporu studovány fázové transformace probíhající při tepelném zpracování metastabilní β slitiny Ti-15Mo. Výchozí materiál byl podroben rozpouštěcímu žíhání nad teplotou β-přechodu a následně zakalen do vody. Mikrostruktura takto připraveného materiálu se skládá z metastabilní β matrice a částic ω fáze. Během měření elektrického odporu in-situ při ohřevu ve speciálně upravené peci byly zjištěny význačné teploty indikující postupně probíhající fázové transformace. Závislost elektrického odporu na teplotě se během ohřevu mění mezi rostoucí a klesající podle probíhající fázové transformace. Tyto změny byly pozorovány při teplotách 225, 356 a 560 °C. Tyto transformace byly dále podrobně studovány měřením elektrického odporu různě tepelně zpracovaných vzorků. Pro kontrolu vývoje mikrosktruktury materiálu byla použita transmisní a skenovací elektronová mikroskopie. Mechanické vlastnosti byly charakterizovány pomocí měření mikrotvrdosti. Výsledky těchto měření umožnily identifikovat typy a sled fázových transformací probíhajících ve studovaném materiálu.

Klíčová slova: metastabilní slitina β Ti, β fáze, ω fáze, měření elektrického odporu, fázové transformace

Title: Study of Phase Transformations in Ti Alloys

Author: Pavel Zháňal

Department: Department of Physics of Materials

Supervisor: RNDr. Petr Harcuba, Department of Physics of Materials

Abstract:

In this work phase transformations in metastable β Ti-15Mo alloy were studied using electrical resistivity measurements. The alloy was subjected to a solution treatment at a temperature higher than β-transus and quenched in water. In this condition, the microstructure of Ti-15Mo alloy consists of a metastable β-matrix and ω phase particles. During in-situ electrical resistivity measurement in a specially designed furnace, significant temperature points which indicate phase transformations in the material were detected. The dependence of electrical resistivity on the temperature changes during heating between increasing and decreasing according to the ongoing phase transformation. The changes were observed at temperatures 225, 356 and 560 °C. A further study of these phase transformations using electrical resistivity measurements was performed on various heat treated specimens. In order to control the microstructure evolution in the material, scanning and transmission electron microscopy was used. Mechanical properties were studied using Vickers microhardness testing. The obtained results serve to identify the type and sequence of phase transformations which take place in the Ti-15Mo alloy.

Keywords: metastable β Ti alloy, β phase, ω phase, electrical resistance measurement, phase transformations

Contents

Introduction

The titanium was discovered by the British reverend William Gregor in 1791. He examined the magnetic sand from the local river and isolated "black sand" now known as "ilmenite". He was able to produce impure oxide of new element. He named it "mechanite". Independently on that the Berlin chemist Martin Heinrich Klaproth isolated titanium oxide from a mineral, now known as “rutile”. The name for the material was provided to him by Greek mythology from the children of Uranos and Gaia, the Titans. They were detained in captivity in the earthy crust, similar to the hard to extract ore – hence he named it Titanium. The metal was isolated more than 100 years later. The first alloys were developed in the late 1940’s in the USA. Today, a large number of titanium alloys expanded into many industrial applications.

Titanium and its alloys stand out primarily due to their high specific strength and excellent corrosion resistance. Also they have just half the density of steels and Ni-based superalloys. Thanks to that the alloys were successfully used in the aerospace and chemical industry. But we can see increased application of titanium also in other markets such as architecture, chemical processing, medicine, power generation, marine and offshore, sports and leisure, and transportation [1]. The only disadvantage, which hinders wider use of titanium, is relatively high cost of it, which is caused by difficult process of preparation.

Titanium alloy with 15 wt. % of molybdenum was studied in this work. This alloy was selected because of its particular significance in the development of new biomaterials. The most used titanium alloy Ti-6Al-4V consist of aluminium and vanadium ions, which can cause some health problems. It is known that aluminum ions cause neurological disorders, and vanadium ions are associated with enzymatic disturbers, among other problems [2]. Ti-Mo alloys were studied by Ho et al. and their studies were presented in papers [3] and [4]. These works showed that Ti-15Mo alloy has elasticity modulus smaller than the commercially pure Ti (CP titanium) and Ti-6Al-4V, but higher than Ti-7.5Mo alloy. However the Ti-15Mo alloy showed better value of corrosion potential then Ti-7.5Mo.

Ti-15Mo stands out among the Ti-Mo system alloys not only due to its excellent corrosion resistance but also its good combination of mechanical properties such as fatigue, hardness, and wear resistance.

This thesis is divided into 5 chapters. Chapter 1 characterizes titanium and provide informations on its alloys. Various phases that can be found in titanium alloys and conditions of their occurrence are discussed. In this chapter, the most important phase transformations are also described. Chapter 2 describes the use and basic physical properties of the studied alloy. Furthermore, it thoroughly describes used experimental methods. Aims of the work are summarized in Chapter 3. The next chapter presents the results and discussion of the findings obtained in the research. It deals with detection of phase transformations occurring in the material, their characterization depending on their influence on electrical resistance of the alloy. Finally, Chapter 5 concludes the results of the study and introduces the future investigations.

1. Titanium and Titanium alloys

1.1 Titanium

1.1.1 Properties

Titanium is the ninth most plentiful element and the fourth most abundant structural metal [1]. It has atomic number 22 and belongs to Group 4 of the periodic table of elements. It is a lustrous transition metal with a silver color, low density, high strength and high corrosion resistance. In nature it occurs in five isotopes, ^{46}Ti through ^{50}Ti, with ^{48}Ti being the most abundant (73.8%) [5].

In the nature, titanium is always bonded with other elements. Titanium usually occurs in mineral sands containing rutile (TiO_2) or ilmenite ($FeTiO_3$). Titanium dioxide is a very versatile white pigment used in paint, paper and plastic and consumes most of world production of titanium [1]. Titanium is produced commercially from these two ores by the Kroll process, which is complex and expensive bath procedure. The process consists of following steps [6]:

The first reaction is chlorination, which is done in this way

$$TiO_2 + 2Cl_2 + C \rightarrow TiCl_4 + CO_2 \tag{1.1}$$

or, thus,

$$TiO_2 + 2Cl_2 + 2C \rightarrow TiCl_4 + 2CO. \tag{1.2}$$

Next the destilation follows, because $TiCl_4$ formed by chlorination needs to be cleaned. At lower temperatures the impurities such as CO and CO_2 are removed. At higher temperatures titanium tetrachloride is cleaned from the $SiCl_4$ and $SnCl_4$. Such material is stored under an inert gas atmosphere for further use.

As the next step, the purified $TiCl_4$ is inserted into reactor filled with inert gas and metallic Mg. Then follows the heating to 800-850 °C to drive following reduction reaction:

$$TiCl_4 + 2Mg \rightarrow Ti + 2MgCl_2. \tag{1.3}$$

This actually occurs in two steps as follows:

$$TiCl_4 + Mg \rightarrow TiCl_2 + MgCl_2, \tag{1.4}$$

followed by

$$TiCl_2 + Mg \rightarrow Ti + MgCl_2. \tag{1.5}$$

The titanium obtained by this process is quite pure. However, it occurs as a mixture of pure metal and $MgCl_2$. Most of $MgCl_2$ is removed continually as the Kroll reaction proceeds, but there is some residual amount that is removed later. Titanium produced this way has sponge-like appearance. That is the reason, why it is called sponge. The last stage in the production is crushing and sizing of the sponge to produce granules of metallic titanium. The size of the granules depends on the final product that is being produced. Coarser granules (up to 2.5 cm) are used for CP titanium and for standard grades of most alloys, but for high performance applications, such as aircraft engines, smaller size of granules (up to 1 cm) are typically required [6].

Application potential of titanium and its alloys is limited by high reactivity of titanium with oxygen. Limiting temperature for usage of titanium alloys is about 600 °C [6].

1.1.2 Structure

Titanium is polymorphic, which means it can occur in more than one phase. Phase formation depends on several conditions, such as temperature, pressure, amount of alloying elements or cooling rate. The phases can be divided into equilibrium (stable) and non-equilibrium (metastable). The stable phase is defined as the state with the lowest Gibbs free energy (G) at specific conditions. However, there are configurations that correspond to local minima of G but do not have the lowest possible value of G. These conditions are called metastable. They can be reached by displacive transformations (shearing, shuffling), when high heating or cooling rates are used. The metastable phases will transform into stable ones at specific conditions after sufficient amount of time [7].

At room temperature, pure titanium crystallizes in a hexagonal close packed structure (hcp), which is known as α phase. Temperature 882 °C corresponds to an allotropic phase transformation (so called β-transus). Above this temperature, the structure transforms into a body-centered cubic (bcc). The temperature of the β-transus for titanium alloys depends on the type and solute content of alloying elements.

The unit cell of α phase with hcp structure along with the room temperature lattice parameters $a = 2.95$ Å and $c = 4.68$ Å is shown in Fig. 1.1. The c/a ratio for pure α titanium is therefore 1.587, which is smaller than ideal ratio 1.633 for hcp.

Fig. 1.2 shows the unit cell of β phase with bcc structure. Its lattice parameter is $a = 3.32$ Å for pure titanium at 900 °C. The most densely packed lattice planes and directions are indicated in Figures 1.1 and 1.2. For hcp structure these planes are basal (0001), prismatic $(10\bar{1}0)$ and pyramidal $(\bar{1}011)$. For bcc structure it is a system of six planes (110).

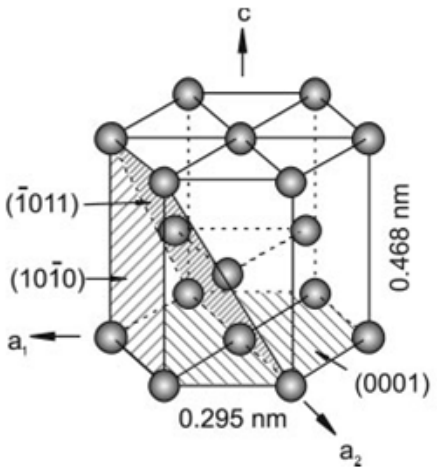

Figure 1.1: Unit cell of α phase [6]

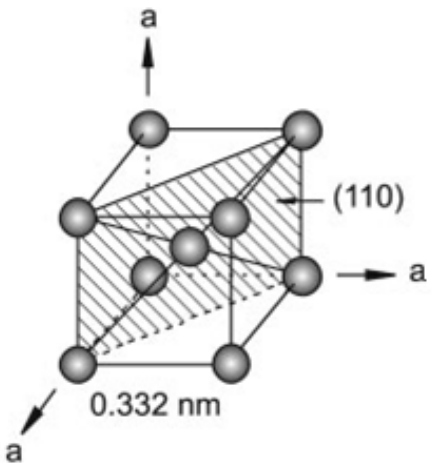

Figure 1.2: Unit cell of β phase [6]

Mechanical properties of the α phase are given by its hexagonal structure. For example, it results in an anisotropy of elastic properties of single crystals

of α titanium. The elastic modulus varies between 145 GPa for load parallel to c-axis and 100 GPa perpendicular to the axis [1]. The shear modulus ranges from 46 GPa to 34 GPa for stresses applied in $\langle 11\bar{2}0\rangle$ direction and in (0002) or $\{1010\}$ planes, respectively.

There are 12 slip systems in the hexagonal structure [6]. The slip system consists of slip direction and slip plane. The three main slip directions are $\langle 11\bar{2}0\rangle$, which are in the (0001), the three $\{10\bar{1}0\}$ planes and the six $\{101\bar{1}\}$ planes. However, only 8 out of these 12 slip systems are independent, this is further reduced only to 4, because the shape changes that are produced by combined action of slip system in planes $\{0001\}$ and $\{10\bar{1}0\}$ with slip direction $\langle 11\bar{2}0\rangle$ are exactly the same as those of slip in the planes $\{10\bar{1}1\}$ in direction $\langle 11\bar{2}0\rangle$. These planes and slip directions are shown in Fig. 1.3

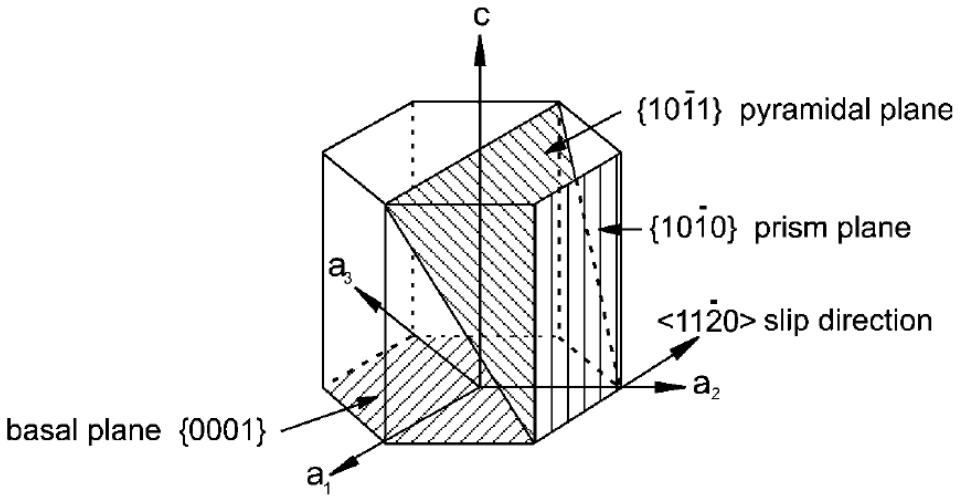

Figure 1.3: Slip planes and slip directions in the hexagonal α phase [6]

According to von Mises criterion, at least five independent slip systems for homogeneous plastic deformation in polycrystals are required. Therefore, one additional mechanism is required. This is provided by twinning. However, in α phase, the twinning is nearly suppressed and $\overrightarrow{c} + \overrightarrow{a}$ slip with direction $\langle 11\bar{2}3\rangle$ needs to be activated [6].

In the bcc β phase there are 12 slip systems, 6 planes $\{110\}$ with 2 slip directions $\langle 111\rangle$. The von Mises criterion is fulfilled so the plastic deformation of β phase is homogeneous. The elastic modulus of this phase just above the β-transus temperature is about 58 GPa and the shear modulus is approximately 20 GPa [6]. These moduli cannot be measured for pure titanium at room temperature because the β phase is not stable.

1.2 Titanium alloys

The main reasons for alloying titanium are to modify β-transus temperature and also to produce a two phase region, where $\alpha+\beta$ coexist. Ti alloys typically receive a thermomechanical treatment to precipitate additional phases. Solution treating above the β-transus temperature followed by annealing precipitation of alpha phase, omega phase and/or intermetallics improves yield strength and fracture

toughness. The morphology, size and distribution of these precipitates determine in large part the mechanical properties of the alloy. The alloying elements of titanium are classified depending on their influence on the β-transus temperature as neutral, α stabilizers, or β-stabilizers. For example, the substitution element Al and the interstitial elements O, N and C are α-stabilizers and increase the β-transus temperature with increasing solute content, as can be seen from the schematic phase diagram in Fig. 1.6. The β-stabilizers (Mo, V, Ta, Nb, etc.) shift the β-transus temperature to lower temperatures, while the neutral elements have only minor influence on this temperature. They slightly decrease the transition temperature for lower concentrations, but for higher concentrations the β-transus temperature increases again.

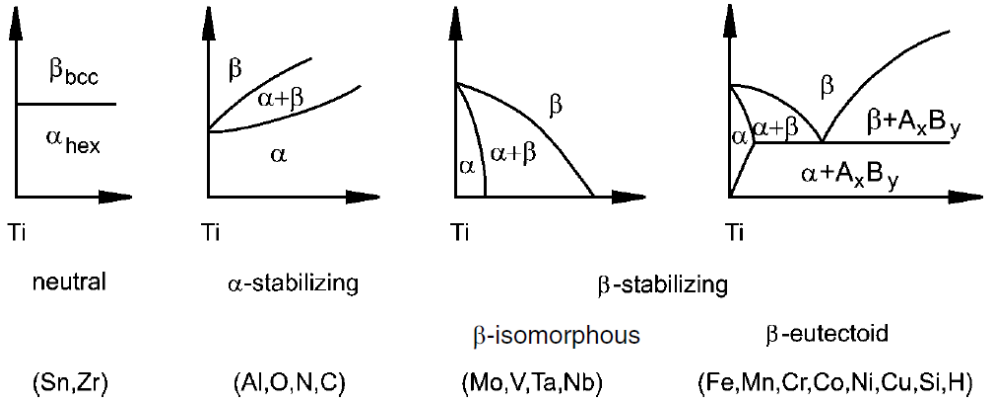

Figure 1.4: Effect of alloying elements on phase diagrams of titanium alloys (schematically) [6]

Most commonly used α-stabilizer is aluminium, because it is the only common metal raising the transition temperature with good solubility in both α and β phases. The β-stabilizers are divided into β isomorphous elements and β eutectoid forming elements. By adding sufficient amount of the isomorphous elements, the β phase could become stable at room temperature. The β eutectoid forming elements have a limited solubility and even a very low volume fraction of them can lead to the formation of intermetallic compounds.

The effect of alloying elements was expressed in terms of molybdenum equivalency (equation 1.6. It shows the amount of each addition needed to have same effect on the β-transus as molybdenum. The amount of molybdenum needed in order to lower the martensitic decomposition of the β phase to the α phase below room temperature is about 10 wt % of molybdenum. According to the equation 1.6 , it correspond to 15 wt % of vanadium and to 3.5 wt % of iron.

$$\begin{aligned}[\mathrm{Mo}]_{\mathrm{eq.}} = [\mathrm{Mo}] + 0.67[\mathrm{V}] + 0.44[\mathrm{W}] + 0.28[\mathrm{Nb}] + 0.22[\mathrm{Ta}] + 2.9[\mathrm{Fe}] \\ +1.6[\mathrm{Cr}] + 1.25[\mathrm{Ni}] + 1.7[\mathrm{Mn}] + 1.7[\mathrm{Co}] - 1.0[\mathrm{Al}]\end{aligned} \tag{1.6}$$

The negative constant before Al in Equation 1.6 corresponds to its opposite tendency to stabilize α phase [7].

1.2.1 The classification of titanium alloys

Titanium alloys are divided depending on the amount of the alloying elements into α, α+β and β alloys. The near α and the metastable β alloys are considered in more detail. The classification is schematically shown in Fig. 1.5.

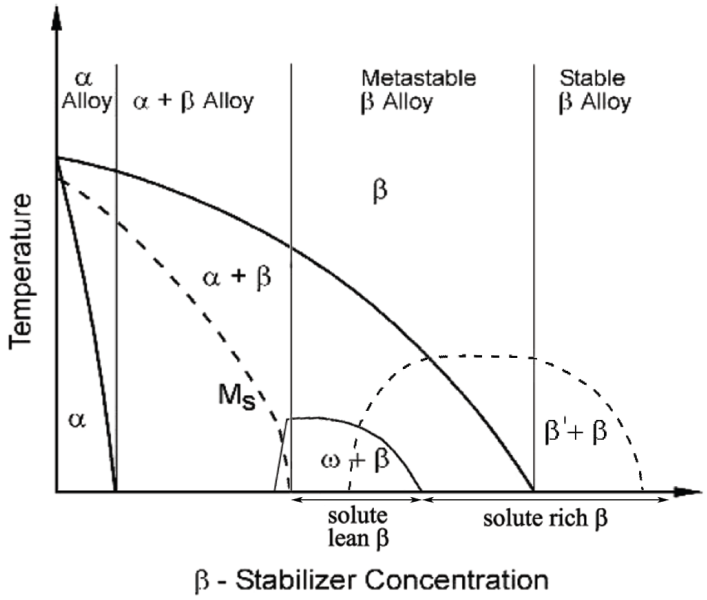

Figure 1.5: Schematic phase diagram to classify Ti alloys [7]

The α alloys contain only pure Ti, Ti alloyed with the α-stabilizers, or with neutral elements. If minor fractions of β stabilizing elements are added, the alloys are referred to as the near α alloys. The $\alpha + \beta$ alloys are the most widely used alloys. The volume fraction of β phase at room temperature ranges from 5 - 40%. Further increase of the content of β stabilizing elements to a certain level results in a decrease of temperature of the start of martesitic transformation just bellow room temperature and β phase no longer transforms upon quenching. This is still in the $\alpha + \beta$ class, but this is already in β metastable field. In the equilibrium, the volume fraction of α phase can be more than 50 %. β metastable alloys are the most versatile from all titanium alloys. Among the advantages of these alloys belong high strength to weight ratio, high ductility and high fatigue resistance. On the contrary, disadvantages in comparison with $\alpha + \beta$ alloys are higher density and higher cost. Single-phase β alloy is created by further increase of the β-stabilizers contents. These alloys do not have commercial or practical use, because of rather poor mechanical properties with no possibility of precipitation hardening. Therefore, β metastable alloys are also known as β alloys [1].

1.2.2 Phases in Ti alloys

The α and β phases were discussed earlier in this work. Both these phases can be stable at room temperature. However, there exist more phases in titanium alloys. One could be already seen in Fig. 1.5. It is one of the most studied phases in titanium alloys - the ω phase.

The ω phase was discovered by Frost et al. [8] in 1954. Since then, this phase has been found in numerous alloys of group IV transition elements. This

phase received extensive attention of scientists. That is because of the complex morphology of the ω phase and its effect on physical properties such as ductility, superconductivity etc. The forming of the ω phase was explained by Hickman in his review [9]. The main conditions under which ω phase grows according to [10] are:

1. The thermal treatment:

   (a) The ω phase forms upon quenching from β phase. This is commonly called athermal ω. Formation of this phase is diffusionless. The experiments proved reversibility of $\beta \rightarrow \omega$ transformation [11]. It was also shown that even ultra fast quenching rates were insufficient to suppress this transformation. For a particular composition there is defined ω-start temperature (T_ω), where this phase forms during quenching. This temperature is schematically shown in Fig. 1.5 as line which limits $\omega + \beta$ phase field [10].

   (b) The ω phase forms during ageing at temperatures near T_ω. This is called isothermal ω, because thermal activation is necessary for its growth. The exact ageing temperature range for ω phase formation varies from one system to another. The growth of ω_{iso} continues from the ω_{ath} particles, which remain after heating to a certain temperature. The growth of ω_{iso} particles is diffusion controlled and it is accompanied by a shift of lattice parameter of the β phase, which indicates an enrichment of the β phase with alloying elements. The terms "athermal" and "isothermal" are used to describe the thermal conditions upon which the ω phase forms.

2. The pressure: The pressure aids the formation of the ω phase and extends the range of compositions in which the ω is observed. At room temperature, the pressure necessary to transform the ω form the α has to be higher than about 30 kbar.

3. The deformation: The formation of the ω phase was observed in some alloys during deformation by Bagaryatskiy et al. (in Ti-8Cr) [12] and by Kuan et al. (in Ti-V alloy single crystal) [13].

The ω phase has either hexagonal or trigonal unit cell. The hexagonal ω, which is known as ideal ω, occurs in less concentrated alloys, while the trigonal occurrence is in the opposite. The unit cell of both has the $c/a \simeq 0.612$. Usually in both ω phases there is no preferential occupancy of atom positions by any of the constituents. The morphology of the ω particles depends on the coherency strain associated with its forming. This is solute content dependent parameter. In alloys where the misfit strain is less than 1%, e.g., Ti-Mo, Ti-Nb and Ti-Ta, the occurring particles have ellipsoidal shape and their major axis is up to 100 nm long. In the alloys where the misfit exceeds 1%, e.g., Ti-V, Ti-Ni and Ti-Cu, the cuboidal ω precipitates with edge length up to 50 nm occur. It has been suggested that the misfit determines the stability of the ω phase. The suggestion is based on the hypothesis that many phases are stable only because of the constraint of the parent lattice [14].

If the solute content of β-stabilizer is high enough, the metastable ω phase becomes unstable and does not precipitate. On the other hand, the β phase separates into β_{lean} and β_{rich}. This occurs either by nucleation and growth or by spinodal decomposition depending on the kinetics of the separation. β_{lean} is known as β' and β_{rich} simply as β, which can be seen in Fig. 1.5. The both β phases have the same crystallographic structure as the parent phase. The only differences are therefore solute content and lattice parameters. β_{lean} forms coherent and uniformly dispersed particles within the β matrix.

In pure Ti and dilute Ti alloys two more phases can occur by quenching from β phase. They are thermal martensites. The hexagonal α', and the orthorombic α". $B2, \alpha_2$ and γ phases also occur in titanium alloys. However, these phases are not important for this work, so their description will be skipped.

1.3 Phase transformations

The phase transformation can be classified based on mechanisms. The designated two classes are: (a) *diffusional* and (b) *displacive* transformations. The first one corresponds to reconstructive transformation in which atom movements from the parent to the product lattice sites occur by random diffusional jumps. This implies that near neighbour bonds are broken at the transformation front and the product structure is reconstructed by placing the incoming atoms at appropriate positions which results in the growth of the product lattice. On the other hand, atom movements in a displacive transformation can be accomplished by a homogeneous distortion, shuffling of lattice planes, static displacement waves or a combination of these. All these displacive modes involve cooperative movements of large numbers of atoms in a diffusionless process. Displacive (which includes martensitic) transformations are initiated by the formation of nuclei of the product phase, and the growth of these nuclei occurs by the movement of a shear front at a speed that approaches the speed of sound in the material [15]. Schematic diagram of atom movements can be seen in Fig. 1.6.

Many phase transformations occur in titanium alloys during thermo-mechanical treatments. This work focuses on metastable β alloys, so the important ones for this work are $\beta \rightarrow \alpha$, $\beta \rightarrow \omega$ and $\omega \rightarrow \alpha$ transformations.

1.3.1 $\beta \rightarrow \alpha$ transformation

The precipitation of α phase in β matrix is a thermally activated diffusional process. It is controlled by the migration of the α/β interface and the diffusion of solute atoms across the interface. Both processes occur simultaneously during growth of the precipitates and the slower one determines the growth rate. When the diffusion of solute atoms is slower than the interface migration rate, the interface will move as fast as the diffusion allows and the transformation is said to be diffusion controlled. On the other hand, when the interface mobility is the limiting process, interface controlled transformation occurs [7]. Upon cooling from the β phase the most densely packed planes of the bcc β phase $\{110\}$ transform to basal planes $\{0001\}$ of hexagonal α phase. This transformation causes a slight atomic distortion, see Fig. 1.7. This is reason for non-ideal c/a ratio of the α phase

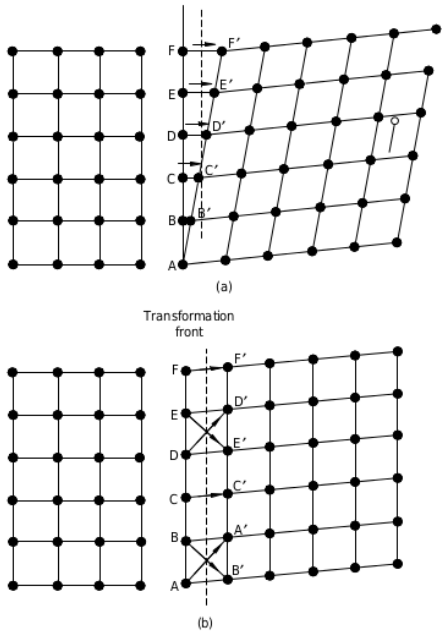

Figure 1.6: Schematic diagram of atom movements across the transformation front in a (a) displacive transformation; (b) diffusional transformation [15].

unit cell. For the α phase precipitated in the β matrix Burgers relationship with four variants applies:

$$\begin{aligned}(0001)_\alpha \parallel (110)_\beta \\ [11\bar{2}0]_\alpha \parallel [111]_\beta\end{aligned} \tag{1.7}$$

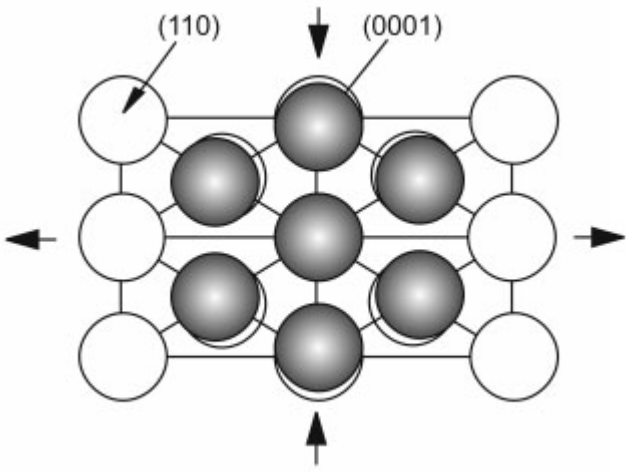

Figure 1.7: β/α transformation according to Burgers relationship [1]

The preferred nucleation sites of the α phase growth in β alloys are: β/β grain boundaries, previously formed α particles, ω particles, dislocations and β_{lean} phase formed during phase separation in β titanium alloys. In $\alpha+\beta$ alloys, one more additional nucleation site, the martensite plates, is present [15].

Each nucleation site results in a distinct morphology and distribution of the α phase. Three types of nucleation mechanisms are distinguished based on the ageing temperature and the nucleation site [16]:

1. At relatively low ageing temperatures (below 450 °C), the appearance of α is preceded by ω. The α precipitates are extremely fine and dispersed uniformly throughout the β matrix. This transformation is explained in detail in Section: 1.3.3.

2. For ageing temperatures above 400 °C, there is a sufficient thermal activation to allow non-uniform nucleation of the α phase. The nucleated α phase bears no relationship to the dispersion of the ω phase in the β matrix. The grain boundaries were observed as nucleation sites for this transformation, but there is also an evidence of nucleation within grains. The precipitates of the α phase are non-uniform plates with high aspect ratio. The observed distribution of the α phase precipitates is called patchy.

3. The third precipitation regime is evident at higher temperatures (above 650 °C). Thick α layers form along β/β grain boundaries with smaller number of the α precipitates. The low number of precipitates reflects small driving force for α nucleation as the temperature approaches the β-transus.

1.3.2 $\beta \rightarrow \omega$ transformation

As mentioned earlier, the ω phase appears as a metastable phase in Ti alloys which contain the required levels of β stabilizing elements. The orientation relationship between the β and the ω phase is:

$$\begin{aligned} (111)_\beta &\parallel (0001)_\omega \\ [1\bar{1}0]_\beta &\parallel [11\bar{2}0]_\omega \end{aligned} \tag{1.8}$$

In the most common model of forming the ω phase, the ω lattice is created by collapsing a pair of the $(111)_\beta$ planes to the intermediate position, leaving the next plane unaffected, and collapsing the next pair of planes and so on. This is schematically shown in Fig. 1.8. According to this picture, the planes marked as 1 and 2 collapse in the middle (marked as 1.5) and the 0 and 3 are kept unaffected.

If the collapse is complete, a sixfold rotation symmetry is created around the $[111]_\beta$ direction along which lattice collapse occurs. In case the collapse is incomplete, the resulting ω structure has a trigonal symmetry. The hexagonal and the trigonal structures can be formed by introducing a displacement wave in the parent bcc structure. This is illustrated in Fig. 1.9 where a displacement wave with the wave vector, $\overrightarrow{K} = 2/3[111]_\beta$, can create the hexagonal structure when the amplitude of the wave is sufficient for moving $\{222\}$ planes by a distance $1/2\{222\}$. When the amplitude of the wave is smaller, the resulting structure is trigonal.

There are four possible $[111]_\beta$ directions, which results into four possible crystallographic variants of the ω structure in a parent bcc crystal.

The $\beta \rightarrow \omega$ transformation proceeds under two different conditions, namely, during quenching from the β phase field and during isothermal ageing at a

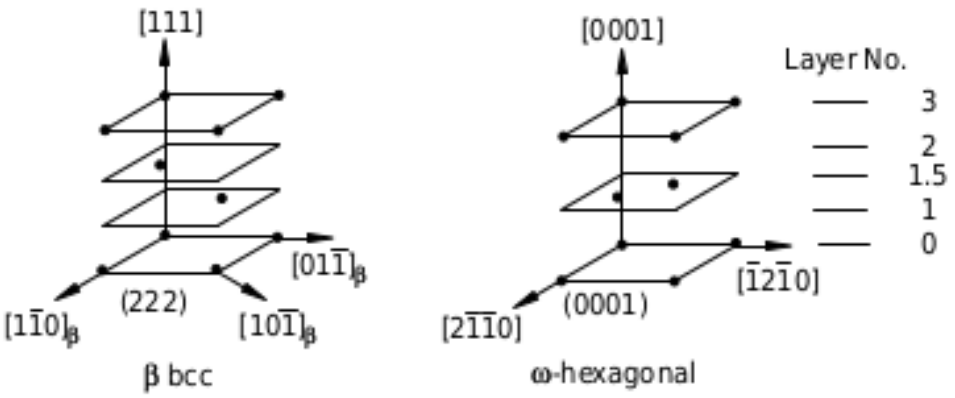

Figure 1.8: Schematic collapse of $(111)_\beta$ planes [15]

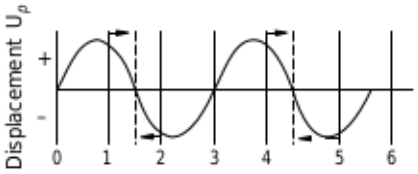

Figure 1.9: The displacement of {222} planes [15]

temperature below about 400 °C. The kinetic characteristics of these two cases correspond to an athermal and a thermally activated process, respectively.

Athermal $\beta \rightarrow \omega$ transformation

This is a pure shuffle transformation and does not include any macroscopic shape strain. When such a mechanism is operative, the product and the parent phases can maintain complete coherency along the entire interface. This could be attained by quenching an ω forming alloy from the β phase field. The athermal nature of the transformation has been established through ultrahigh quench rate experiments. The fact that the transformation is not suppressible even under such quenching conditions suggests that the transformation can occur without any thermal activation. The complete reversibility of the transformation is yet another evidence for its athermal nature. All these observations suggest that this transformation can be classified as a displacive transformation. Particles of the ω phase that form during quenching do not have a plate-like morphology or a surface relief effect typical for a martensitic transformation. Because of that, the athermal $\beta \rightarrow \omega$ transformation is not categorized as a martensitic transformation even though it has athermal and composition-invariant character.

Thermally activated precipitation of the ω phase

Precipitates of the ω phase grow in the β phase upon ageing at temperatures below $\sim$ 400 °C, which is the upper limit for this transformation in most of the β solid solutions. The increase in the volume fraction and the growth of ω particles with increasing ageing time indicates a thermally activated transformation mechanism. The lattice correspondence between the β and the structure of ω_{iso} is the same as that observed in the case of the athermal transformation. These

features suggest that the isothermal precipitation occurs by an atomistic mechanism which is essentially the same as that in the athermal transformation. The thermally activated component of the transformation mainly involves a solute-partitioning process which accompanies the lattice collapse mechanism.

1.3.3 $\omega \rightarrow \alpha$ transformation

The over-ageing of material with $\omega + \beta$ phase microstructure results in α phase precipitation. Different mechanisms have been proposed describing the role of ω precipitates in the nucleation of α precipitates:

1. At the ω/β interfaces. It was shown in [17] that when the critical misfit of the interface is exceeded, interfacial edge dislocations form in $\langle 110 \rangle_\beta$ directions. The formation of dislocations is then followed by nucleation of α rod-shaped precipitate lying in the same orientation as the corresponding dislocation. The nucleation at the dislocation or adjacent to it is happening due to stress fields induced by the dislocation. The α phase nucleated at the ω/β interface has the following orientation relationship with the β and the ω phases [18]:

$$\begin{aligned} (0001)_\omega \parallel (\bar{1}2\bar{1}0)_\alpha \parallel (\bar{1}11)_\beta \\ (\bar{1}\bar{1}20)_\omega \parallel (0001)_\alpha \parallel (0\bar{1}1)_\beta \\ [1\bar{1}00]_\omega \parallel (10\bar{1}1)_\alpha \parallel [211]_\beta \end{aligned} \tag{1.9}$$

   After some ageing time the α phase grows over the ω phase.

2. In the systems with a lower ω/β misfit, there are two different models of $\omega \rightarrow \alpha$ transformation [19]:

   (a) The α precipitates nucleate at certain distance from the ω/β interface. This is caused by local rejection of the ω destabilizers ($= \alpha$ stabilizers), during the isothermal ageing of ω precipitates, which aids the nucleation of α precipitates in the vicinity of the ω precipitates.

   (b) By displacive transformation within the core of the ω precipitates, leading to the formation of α platelets. There is a strict orientation relationship at the α/ω interface. This leads to a perfect planar interface between these two phases and the α phase is able to grow from the ω phase. Two kinetic growth regimes were observed, so model explaining the nucleation and growth mechanism of α phase can be proposed [20] and schematically shown in Fig. 1.10: After nucleation from the ω phase by a displacive transformation, the α phase growth associated with the first regime is directly issued from the ω consumption. This leads to the plate-like morphology. During the second regime, the ω phase has completely disappeared and the α growth is now governed by the interface mobility between α and β. From this point and depending on the degree of coherency, the mobility of the interface in the width direction is lower (better coherency) than in the length direction.

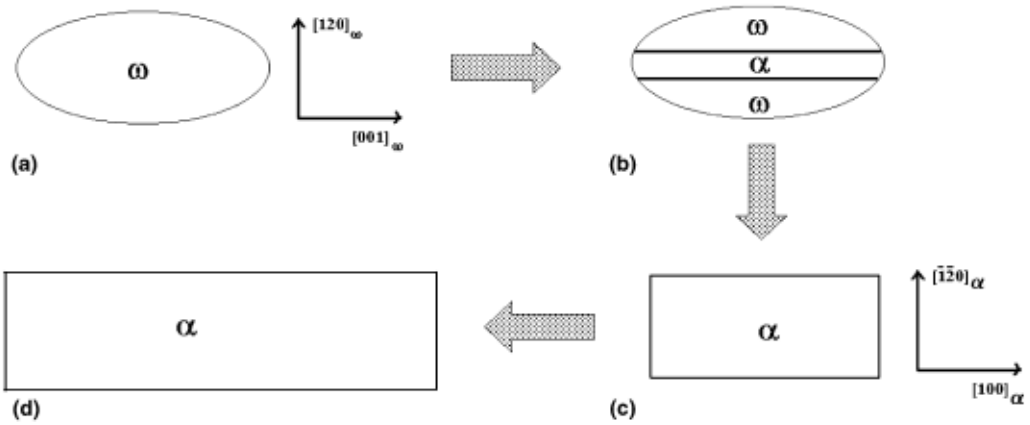

Figure 1.10: Nucleation and growth model of α phase: (a) ω phase acting as a heterogeneous nucleation site, (b) α growth from ω consumption, (c) ω disappearance and (d) α growth from β consumption [20].

2. Experimental procedures

2.1 Studied alloy

In this research, Ti-15Mo titanium alloy with 15 wt. % (8.1 at. %) of molybdenum was studied. The material was solution treated (ST) at 900 °C for 4 hours and subsequently quenched in water.

Molybdenum is a beta stabilizing element and a minimum 10 wt. % molybdenum content is needed in a Ti-Mo binary alloy to lower the temperature of the start of martesitic transformation below room temperature, which makes β phase no longer transform upon quenching. Fig. 2.1 shows the equilibrium binary phase diagram of the Ti-Mo system. The red line indicates the chemical composition of the Ti-15Mo alloy. The $\alpha + \beta$ to β phase transformation (β-transus) occurs around 750 °C. In Table 2.2 significant points of Ti-Mo system are summarized.

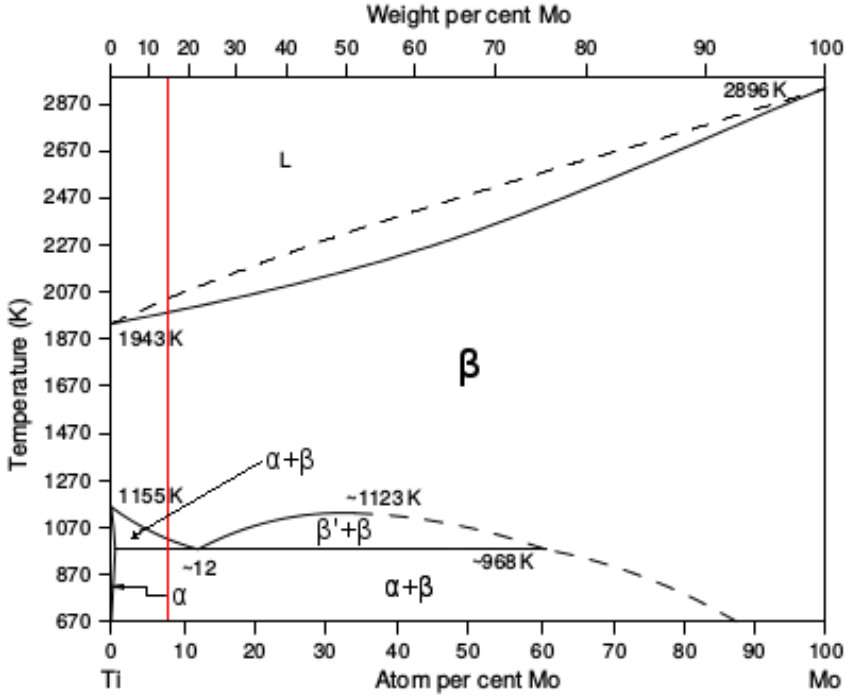

Figure 2.1: Equilibrium phase diagram of Ti-Mo system [15].

Phase reaction	Type of reaction	Temperature [°C]	Composition (at. % Mo)
$L \leftrightarrow \beta$	Melting	1670	0
$L \leftrightarrow Mo$	Melting	2623	100
$\beta \leftrightarrow \beta' + \beta$	Spinodal decomposition	~ 850	~ 33
$\beta \leftrightarrow \alpha + \beta$	Monotectoid	~ 695	(12) (0.4) (~ 60)
$\beta \leftrightarrow \alpha$	Allotropic	882	0

Table 2.1: Significant points of Ti-Mo system [15].

The equilibrium solid phases are: the bcc β solid solution, in which Ti and

Mo are completely miscible above the allotropic transformation temperature of Ti (882 °C), the hcp α solid solution in which the solubility of Mo is restricted (maximum of about 0.4 at.%). This system exhibits a miscibility gap in β. Thus, phase separation occurs in $\beta' + \beta$ regime. The monotectoid reaction: $\beta \leftrightarrow \alpha + \beta$ takes place at about 695 °C [15].

Ti-15Mo is a relatively new material used mainly for biomedical applications that belongs to an advanced class of metallic biomaterials known as β titanium alloys. The Ti-Mo alloy system was originally developed for the chemical industry to provide a titanium alloy with improved corrosion resistance. High temperature applications were also investigated but thermal handling difficulties and microstructure instability at moderate temperatures prevented widespread use in the aerospace industry.

Composition limits for Ti-15Mo are specified by a standard and are listed in Table 2.2.

Element	Composition [wt. %]
Ni	max 0.05
C	max 0.1
H	max 0.015
Fe	max 0.1
O	max 0.2
Mo	14.0-16.0
Ti	Balance

Table 2.2: Composition limits for Ti-15Mo alloy [21].

Important physical properties are summarized in Table 2.3. The values of electrical resistance and thermal conductivity are for fully aged material.

Density [mg/cm^3]	4.96
Modulus of Elasticity in Tension [GPa]	78 (β) 105 ($\alpha + \beta$)
Electrical Resistivity at 31 °C [µΩ mm^{-1}]	800
Mean Coefficient of Thermal Expansion from 50–600 °C [10^{-6}/°C]	8.5
Thermal Conductivity at 31 °C [cal/cm s°C]	0.03

Table 2.3: Physical properties of Ti-15Mo alloy [21].

2.2 Electrical resistance measurement

Measurement of electrical resistance and its dependence on temperature is commonly used for detection of structural changes and phase transformations in the material. To be able to successfully understand processes, which occur in material by measuring electrical resistance, basic theoretical knowledge of electrical conductivity is necessary. The electrical conductivity (σ) is the ability of a substance to conduct an electric current and it is the inverse of the resistivity (ρ):

$$\sigma = 1/\rho \tag{2.1}$$

The resistivity is material property, whilst resistance (R) refers only to specific sample. The relationship between these two quantities is defined in equation 2.2:

$$\rho = \frac{S}{l}R, \tag{2.2}$$

where S stands for cross-section area of the sample and l for its length.

In most materials (e.g. metals), the current is carried by electrons. They are fermions (particles which have half-integer spin) and according to the Pauli exclusion principle, no two electrons in an atom can have the same set of (four) quantum numbers. At absolute zero electrons stay at the lowest possible energy states and they all have energy lower than the so called Fermi energy. It is the energy of the highest occupied single particle state (at 0 K). At higher temperatures a certain fraction, characterized by the Fermi function (equation 2.3), will exist above the Fermi energy [22].

$$f(E) = \frac{1}{e^{(E-E_F)/kT} + 1}, \tag{2.3}$$

where E is energy, k represents Botzmann's constant, T absolute temperature and E_F is the Fermi level. It is energy level with 50 % probability of occupation at finite temperature. The Fermi level plays an important role in the band theory of solids. Bands represent the available energies for electrons in the material. Crucial to the conduction process is whether or not there are electrons in the conduction band. In conductors like metals the valence band (contains valence electrons, which are in the outermost shell of an atom) overlaps the conduction band. In semiconductors there is a small enough gap between the valence and conduction bands that thermal or other excitations can bridge the gap. A large gap separates valence and conduction band in insulators [22]. Fig. 2.2 schematically shows energy bands in solids.

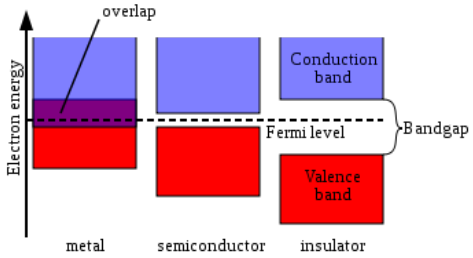

Figure 2.2: Schematic energy bands in solids [23].

Energy, which excites electrons into conducting states, is provided by an electric field. The force acting on the electron is $-eE$ (e is the electric charge, E is the value of electric field). This force produces a constant acceleration, therefore, in the absence of obstacles the electron speeds up continuously in the electric field. In a real solid, the electrons scatter by collisions with imperfections and due to atomic thermal vibrations. This "frictions" leads to electric resistance. To characterize the flow of an electron in the direction of the acting force, the drift velocity of the electron motion is established:

$$|v_d| = \frac{eE}{m}\tau, \tag{2.4}$$

where τ represents the average time between collisions. The "friction" transfers a part of the energy supplied by the electric field into the lattice as Joule's heat. Electron speed can be approximated by Fermi speed:

$$v_F = \sqrt{\frac{2E_F}{m}} \tag{2.5}$$

The conductivity of the material can be expressed in terms of the Fermi speed v_F and the mean free path d ($= v_F\tau$) of an electron in the metal:

$$\sigma = \frac{nev_d}{E} = \frac{ne^2}{m}\tau = \frac{ne^2 d}{mv_F} \tag{2.6}$$

The mean free path d for Ti could by approximately computed with these parameters: free electron density: $n = 2.26 \times 10^{29}$, conductivity at 20 °C: $\sigma = 2.38 \times 10^6\ /\Omega m$, Fermi speed: $v_F = 1.76 \times 10^6\ m/s$, electron mass: $m = 9.12 \times 10^{-31}\ kg$ and electron electric charge: $e = 1.6 \times 10^{-19}\ C$. After substitution the mean free path equals:

$$d \doteq 6.6 \times 10^{-10} m = 0.66nm \tag{2.7}$$

The resistivity ρ is defined by scattering events due to the imperfections and thermal vibrations. Matthiessen rule says that the total resistivity ρ_{total} can be approximated by adding up several different terms:

$$\rho_{total} = \rho_{thermal} + \rho_{impurity} + \rho_{deformation}, \tag{2.8}$$

where the components stand for different types of electron scattering: $\rho_{thermal}$ - on thermal vibrations, $\rho_{impurity}$ - on impurities, $\rho_{deformation}$ - on deformation-induced defects.

Influence of temperature

In the first approximation resistivity of material rises linearly with temperature (increasing thermal vibrations and density of vacancies):

$$\rho(T) = \rho_0 \left[1 + \alpha \left(T - T_0\right)\right], \tag{2.9}$$

where α is called the temperature resistivity coefficient (TRC), T_0 is a reference temperature, and ρ_0 is the resistivity at T_0. The parameter α is an empirical parameter fitted from measurement data and varies for different reference temperatures. The relationship 2.9 is valid only in a range of temperatures around the T_0. When the temperature varies over a large temperature range, the linear approximation is inadequate [24].

Electrical resistivity of metals generally increases with temperature. Key role can be played by an electron–phonon (thermal vibrations) interactions. Around room temperature, the resistance of a metal should increase linearly with temperature. At cryogenic temperatures, the temperature dependence of resistivity is mathematically approximated by the Bloch–Grüneisen formula [24]:

$$\rho_{thermal}(T) = \rho_0 + A\left(\frac{T}{\Phi_R}\right)^n \int_0^{\frac{\Phi_R}{T}} \frac{x^n}{(e^x - 1)\,(1 - e^{-n})}, \tag{2.10}$$

where ρ_0 is the residual resistivity due to defect scattering, A is a constant. Φ_R is the Debye temperature and n is integer that depends upon the nature of interaction:

1. $n = 5$ - scattering of electrons by phonons (for simple metals)
2. $n = 3$ - s-d electron scattering (for transition metals; scattering of conduction (s) electrons in d band)
3. $n = 2$ - electron–electron interaction.

Influence of imperfections

In a perfect lattice at 0 K no electron scattering occur. However, metal lattices are not perfect. Lattice imperfection include vacancies, dislocations, impurities. These defects scatter conduction electrons, which increase electric resistivity of the material. Impurities that form in solid solution affect resistivity in following way [25]

$$\rho_{impurity} = A\ c_{impurity}\,(1 - c_{impurity})\,, \tag{2.11}$$

where $c_{impurity}$ is impurity concentration, A – composition independent constant. For two phase alloys, the rule-of-mixtures can be used:

$$\rho_{eff} = \rho_\alpha V_\alpha + \rho_\beta V_\beta, \tag{2.12}$$

where the term stand for: ρ_{eff} - effective resistivity, V - volume fraction of α or β phase, ρ - resistivity of α or β phase. Alloying pure metal always increases the amount of disorder in the lattice. Therefore, the resistivity of material also increases. This happens even when the added metal has a lower resistivity in its pure form. For low concentrations of added metal, the resistivity increases linearly, but for higher percentages the increase goes slower. A maximum is usually reached around a 50 % composition. Higher contents can be considered as alloy of first metal in second one.

Four-point method was used for this study. Circuit scheme of this technique is shown in Fig. 2.3. Electrical current passes through the two outer probes (1 and 4), while the voltage is measured between the two inner contacts (2 and 3). The advantage of this method is that the resistance of connecting leads and their contacts with the sample does not affect the measured resistance. Since the resistance of the voltmeter is much greater that the resistance of the sample, the current which flows through the voltmeter is negligible compared to the flow through the sample. Thus, the resistance of the voltmeter leads and contacts does not play a significant role. Commutated direct current is used to eliminate transient and thermoelectric effects, which arise due to different temperatures on the contacts during voltage measurements and on joints of different material. The influence of these effects can be eliminated by calculating the average voltage values measured for current flow in both directions.

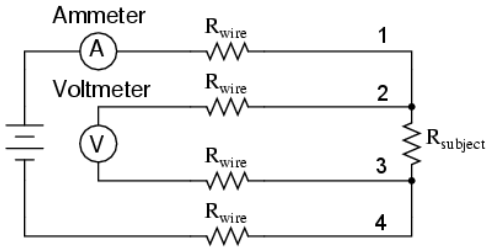

Figure 2.3: Schematic four-point probe.

Samples for electrical resistance measurements were cut from bulk material by an automatic precision saw Struers Accutom-50 with Struers silicon-carbide wafering blade. The blade speed was 1500 rpm and the feed rate 0.005 mm s^{-1}. Material cooling during cutting and cutting debris removal was ensured by recirculating water. Specimens had a shape shown in Fig. 2.4 and were about 1 mm thick. These plates were subjected to the heat treatment determined from measurement of ST samples. To eliminate any deformation or contamination of the surface layer, approximately 0.2 mm was removed from both sides by grinding with 220 grit (European FEPA grading) SiC grinding paper. Then the samples were ground and polished using 500 and 800 grit SiC papers. The resulting thickness of the samples was about 0.6 mm.

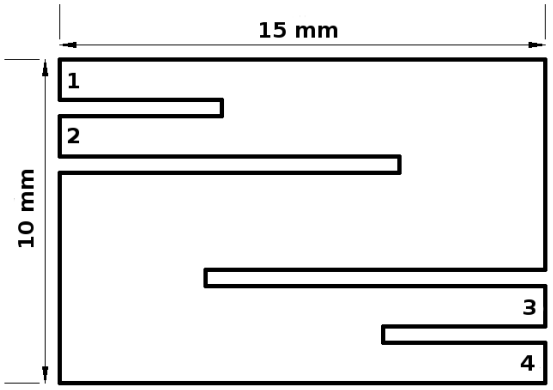

Figure 2.4: Shape of the sample used for electrical resistance measurement. Thickness is 0.6 mm.

The voltage was measured simultaneously with the electrical current using nanovoltmeter Keithley 2182 and SourceMeter Keithley 2400 device, respectively. The samples were placed in a specially designed furnace which allows precise heating of the sample in the protective argon atmosphere up to 850 °C. Heating rate used in most measurements was 5 °C/min. Fig. 2.5 schematically shows the furnace used in this measurement.

Measurement at cryogenic temperatures was done in following way. The sample was inserted between two 10 mm thick copper sheets. This ensures an uniform distribution of the heat along the sample. This system was put into liquid nitrogen. When the system stabilized (the sample and the copper sheets had the temperature of boiling nitrogen) the measurement started. The sample was not heated by any device, the temperature rose only because of surroundings. The dependence of temperature on time is shown in Fig. 2.6.

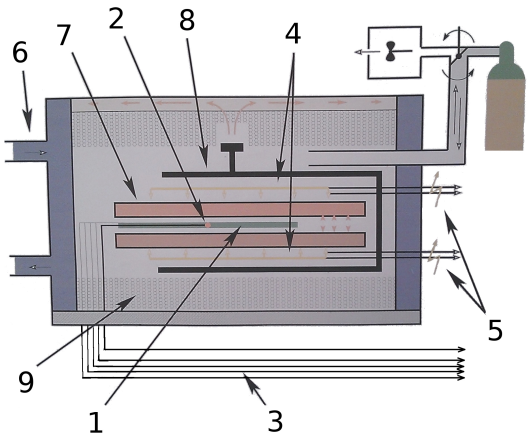

Figure 2.5: Furnace chart: 1 - sample, 2 - thermocouple, 3 - signal lead, 4 - heating coil, 5 - power lead, 6 - water cooling system, 7 - heat basin, 8 - internal gripper, 9 - heat barrier.

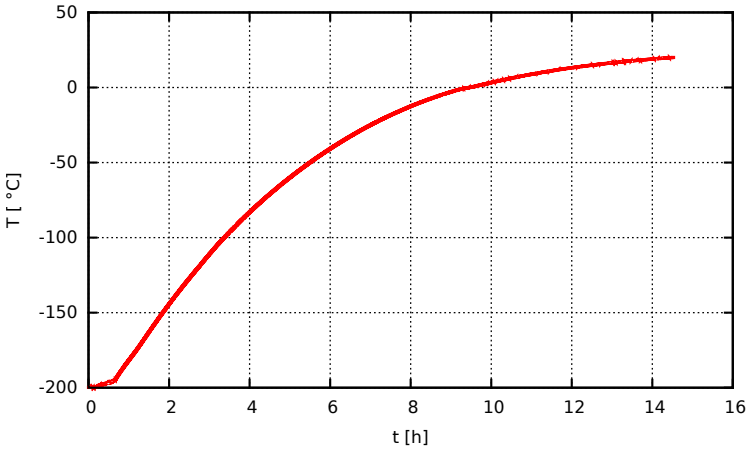

Figure 2.6: The dependence of temperature on time for the device in the range from -196 °C up to room temperature (RT).

The Fig. 2.6 shows that the heating rate during this measurement is slow enough. Thus, the results obtained by this measurement are not affected by high heating rate.

2.3 Differential scanning calorimetry (DSC)

DSC is a thermoanalytical technique, which measures the difference in the amount of heat required to increase the temperature of a sample and a reference one. The measured and the reference sample are maintained at nearly the same temperature during the experiment. The reference sample has to have a well-defined heat capacity over the measured range of temperatures. A DSC measuring cell consists of a furnace and an integrated sensor with designated positions for the sample and reference pans (Fig. 2.7). The sensor areas are connected to thermocouples, which allows measuring temperatures of both, the sample and the reference. The DSC signal (heat flux) is then plotted as a function of temperature or time.

The reference side (usually an empty pan) generally heats faster than the

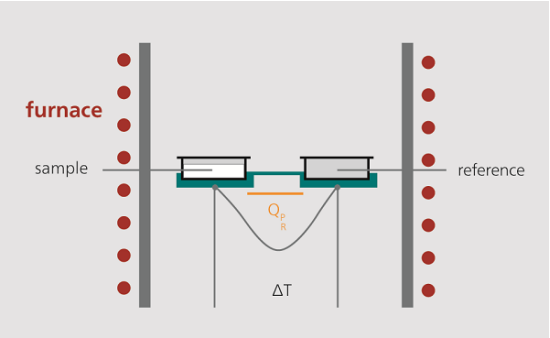

Figure 2.7: DSC measuring cell [26].

sample side, because of the heat capacity of the sample. The two dependencies exhibit parallel behaviour during heating at a constant heating rate – until a reaction in sample the occurs, such as a phase transition. More or less heat will need to flow to the sample than to the reference to maintain both at the same temperature. Whether less or more heat must flow to the sample depends on whether the process is exothermic or endothermic. For example, during endothermic process the heat is absorbed by the sample. Likewise, as the sample undergoes exothermic processes (such as crystallization) less heat is required to raise the sample temperature. Any transition accompanied by a change in specific heat produces a discontinuity in the power signal, which gives peaks whose areas are proportional to the total enthalpy change. Orientation of the peaks depends on the used notation. In this work exothermic peaks are directed upwards and endothermic downwards [27]. The exothermic processes are for example: solidification, crystallization, some cross-linking processes, oxidation reactions, and some decomposition reactions. Among endothermic processes belongs melting, dissolution, etc.

The differential scanning calorimetry measurements were performed on Netzsch calorimeter DSC 404 Pegasus. The sample was held in a static argon atmosphere during the whole measurement. Two heating rates were selected for this study – 5 °C/min and 50 °C/min.

2.4 Scanning electron microscopy

Scanning electron microscopy (SEM) is used for the study of microstructure of the samples. An electron beam is focused to a spot of about 0.4 nm to 5 nm in diameter. The electromagnetic lenses in the microscope deflect the beam in the x and y axes so it scans in a raster fashion over a rectangular area of the sample surface. In contrast to an optical microscope the resulting image in SEM is created by secondary signal - back-scattered (BSE) or secondary electrons (SE). The big advantage of SEM compared to the light microscope is a large depth of focus. The interaction of accelerated electrons with solid sample produces also other signals, which carry additional information about the sample e.g., X-rays, Auger electrons, cathodoluminescence.

Fig. 2.8 shows the excitation volume, which represents the area under the sample surface, where the primary electrons are decelerated and where the individual signals are formed [28]. Primary electrons penetrate to a certain depth

below the surface of the material, where they are diffused and absorbed by the atoms in the sample. Scattering of electrons can be either elastic or inelastic.

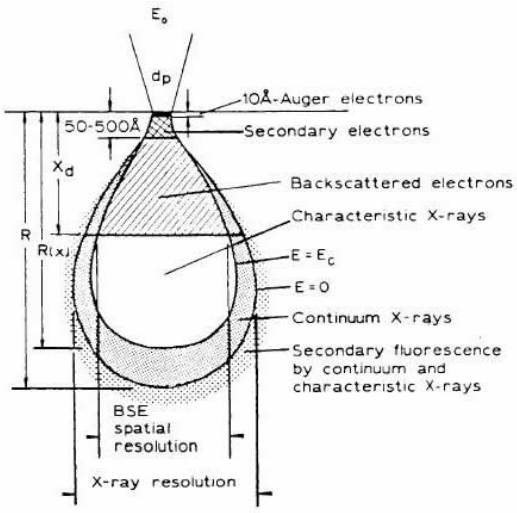

Figure 2.8: Excitation volume [28].

The elastically scattered primary electrons do not lose their energy in the surface layer of the sample. They only change the direction of motion and after multiple scattering are reflected back from the sample at a certain angle. Therefore, they are called backscattered electrons (BSE). The intensity of reflected BSE depends on the average atomic number Z of elements in the region from which the electrons are reflected. If it is an area with heavier elements (with higher atomic number), electrons are reflected with higher intensity than from lighter elements. Thus, in the images obtained using BSE, areas with higher Z appear brighter. BSE signal is used for elemental and phase analysis.

During an inelastic scattering process, primary electrons lose some energy. This energy is transmitted to the atoms in the surface layer. It leads to excitation of the atom which induces the emission of secondary particles from the inner shell. If the secondary particles are electrons, the effect is denoted as secondary electron (SE) emission. The excited electron moves towards the surface of the sample undergoing elastic and inelastic collisions until it reaches the surface, where it can escape if it still has sufficient energy. These energies are low (up to 50 eV [29]). This signal allows to establish the topography of the sample because the SE can escape only from thin surface layer. The inclined surfaces and humps emit more SE and these areas are displayed lighter shade than the pits.

Another important tool for material investigation in SEM is the energy-dispersive X-ray spectroscopy (EDX). The excited atom, from which the primary electron ejected an inner-shell electron, must return to the ground state. An electron hole is left after the ejection of the core electron. The electrons fall down to lower orbitals and leave the excited state, energy is emitted in the form of photons (X-rays). The wavelength of the photons is determined by the difference in energy between the two states which electrons transitted. These emitted photons form the element's spectrum. As the energy of the X-rays are characteristic of the difference in energy between the two shells, and of the atomic structure of the element from which they were emitted, this allows to investigate chemical composition of the sample.

The samples for SEM investigation were prepared in the same way as samples for electrical resistance measurement. However, they were further polished by 1200, 2400 and 4000 grit SiC papers. Final polishing was done using a vibratory polisher and employing 0.3 µm and 0.05 µm aqueous alumina suspensions (Al_2O_3) and 0.05 µm colloidal silica.

For the microstructural study of the samples scanning electron microscope QUANTA 200 FEG from FEI with an accelerating voltage of 20 kV was used. The microscope is equipped with BSE, SE and EDX detectors.

2.5 Microhardness testing

During the Vickers microhardness testing, a diamond indenter is impressed into the polished surface of the tested specimen. The indenter has pyramidal shape with a square base. The opposite sides form an angle of 136°. Fig. 2.9 shows the shape of the indenter used in Vickers method. Defined force is applied to the indenter and it is pressed into the specimen for a certain time. After the indentation, a small hole is left in the material. In an ideal case, the shape of the indentation is a square as it is shown in Fig. 2.10.

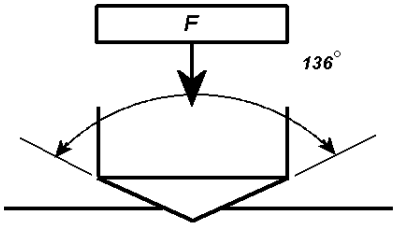

Figure 2.9: Shape of the indenter used in Vickers microhardness testing [30].

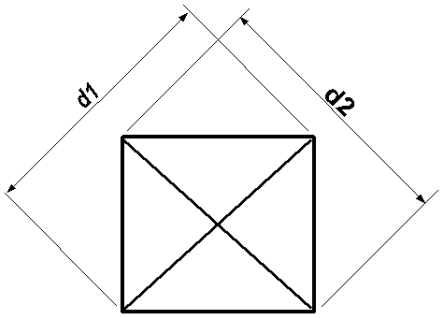

Figure 2.10: Shape of the indentation left on the sample after Vickers microhardness testing [30].

The surface area of the resulting indentation can be determined by formula [31]:

$$A = \frac{d^2}{2\sin(136°/2)}, \tag{2.13}$$

where d the is average length of the diagonal of the imprint left by the indenter in millimeters. Microhardness is determined by the ratio F/A, where F is the force applied to the diamond [31].

$$HV = \frac{F}{A} = \frac{2\sin(136°/2)F}{d^2}, \tag{2.14}$$

where F is in kilogram-force (kgf), or kilopond, which is a gravitational metric unit of force. It is equal to the magnitude of the force exerted by one kilogram of mass in a 9.80665 m/s^2 gravitational field [32].

The microhardness testing allows quick and easy estimation of basic mechanical properties of the material (e.g. the ultimate and tensile strength. Which

linearly correlates with the value of microhardness [33]). A matrix of indents on the surface is used for detection of inhomogeneities in the structure of the tested material.

The microhardess measurement was conducted on the samples previously used for SEM investigation.

The measurement was done with microhardness tester QNESS A10+. The computer program QPix Control automatically processed and evaluated microhardness values. The force applied by the indenter to the samples was 1 kgf.

2.6 Transmission electron microscopy

A beam of accelerated electrons is used in transmission electron microscopy (TEM) for imaging. The electron beam is emitted by thermal emission from the tungsten filament and passes through the optical system of the microscope. The electromagnetic lenses of TEM focus the electron beam and transmit it to the sample. The electrons are diffracted by crystal lattice. The resulting image consists of transmitted (not diffracted) and diffracted electrons and is observed on a fluorescent screen. Magnification in TEM can reach $10^5\times$. If the microscope is focused in the objective plane, one observes a direct image of the sample, so called bright field (BF), where the image is created by transmitted not diffracted electrons, or dark field (DF), where the observing aperture defines beam of diffracted electrons. If the microscope is focused in the back focal plane, the diffraction pattern with Kikuchi lines is obtained. This allows to easily determine the orientation of the sample [34].

For TEM observation, samples in the form of a disc with a diameter of 3 mm with a hole in the middle need to be produced. First, thin plates were cut from the bulk material by the same saw as previous specimens. However, they were thinned to thickness of about 0.15 mm using abrasive papers of various grit sizes. After that, the discs with the diameter of 3 mm were mechanically punched from the thinned material. Electropolishing which is commonly used for TEM sample preparation, cannot be used in the case of Ti-15Mo, as the material gets contaminated by hydrogen during the electropolishing at low temperatures (-20 °C) and the hydrides form inside the material. They have bigger volume than the original material, which leads to swelling accompanied by twinning. When the hole occurs, the tension inserted in material by forming of hydrides distorts the sample. When heated up to room temperature hydrogen evaporates, but the distorted structure remains [35]. Image of the distorted sample is shown in Fig. 2.11 and the Fig. 2.12 shows it in detail. The big clearly visible needle-shaped areas probably occurs during creation of hole, thanks to strain in sample. Most of twins can be seen near the grain boundaries. They even grow through needle-shaped areas.

The samples for TEM were prepared by ion polishing, where accelerated argon ions sputter away material until it is transparent.

The prepared samples were mounted on a special holder which allows double tilt. The observations were performed on JEOL JEM 2000FX microscope with an operating voltage of 200 kV.

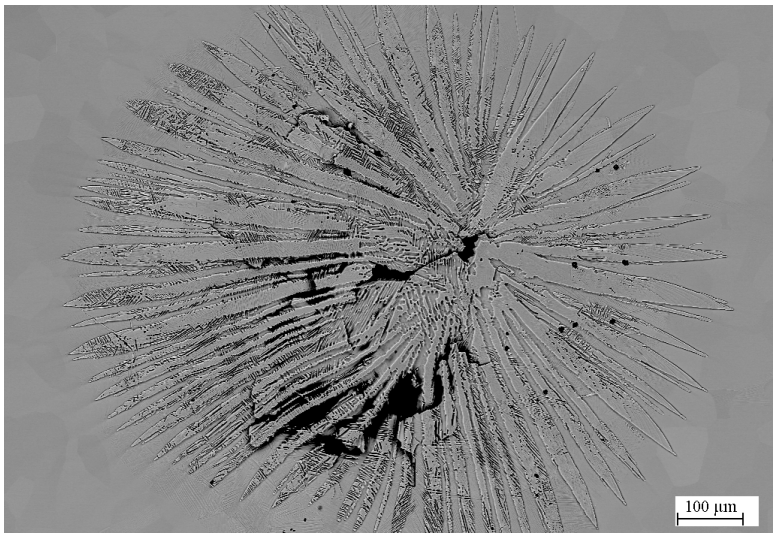

Figure 2.11: Microstructure of the electropolished sample.

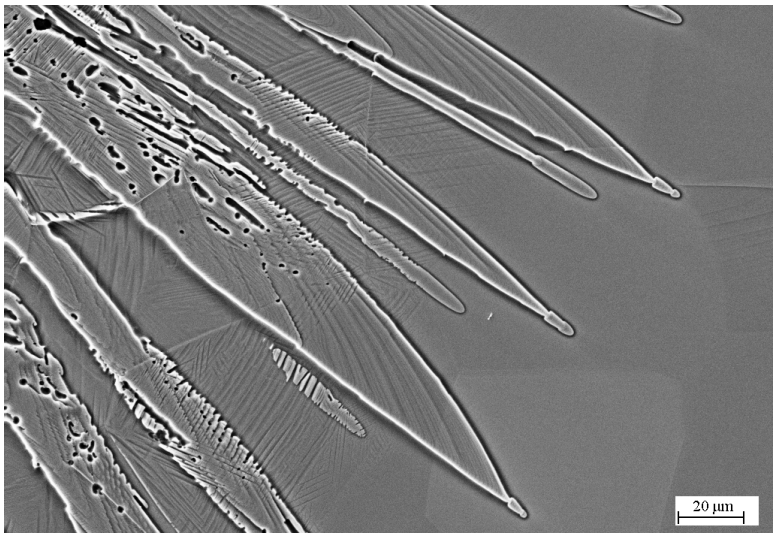

Figure 2.12: Detailed microstructure of the electropolished sample.

3. Aims of the thesis

The ultimate goal of the research in the present work is the detection and characterization of the phase transformations, which occur in Ti-15Mo during heating. These transformations were detected using in-situ electrical resistance measurement of solution treated sample. This measurement showed interesting changes in dependence of electrical resistance on temperature. The material was aged at temperatures determined by this result, as well as to correlate with measurements presented in literature. The influence of ageing at these temperatures on the resistance of the material was studied. Next, the actual processes, which occur in material will be identified and discussed. Also the influence of the phase transformations on the mechanical properties (microhardness) will be measured.

This present work focuses in particular on:

- Detection and characterization of the phase transformations occurring in Ti-15Mo during heating.
- Studying the influence of these processes on: electrical resistance, microstructure and microhardness.
- Comparison of results given by each measuring method and an explanation of the differences.

4. Results and Discussion

The methods discussed in Chapter 2 were used to accomplish the aims of the work. The following results and discussion will be divided into the parts corresponding to the used methods. The main results will be presented and discussed in this Chapter.

4.1 Electrical resistance measurement

For easier comparison of measurements of electrical resistance evolution of different samples, the results have to be normalized. The best solution would be to normalize by the shape of the sample - compute resistivity: $\rho = RS/l$. However, because the shape of used samples is quite complex, this computation would not be accurate enough. The normalization by initial resistance or R_{RT} is commonly used [20]. Samples with different thermal history were measured in this work. These samples have varying structure at RT. During heating up to temperature above the β-transus, all effects caused by previous thermal treatment should disappear and the structure of the samples should differ minimally (above the β-transus temperature only the β phase occurs in the material). Because of that, we tried to normalize most of presented results by resistance at the maximal measured temperature (850 °C). However, this choice was also not ideal. The structure is never completely the same. This is very probably caused by different oxidation of each sample at high temperatures. It results in deviation between curves of the resistance dependence. Fig. 4.1 shows a comparison of samples after identical heat treatment (two samples aged at 300 °C for 4 hours and two aged at 300 °C for 16 hours), as well as different ones (solution treated and quenched in water after heating up to 550 °C). One can see that for samples with the same thermal history, curves normalized by R_{RT} value are in good agreement at lower temperatures. For higher temperatures it sometimes goes a little bit off, probably because of oxidation. However, this deflection has the same effect for normalizing by R_{850} where the curves are not in agreement at lower temperatures. For different samples the typical approach of normalizing by R_{RT} fails. On the other hand, the the normalization by R_{850} gives nice results, which is clearly visible from the Fig. 4.2.

However, neither one of the previous normalizations is satisfying enough. Therefore, we normalized by value of resistance at 600 °C (R_{600}). This is shown in Fig. 4.3.

The last normalization shows the best visual agreement for curves. Regardless of the thermal treatment history of the material, the normalized resistance of all samples exhibits the same evolution around 600 °C. Moreover, oxidation is still minimal at this temperature. Therefore, normalization by R_{600} will be used in this work for comparison of the results for different samples. The repeated measurements for each condition of material show good agreement throughout nearly the whole measurement (oxidation occurring at high temperatures can be neglected). That fact proves the reproducibility of measurement. The results will be, for lucidity, presented just for one sample. The figures where the results are not compared will be normalized by R_{RT}. The normalization constant will be

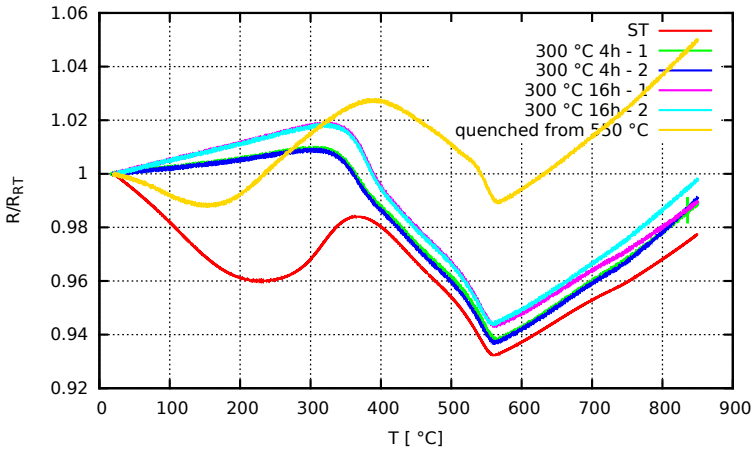

Figure 4.1: Normalization by R_{RT}.

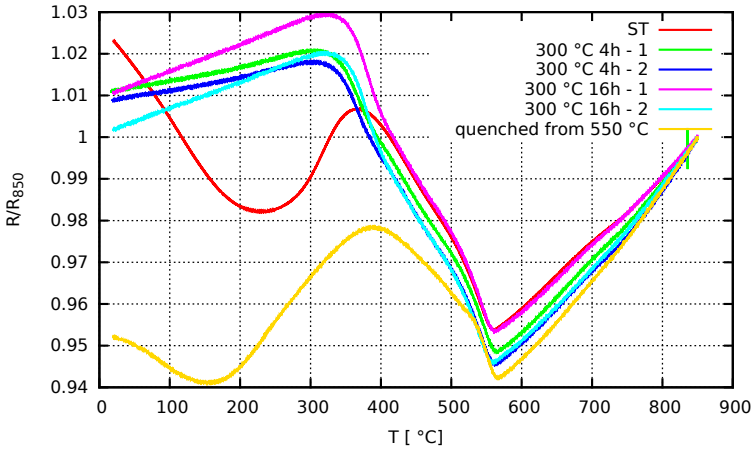

Figure 4.2: Normalization by R_{850}.

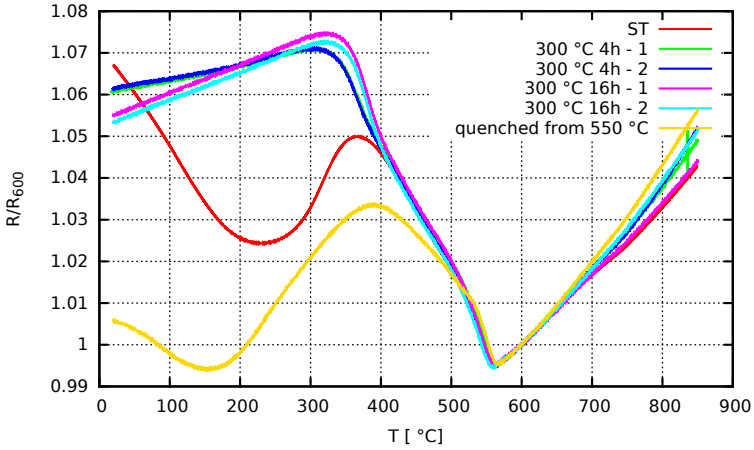

Figure 4.3: Normalization by R_{600}.

always shown in the y-axis label.

The measurement done on the solution treated material is shown in Fig. 4.4, where the red line represents electrical resistance during heating and the blue one during cooling. These results are also presented in Attachments at page 57

as two pictures next to each other. The temperature dependence of electrical resistance for heating is on the left panel and for cooling on the right panel. It is also necessary to note that for cooling, temperature on the x axis goes from higher to lower values.

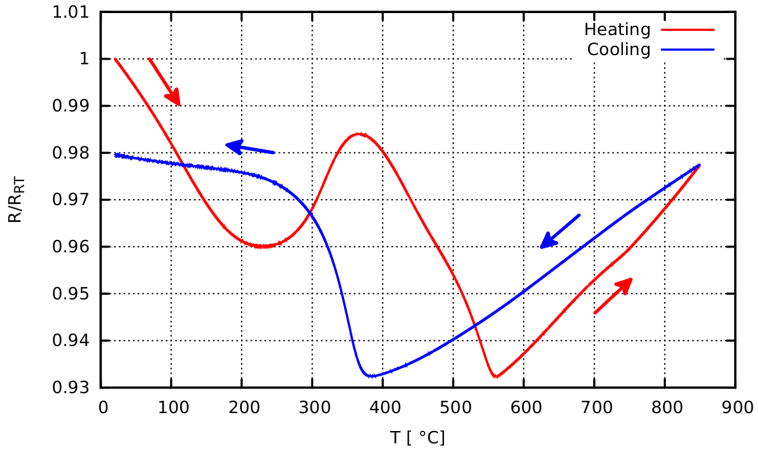

Figure 4.4: The dependence of electrical resistance on temperature for ST sample.

The trend of electrical resistance changed at 225 °C, 356 °C and 560 °C during heating and at 380 °C during cooling. In the intervals defined by these temperatures, the monotonicity of the function changed between increasing and decreasing. The significant temperatures define zones shown in Attachments at page 57. These zones correlate with phase transformations which occur in the material. Also the derivative of the dependence from this measurement (Fig. 4.5) shows several significant points which are at 112 °C, 317 °C, 437 °C, 539 °C, 575 °C and 730 °C. The change of monotonicity of resistance indicates, that new transformation (scattering mechanism) begins to outweigh the old one. Whereas from the derivative (Fig. 4.5) one can deduce starting or finishing points of these transformations.

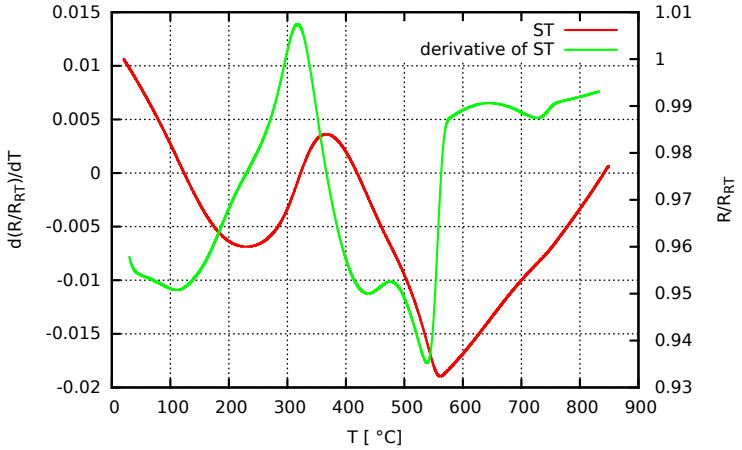

Figure 4.5: Derivative of the dependence of electrical resistance on temperature of ST material.

The resistance evolution from Fig. 4.4 and its derivative (Fig. 4.5) were used to determine the further thermal treatment of investigated specimens.

4.1.1 Zone I

In order to determine lower limit of zone I and to investigate behaviour of electrical resistivity at low temperatures, the specimen was cooled in liquid nitrogen and then left to heat up to room temperature. The electrical resistance and the temperature were measured. The result is shown in Fig. 4.6. The resistance decreases with increasing temperature for the whole measurement and does not reach the maximum even at the lowest temperature. These results suggest, that this zone starts even lower than -196 °C. It is not possible to exactly define this temperature until the measurements for even lower temperatures are done. Unfortunately, such temperatures are inaccessible in the current experimental setup.

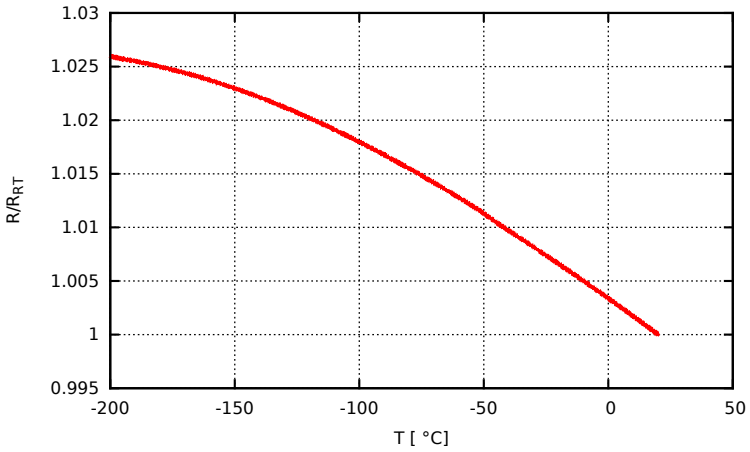

Figure 4.6: The dependence of electrical resistance on temperature from -196 °C to RT of ST sample.

The anomalous negative temperature coefficient of electrical resistance (TRC), where $TRC = \frac{d(R/R_0)}{dT}$ is linked to the ω_{ath} phase which forms during cooling from the β phase by a shuffle transformation. In the vicinity of the coherent β/ω interface elastic strain field occurs. It is an obstacle for movement of conducting electrons and increases electric resistance of the sample. During heating, the ω_{ath} dissolves by an inverse shuffle and these elastic strain fields are released, which clears the matrix for electron drift. It leads to a decrease in conduction electron scattering and therefore the resistance drops [36]. The presence of the ω_{ath} was investigated by TEM. The diffraction pattern of solution treated sample is shown in Fig. 4.7. The bright points are caused by diffraction of electrons on planes in β phase. The less intense points are caused by the ω phase. This figure confirms the presence of ω_{ath} phase and also the Burgers relationship between the β and the ω phase.

Fig. 4.8 schematically shows the negative diffraction pattern for the ω and β phase. It has the same orientation as measured one (Fig. 4.7) and could be used to identify the reflections. One can see, that only two (out of four) orientations of the ω particles in β matrix are visible. The reflections for other two merge together with the reflections from the β phase.

One weak beam from Fig. 4.7 corresponding to diffraction $\{\bar{2}020\}_\omega$ was selected and the DF image of the sample was taken. The white dots represent the

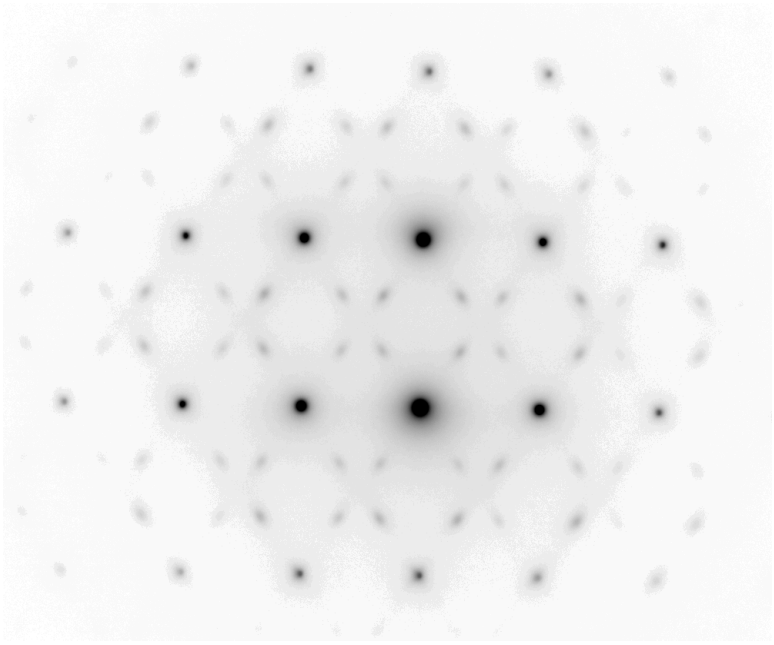

Figure 4.7: Negative TEM diffraction pattern of solution treated Ti-15Mo, showing presence of two phases: $[110]_\beta \parallel [1120]_\omega$.

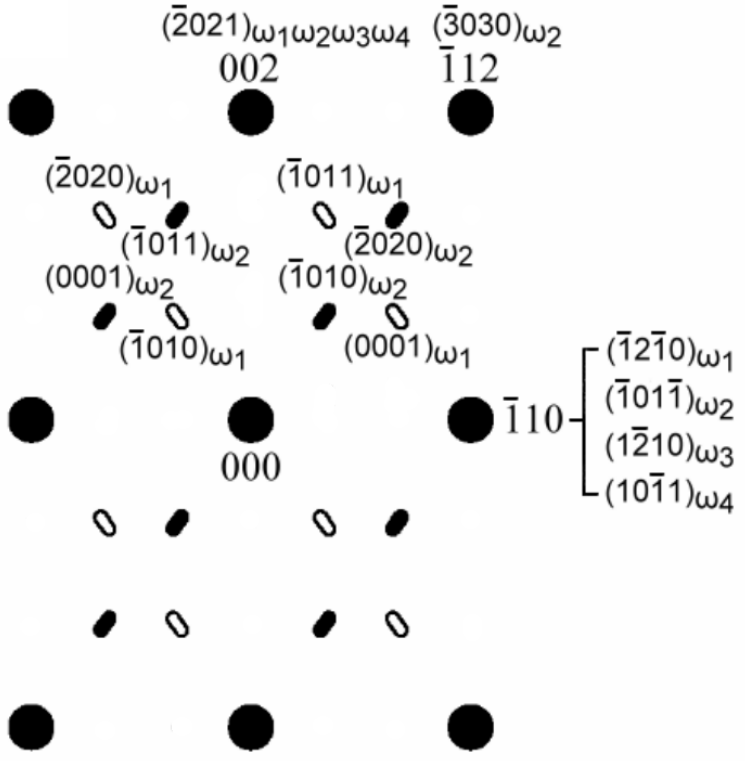

Figure 4.8: Schematic diffraction pattern denoting indices of the reflections [38].

ω precipitates. Their size is in the order of nanometers. There are four possible orientations of the ω particles in the β-matrix. Selected beam corresponds to only one orientation. Fig. 4.7 shows only 1/4 of ω particles.

The ω_{ath} transformation is reversible up to about 110 °C. This was proven

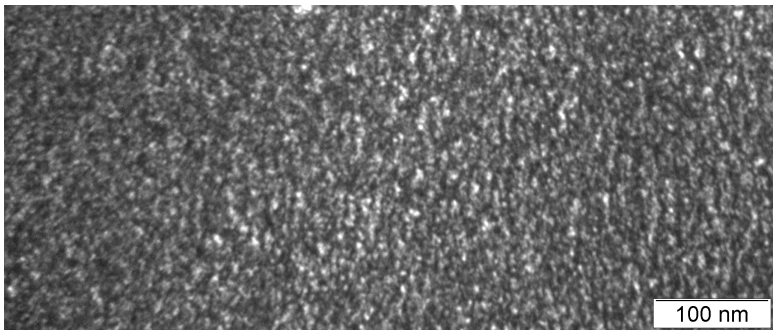

Figure 4.9: ω_{ath} in solution treated Ti-15Mo shown by DF TEM.

by repeated heating (heating rate 5 °C/min) and cooling of the sample. It was sequentially heated up to 80, 90 and 100°C. The record of this measurement is plotted in Fig. 4.10. One can see, that the lines for cooling and heating follow the same path and resistance returns to the value, as it had before. The point of reversibility could be seen in Fig. 4.5 as the first minimum in the derivative. At this temperature the diffusion controlled growth of ω starts. Particles, which grow diffusionally, are referred to as ω_{iso}. Most of the ω_{ath} precipitates still inversely shuffle back to the β phase. As the number of ω_{ath} particles decreases and growth of ω_{iso} gets more rapid, the resistance increases with temperature and the material enters zone II [39].

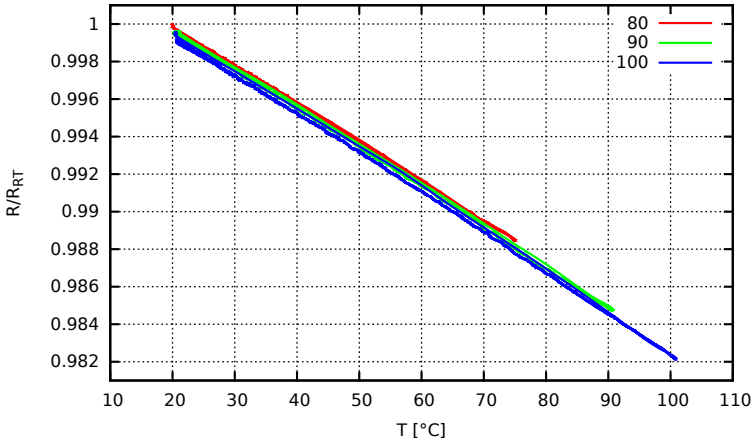

Figure 4.10: The electrical resistance dependence on temperature during heating and cooling.

In most metals, the resistivity of material decrease with precipitation of new phase, which is opposite of observed effect. When new phase diffusely nucleates during heating in typical alloy, the coherent precipitates grow first. Later the incoherent ones. The precipitates of new phase have different chemical composition than matrix. Their growth cleans the matrix from impurities, such as dopant atoms, which caused scattering of conduction electrons and the resistivity of material decreases. The newly formed phase interfaces increase electrical resistivity of material, but this effect is much lower than previous. On the other hand, if the precipitates of some phase are not stable and dissolute during heating the electric resistivity of material increases.

In metastable β titanium alloys, the ω_{ath} forms by diffusionless shuffle transformation. They are very small (around 1 nm) and occupy quite high volume fraction (tens of percent). The forming of this particles does not clean the matrix. It even greatly deforms the matrix and around each particle are elastic strain fields. When the ω_{ath} dissolutes (by inverse shuffle transformation), the elastic strain fields are relaxing and number of electron scattering sites decreases.

4.1.2 Zone II

This zone is between approximately 225 °C and 356 °C. The electrical resistivity of ST material increases during heating in this interval. The ω_{iso} particles (and their volume fraction) grow in this zone. This transformation is diffusional and thus, irreversible. As mentioned earlier, the ω_{iso} is actually ω_{ath}, which grows diffusionally. Thus, elastic strain also occurs around ω_{iso} precipitates and makes an obstacle for the electron movement. The elastic strain increases along with size of the ω_{iso} particles. This growth along with thermal vibrations of lattice causes increase of electric resistance of the sample results in positivity of the TRC up to 356 °C.

The samples aged at 300 °C for 4, 16 and 94 hours were measured to determine the influence of the ω phase on electrical resistance. Fig. 4.11 shows the measurements results. It has been shown in [10] that the volume fraction of the ω phase increases with time during ageing at 300 °C.

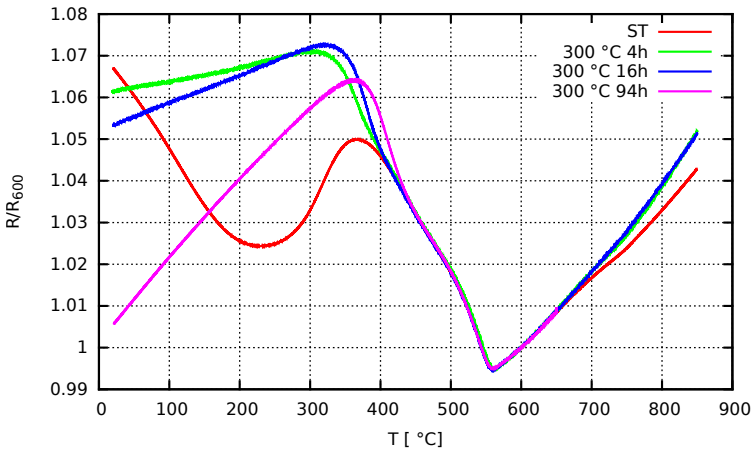

Figure 4.11: The electrical resistance dependence on temperature for samples aged at 300 °C for 4, 16 and 94 h compared with solution treated state.

One can see that already after ageing at 300 °C for 4 h the R increases during heating in zone I. The former decrease of R with increasing T was caused by dissolution of ω_{ath} precipitates. Fig. 4.11 proves that dissolution of the ω_{ath} is no longer the decisive process in the material after ageing at 300 °C. The samples aged for longer time have even lower R/R_{600} at RT. It means that the volume fraction of ω_{ath} decreases, whereas ω_{iso} increases with ageing time. The record of heating, ageing for 94 hours and cooling is shown in figure at page 59 in Attachments. On the x-axis in Ageing part is time in hours in logarithmic scale. After some ageing time at 300 °C, the resistivity decreases, which probably indicates relaxation of strain fields around the ω precipitates. This relaxation

could be connected with diffusion of atoms of molybdenum from the ω into the β phase. Concentration of Mo in matrix increases and the lattice parameter changes, which lowers the misfit between ω and β phases, which lowers strains at the ω/β interfaces. It agrees with Fig. 4.11, where the normalized values of R/R_{600} at RT are highest for the samples aged shorter time (not enough time for the diffusion of Mo and the relaxation of the strain). All aged samples, at the end of zone II (∼350 °C), have higher R/R_{600} than solution treated sample. Which is caused, as mentioned higher, by the presence of ω_{iso} particles.

4.1.3 Zone III

This zone lies between 356 °C and 560 °C. Near the end of zone II the α phase starts to precipitate, which leads to a decrease of R. The α phase particles have incoherent interface with the β matrix and preferentially nucleate on the ω phase, which results in disappearance of elastic strain at the β/ω interfaces, as mentioned earlier. The ω_{iso} does not stop its growth. The derivative (Fig. 4.5) shows, that the resistance decreases linearly nearly from the beginning of zone II and around 480 °C the decrease gets more rapid. This temperature marks the end of the growth of the ω phase. Three phases (β, α, ω) coexist in this regime.

The growth of the α phase was investigated in this zone.

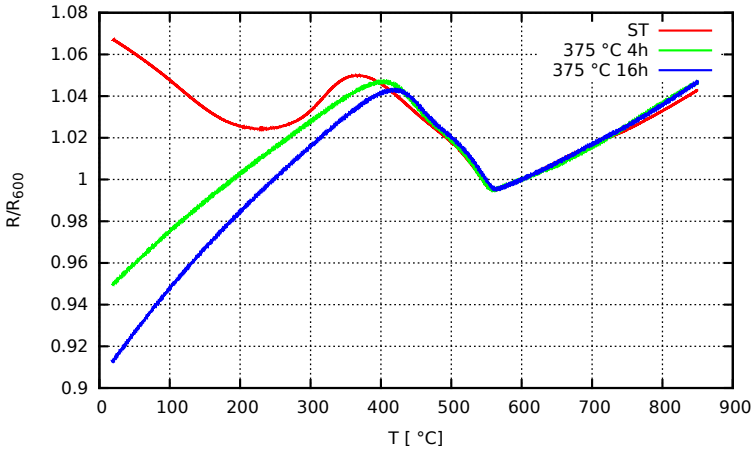

Figure 4.12: The electrical resistance dependence on temperature for samples aged at 375 °C for 4 and 16 h compared with solution treated state.

In Fig. 4.12 green (blue) curve represents the electrical resistance dependence on temperature for sample aged at 375 °C for 4 (16) hours. During such thermal treatment the volume fraction of the α and ω phases increase with ageing time, which leads to a decrease of the normalized value of R. Even after ageing for 16 h, the ω phase is still in the material. To completely dissolve the ω phase longer ageing time is needed. For different titanium alloy, the ω phase completely dissolve after ageing at 400 °C for 256 hours [7]. The occurrence of the ω in aged samples is reflected in decrease of resistance in zone III, where the α precipitates from it.

Fig. 4.13 shows the dependence of electrical resistance on temperature for sample aged for 28 hours at 550 °C. The curves for cooling after ageing and for second heating fit perfectly on each other. There is no detected transformation

during cooling or second heating after ageing, which means that the material aged at 550 °C for 28 h reached equilibrium concentration of phases and that the sample after ageing consists only of the α and β phase.

The resistance dependence on temperature of the sample at equilibrium phase composition has really high TRC. The value of resistance at 650 °C is nearly two times higher than R_{RT}. This can be seen in Fig. 4.13, from value of R/R_{RT} at RT and at 650 °C for second heating.

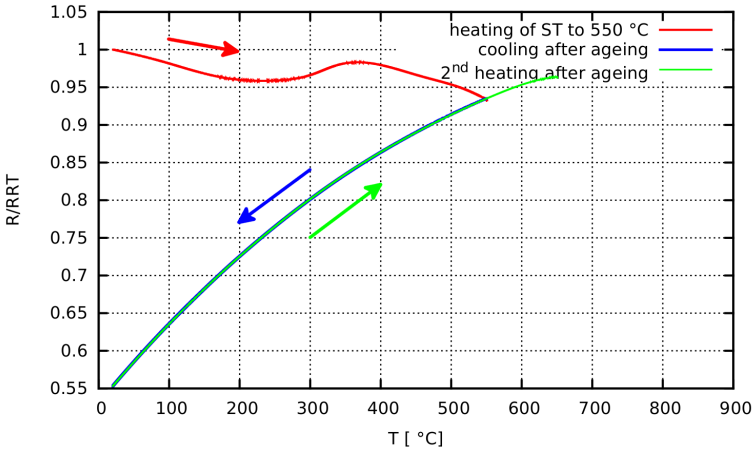

Figure 4.13: The electrical resistance dependence on temperature for solution treated material compared to state after ageing at 550 °C for 28 h.

The record of measurement (heating, ageing and cooling) of this sample is in Attachments at page 60.

The scale on Fig. 4.13 makes the dependence during first heating look flat, but it is exactly the same as the one in Fig. 4.4. Comparison of these two measurements can be found in Attachments at page 61.

It can be seen in Fig. 4.14 that the upper limit of zone III is equally defined even for measurements with different heating rate. This figure compares dependence of R/R_{RT} on T for heating rate 5 and 50 °C/min. This point is located at 560 °C and corresponds to the limit temperature of ω formation introduced in [11] and shown in Fig. 4.15.

One can also see that other zone limits shift to higher temperatures for faster heating rate.

In Fig. 4.15 the equilibrium phase digram is plotted by full curves. Dotted curves represent metastable ω/β phase diagram. Shaded region represents approximately the region of expected diffusionless transformation.

In order to examine phase transformation around the significant temperature of 560 °C, samples were heated up to 550 and 570 °C in salt bath with heating rate 5 °C/min and quenched in water . The electrical resistance dependence on temperature for these samples is shown in Fig. 4.16.

The normalized value of resistance of the sample heated up to 550 °C is lower than for others at RT. This is caused by presence of the α and the ω_{iso} phase. The initial decrease of R corresponds to dissolution of the ω_{ath} particles, which formed from the β phase during quenching from 550 °C. This decrease is small and has a low gradient. This means that only low volume fraction of the ω_{ath} during quenching was formed. This was due to presence of ω_{iso} particles at 550 °C,

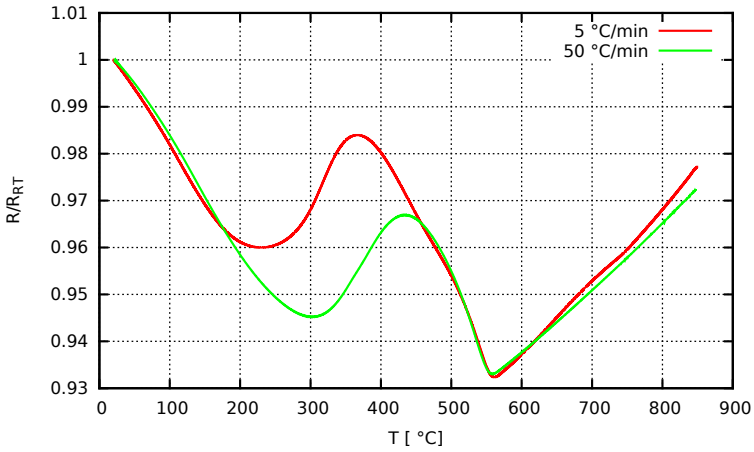

Figure 4.14: The dependence of electrical resistance on temperature with heating rate 50 °C/min.

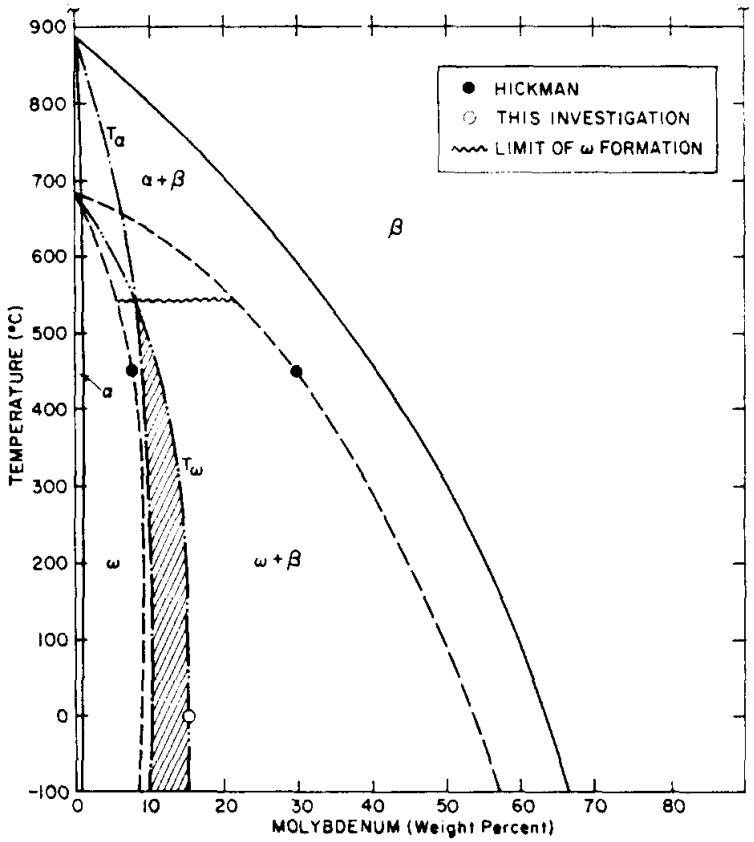

Figure 4.15: Phase diagram for Ti-Mo system based on experimental data [11].

which persist the quenching. The strain fields at ω_{iso}/β boundaries compensate strain induced in material during quenching. Thus, massive formation of the ω_{ath} particles does not occur.

The material quenched from 570 °C also contains some amount of the α phase. It follows not only from normalized value of R at RT, which is lower than for the ST sample. Presence of the α phase is also supported by lower value of R/R_{600} at the beginning of zone III (356 °C). The initial decrease is much more significant, than for the previous condition. This means the change of monotony of resistance

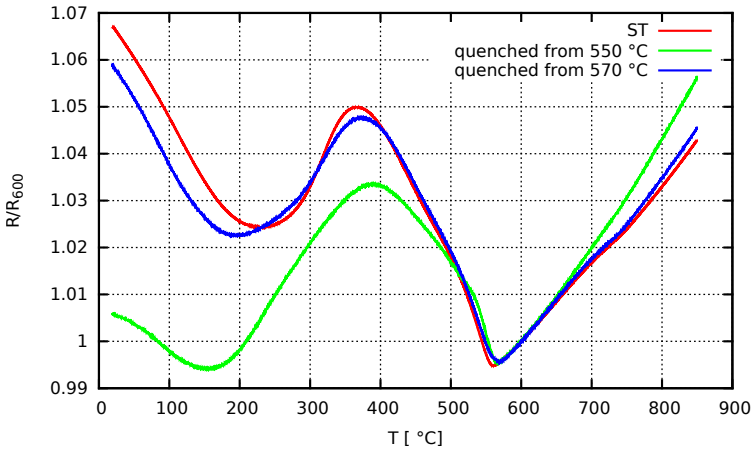

Figure 4.16: The dependence of electrical resistance on temperature for samples heated up to 550 and 570 °C and quenched in water.

dependence on temperature at 560 °C indicates dissolution of all ω phase. The strains again occur in matrix during quenching and now have to be compensated by forming the ω_{ath} particles.

Thus, the elastic strain, which prevented creating the ω_{ath} is no longer present. Therefore, the ω_{ath} can transform from the β phase during quenching.

4.1.4 Zones IV, V

There should not be any more ω phase in the sample in zone IV. The material should be headed towards equilibrium composition. The lamellar α phase precipitates from the β phase preferentially at grain boundaries in this regime. This is shown in a micrograph of the sample quenched from 570 °C from SEM, see Fig. 4.22.

The increase of electrical resistance is caused mainly by thermal vibrations. The dependence is linear throughout zone IV. This is confirmed by all earlier figures, which showed dependence of electrical resistance on temperature in this interval.

The upper limit of zone IV was defined at 730 °C, where a bump in the derivative is observed, see Fig. 4.5. It should correspond to β-transus. This temperature agrees with value from binary phase diagram. The resistance measured during cooling also confirms this idea. All samples heated above 730 °C (up to 850 °C) have similar resistance evolution as solution treated one (see green line in Fig. 4.17). The increase of resistance at 385 °C indicates forming the ω_{ath}. However, the sample, which was aged at 550 °C and reached equilibrium phase composition, was heated from RT for second time only to 650 °C. Its resistance evolution compared to solution treated sample during cooling is shown in Fig. 4.17 (x-axis decreases in order to respect course of time). There in no detected transformation during cooling observed, which indicates that the transition temperature must be higher. The only value, that comes into consideration after these arguments, is 730 °C.

In zone V the temperature is higher than the β-transus and the material contains only the β phase. The resistance dependence on temperature corresponds to

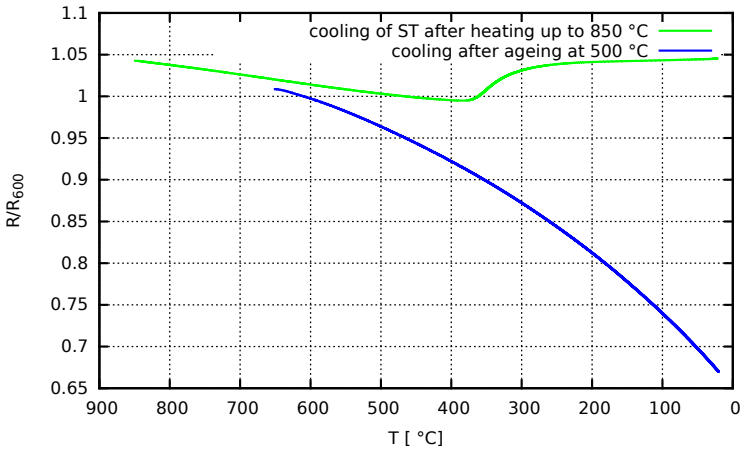

Figure 4.17: Comparison of the dependence of electrical resistance on temperature for cooling of: solution treated sample after heating up to 850 °C and sample after ageing at 550 °C for 28 hours.

electron scattering on thermal vibrations (linearly increases with temperature).

4.1.5 Zones VI, VII

The zone VI was introduced only because the sample is no longer heated up, but cooled. Material consists entirely of the β phase. The material has the same structure as in zone V. The increase of R during cooling corresponds with onset of zone VII (385 °C) and indicates nucleation of the ω phase from the β phase. This also shows that the ω phase forms even at slower cooling rates (5 °C/min and slower).

4.2 Scanning electron microscopy (SEM)

SEM was used to to observe solution treated material, as well as samples, which underwent different thermal treatment. Samples selected for SEM observations were aged at 375 °C for 4 and 16 hours and heated up to 550 and 570 °C, then quenched into water.

In Fig. 4.18 one can see SEM micrograph of solution treated sample. There are shown two different grains. The ω_{ath} particles too small and have the same chemical composition as the β phase, which makes impossible to observe them in SEM. The image from TEM (Fig. 4.9) shows, that the ω particles in solution treated material have size in the order of nanometers.

The microstructure of samples aged at 375 °C seems to be identical with solution treated one, see Fig. 4.19 and Fig. 4.20. However, electrical resistance measurement was different for these samples. This inconsistency in results is caused by deficiencies of SEM resolution. The ω particles still could not be seen in SEM. In both figures grain boundaries are shown, which serve as one of the preferential nucleation sites for the α phase.

Fig. 4.21 shows microstructure of material quenched from 550 °C. The black dots indicate the grown ω and α particles. Their size is about 40 nm, which is in

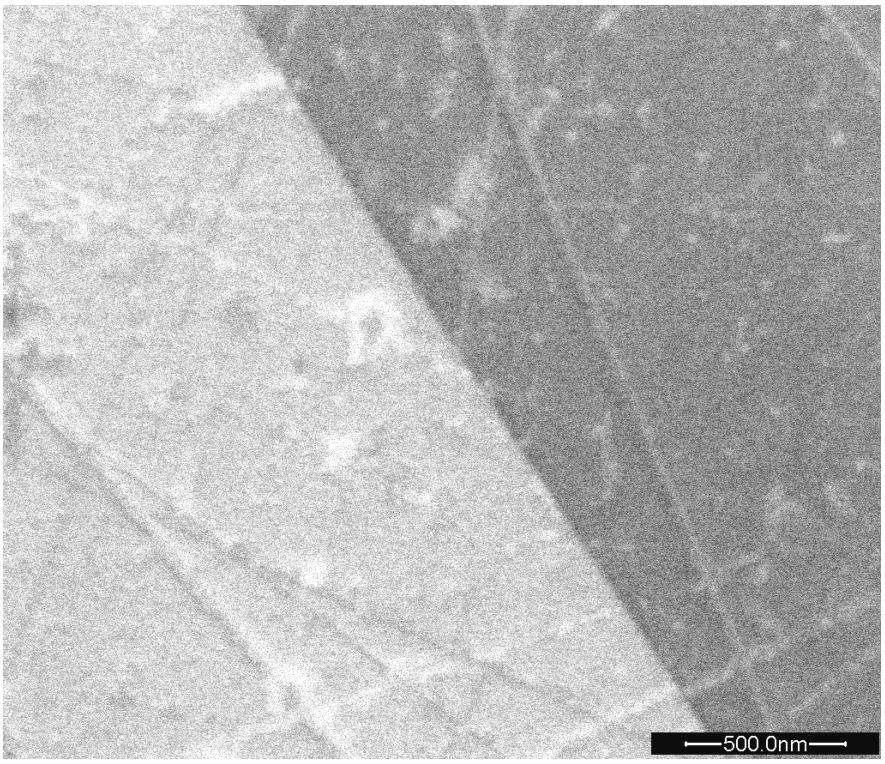

Figure 4.18: Solution treated material.

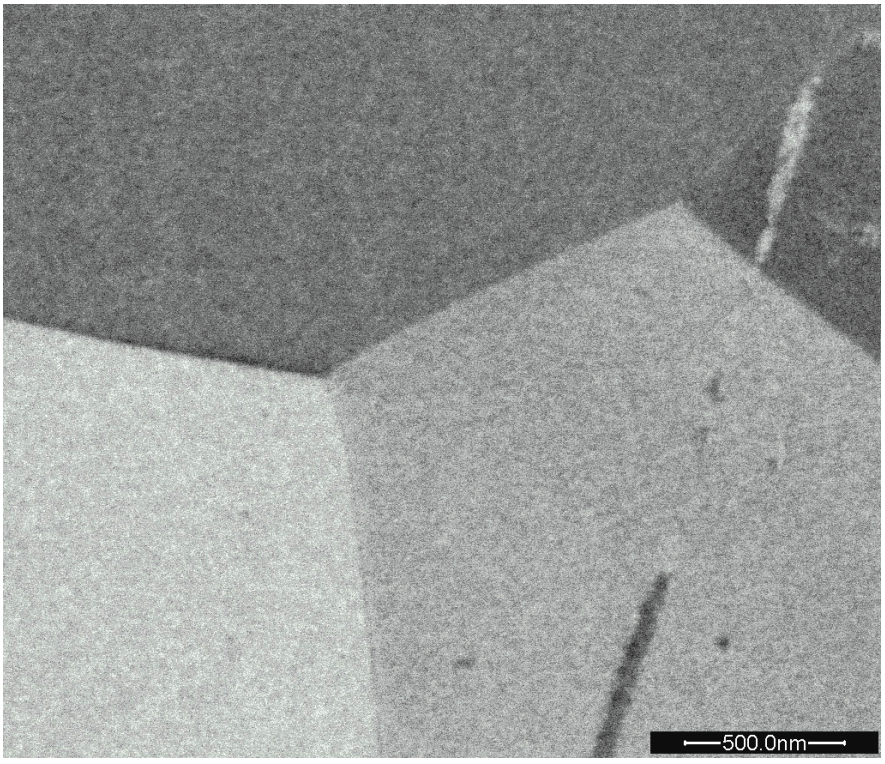

Figure 4.19: Material aged at 375 °C for 4 h.

good agreement with the size found in the literature [37]. This complements results from resistance measurements, where we deduced, that such material should contain ω and α precipitates. The particles are uniformly dispersed throughout

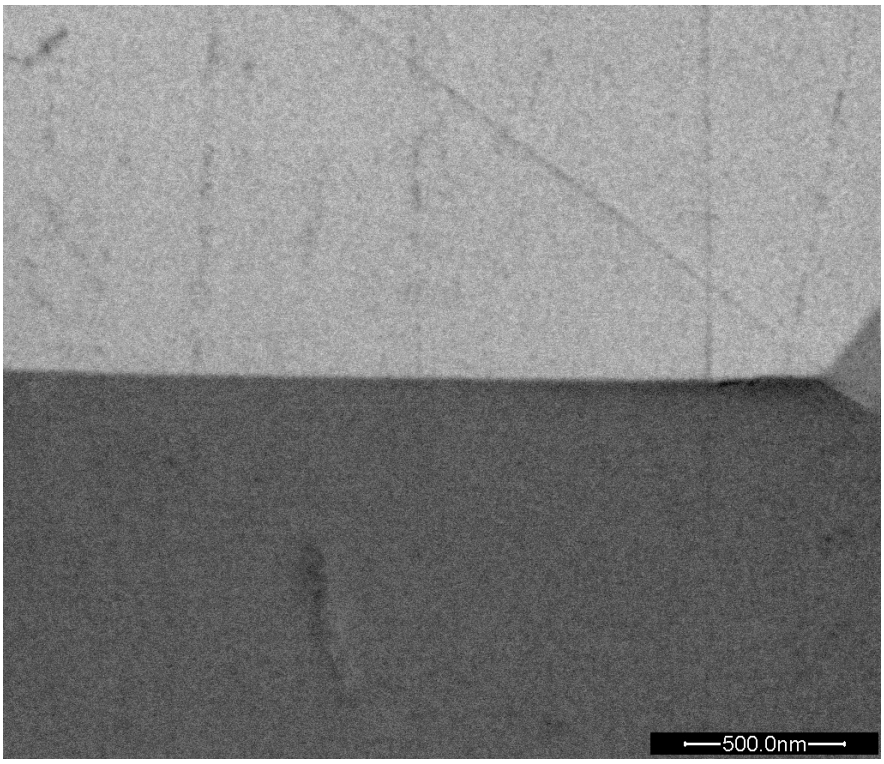

Figure 4.20: Material aged at 375 °C for 16 h.

the grains. On grain boundaries their density is higher.

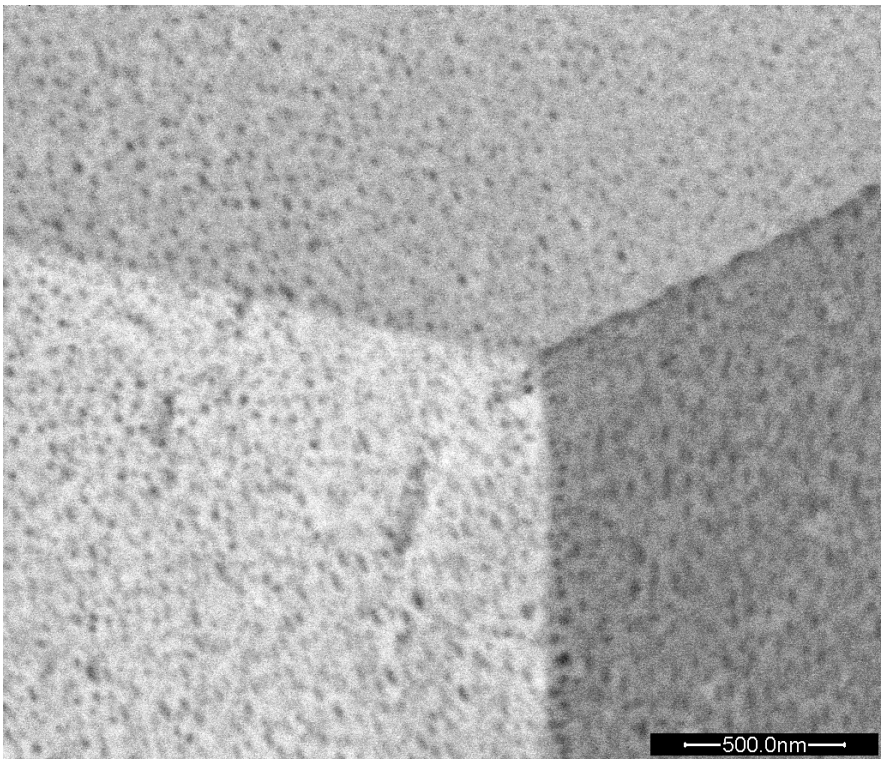

Figure 4.21: Material quenched from 550 °C.

In Fig. 4.22 the microstructure of material quenched from 570 °C is shown. It proves, that black particles from Fig. 4.21 were ω and α precipitates. There is

much less of these particles. The disappeared ones corresponded to ω precipitates. From the analysis of the resistance measurements we concluded, that grown ω_{iso} particles should dissolute at 560 °C. The grain boundaries serve as preferential nucleation sites for the lamellar α precipitates. These α precipitates are known as Widmanstatten side plates. The ω_{ath} particles formed during quenching are again too small to be seen in SEM. However, these statements have to be proved for example by analysis in TEM.

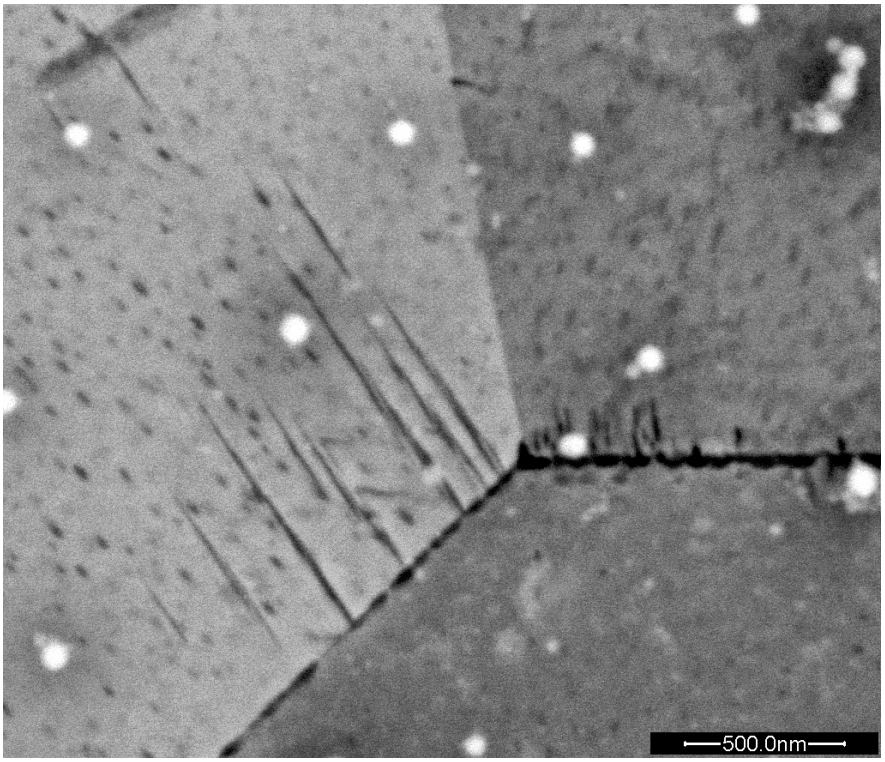

Figure 4.22: Material quenched from 570 °C.

4.3 Differential scanning calorimetry (DSC)

Fig. 4.23 shows record of DSC signal measured during heating. The temperature was increased by 5 °C/min up to 750°C. This rate was chosen not only to observe phase transformations occurring in the material, but also to be in accordance with resistance measurement. Slower heating rate allows to increase time of each phase transformation. Thus, phase transformations overlap less and related DSC peaks are separated. Due to the longer reaction time, greater amount of transformations products could be formed. On the other hand, at higher heating rates, different phase transformation kinetics may lead to observation of fewer peaks and fewer reactions [27].

Explanation of processes taking place in the material is based on previous studies on titanium alloys [37], [40] and resistance measurements done in this study. According to the resistivity results, zone I in Fig. 4.23 (approximately up to 225°C) corresponds to a reversible diffusionless dissolution of athermal ω phase. The carefully calibrated signal from DSC increases in this regime. This might be caused by continuous decrease of thermal capacity corresponding to dissolution

of the ω_{ath}. In zone II (between approximately 225 and 356°C), an irreversible diffusion controlled precipitation of ω_{iso} occurs. Small peak in DSC measurement in this regime can be seen. At higher temperatures (zone III in Fig. 4.23, 356-560°C), the growth of the ω phase is accompanied by heterogeneous nucleation of α phase at ω particles. The growth of the ω phase stops about 480 °C. DSC signal exhibits a weak peak in this region due to the precipitation of the α phase. At 560 °C a sharp change in DSC curve is observed. It indicates an abrupt change of thermal capacity of the material, which is caused by dissolution of the ω_{iso} phase and nucleation of lamellar α phase from grain boundaries. This transformation does not consume any latent heat. The last significant change in DSC signal is observed at 730°C (upper limit of zone IV), which is the temperature of β-transus.

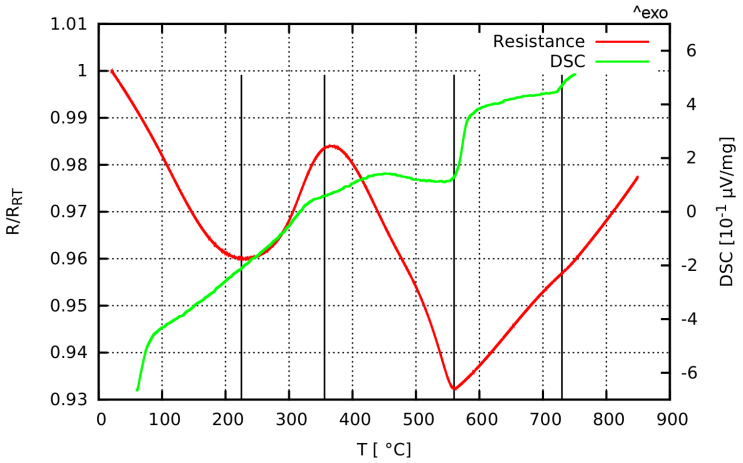

Figure 4.23: The temperature dependence of electrical resistance at the heating rate of 5 °C/min (red curve) and a corresponding DSC measurement at the same heating rate (green curve).

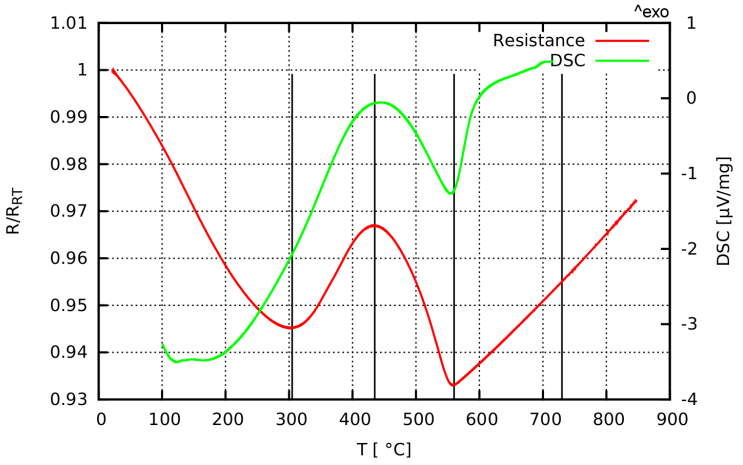

Figure 4.24: The temperature dependence of electrical resistance at the heating rate of 50 °C/min (red curve) and a corresponding DSC measurement at the same heating rate (green curve).

In order to observe the differences between phase transformations occurring in the material at faster heating rates, the measurement with heating rate of

50 °C/min was done. It was the highest heating rate available on equipment used for the measurements. The DSC curve obtained at the heating rate of 50 °C/min is shown in Fig. 4.24 along with the resistance evolution at the same heating rate. The DSC signal has one peak around 440 °C, instead of two small as in Fig. 4.23. Is is caused by high heating rate. Phase transformations overlap. They are detected as one and an inertia of transformations shifts the peak to higher temperatures. However, the dissolution of the ω_{iso} phase does not depend on heating rate and occurs exactly at same temperature as for lower heating rate (at 560 °C). The β-transus could not be detected by this measurement as it was done only up to 700 °C.

4.4 Microhardness testing

It is a known fact [41], that metastable β-Ti alloys can be strengthened by solution treatment and ageing (STA). The value of microhardness should increase with ageing time at low temperature (around 300-400 °C). This increase corresponds to the growth of the ω and α particles. The ω particles form strong and efficient obstacles for dislocation movement due to their small proportions, homogeneous distribution and relatively high volume fraction. The microhardness should steadily increase [7]. As the α phase preferentially nucleates at ω precipitates, the α particles are uniformly distributed throughout the matrix. This hardens the material and improve its the ductility. However, with the increase of ageing time the ω phase dissolves and is replaced by secondary α lamellae and as a result of overageing the hardness decreases [7].

Microhardness measurement was done on samples listed in Table 4.1. In order to obtain a good statistic, ten indentations spaced 0.5 mm apart were made on each sample. The resulting values of microhardness, as well as standard deviation were computed from ten indentations. These values are written in Table 4.1.

Sample	HV1	Deviation
ST	278	14
300 - 4 h	363	6
300 - 16 h	376	5
375 - 4 h	464	5
375 - 16 h	491	6
550	350	3
570	293	10

Table 4.1: Values of Vickers microhardness for different states of material.

If we consider that the ω_{iso} particles and α precipitates, nucleated at the ω phase, harden the material, the results correspond to the previous measurements. The lowest value of microhardness of the ST sample is caused by absence of these hardening phases. The ω_{iso} grows during ageing at 300 °C as does the microhardness. Longer ageing time corresponds to higher volume fraction of ω_{iso}, which results in hardening. At 375 °C the growth of ω phase is even more rapid, than at 300 °C, also some of the ω_{iso} particles get consumed by precipitation of the α phase. Beacause of that, the sample aged at 375 °C for 16 hours has the

highest value of microhardness of the measured samples. The sample quenched from 570 °C contained small volume fraction of the α phase and its microhardness was only little higher than of ST sample. The sample quenched form 550 °C contained little less amount of the α phase, but plenty of the ω_{iso}. Its microhardness is thanks to that higher than for ST and quenched from 570 °C samples.

Conclusions

In the present work, phase transformations in metastable β titanium alloy Ti-15Mo were studied in a wide temperature range (from -196 °C to 850 °C) using in-situ electrical resistance measurement. In order to determine ongoing phase transformation, several aged conditions of the alloy were prepared and their resistance evolution was compared with the solution treated material. This thorough research allowed us to reach unique conclusions about the phase transformations in metastable β titanium alloys. To our knowledge, such detailed study has not been done and published yet. Nevertheless, such research of ageing processes is of great importance, as tailoring the mechanical properties of the material to a specific application requires a good understanding of ongoing phase transformations and their influence on the overall mechanical performance of the alloy. The material was solution treated at 900 °C for 4 hours and subsequently quenched in water. Material prepared that way consists of ω_{ath} particles dispersed in β matrix. The ω precipitates occur during quenching by a shuffle transformation.

The main results of the present work can be summarized as follows:

- Presence of the ω_{ath} particles in solution treated sample was confirmed by TEM. Their size was in order of nanometers. TEM diffraction pattern also confirmed validity of orientation relationship between the ω precipitates and the β matrix.

- In-situ electrical resistance measurement of solution treated sample provided initial insight in temperature limits for each transformation occurring in material during heating. Thanks to this measurement together with its derivative, seven zones, where different processes take place, were distinguished and ongoing transformations were determined:

  - Zone I (lower than 225 °C): Throughout this zone electrical resistivity of the material decreases with increasing temperature. This anomalous resistivity dependence on temperature was observed in temperature interval from -196 °C up to 225 °C and applies even for lower temperatures. During heating, the ω_{ath} dissolves by an inverse shuffle transformation and an elastic strain fields surrounding the ω omega particles are released. It leads to a decrease in conduction electron scattering and therefore the resistance drops. The reversibility of this process was proved by repeated heating up to 80, 90 and 100 °C and cooling to RT.
  - Zone II (225 - 356 °C): In this regime, resistance of solution treated sample increases with temperature. ω_{iso} grow by diffusional irreversible process. With increasing size of ω particles, the value of elastic strain around it also gets higher. Scattering of conduction electron on these strain fields together with thermal vibrations are the reasons for the increase of resistance with temperature. During ageing the relaxation of elastic strain fields probably takes place. It could be caused by diffusion of Mo atoms from the ω precipitates to the β matrix.

- Zone III (356 - 560 °C): Precipitation of α phase causes decrease of electrical resistivity of the material in this zone. The α nucleates preferentially on the ω phase, which results in disappearance of elastic strain at the β/ω interfaces accompanied by decrease of electrical resistivity of the material. The growth of ω_{iso} continues up to 480 °C. The upper limit of this interval corresponds to compete dissolution of the ω phase. This transformation is not dependent on heating rate and always happens at the same temperature.
- Zone IV (560 - 730 °C): There is no longer the ω phase above 560 °C. However, the ω_{ath} forms in a material heated up to zone IV and then quenched. The lamellar α phase nucleates at grain boundaries and the material composition is headed to phase equilibrium.
- Zone V (730 °C and higher): At 730 °C the β-transus occurs and in this regime, the material contains only β phase.
- Zone VI (higher than 385 °C): This zone was introduced because the cooling of the sample was carried out. The material still consists solely of the β phase. If the cooling rate is slow enough, the α phase forms from the β phase.
- Zone VII (385 ° and lower): The onset of this regime corresponds to an increase of electric resistance of the samples during cooling. It indicates forming of the ω phase from the β phase, which shows that the ω_{ath} phase forms even at slow cooling rates (5 °C/min and slower).

- The microstructure evolution of material used for electrical measurements was studied by SEM. The ω_{ath} particles in solution treated sample were too small and did not give any contrast, which makes impossible to observe them in SEM. This applied even for samples aged at 375 °C where the ω and α precipitates could not be observed. In sample quenched from 550 °C the ω and α particles were finally observable. They had rounded shape with diameter about 40 nm. Particles were preferentially grown at grain boundaries and inside grains were uniformly distributed. In sample quenched from 570 °C, besides rounded α precipitates, the lamellar α, which preferentially nucleated at grain β/β boundaries, was observed.

- The resistance measurement of solution treated sample was compared with differential scanning calorimetry. The DSC did not identify transformations occurring at lower temperatures so clearly as resistance measurement did. However, for the dissolution of the ω phase at 560 °C it provided additional information. This process causes step change in thermal capacity of the material and does not consume or release any latent heat.

- The microhardness measurements were done in order to confirm influence of phase transformations on mechanical properties. The highest values of microhardness were reached in the sample aged at 375 °C for 16 hours, because it contained the highest volume fraction of hardening phases (ω_{iso} and α).

The future research of this material will include in-situ TEM observation, which will confirm well founded theories of ongoing phase transformations presented in this work. In-situ X-ray diffraction measurement at cryogenic temperatures is already planned. The unique results of this work will be presented at international conferences and published in scientific journals.

Bibliography

[1] Leyens, C., Peters, M. *Titanium and Titanium Alloys. Fundamentals and Applications.* WILEY-VCH Verlag GmbH & Co. KGaA, Weinheim, 2003. ISBN 3-527-30534-3

[2] Martins, J. R. S., Jr., Nogueira, R. A., de Araújo, R. O., Donato, T. A. G., Arana-Chavez, V. E., Claro, A. P. R. A., Moraes, J. C. S., Buzalaf, M. A. R., Grandini,C. R. *Preparation and Characterization of Ti-15Mo Alloy used as Biomaterial.* Materials Research. 2011. DOI: 10.1590/S1516-14392011005000013.

[3] Ho, W. F., Ju, C. P., Chern Lin, J. H. *Structure and properties of cast binary Ti-Mo alloys.* Biomaterials. 1999.

[4] Ho, W. F. *A comparison of tensile properties and corrosion behavior of cast Ti-7,5Mo with c.p, Ti-15Mo and Ti-6Al-4V alloys.* Journal Alloys and Compounds. 2008.

[5] Wikipedia. *Titanium* Wikipedia, the free encyclopedia, 2014. [Online; accessed 15-May-2014].

[6] Lütjering, G., Williams, J.C. *Titanium.* USA: Springer, 2003. ISBN 3-540-42990-5.

[7] Šmilauerová, J. *Phase transformations and microstructure changes in TIMET LCB alloy.* Master thesis, MFF UK, 2012.

[8] Frost, P. D., Parris, W. M., Hirsch, L. L., Doig, J. R., Schwartz, C. M. *Isothermal transformation of titanium-chromium alloys.* Trans. Am. Soc. Metals, 46:231, 1954.

[9] Hickman, B. S. *The formation of omega phase in titanium and zirconium alloys: A review.* Journal of Materials Science, 4(6):554-563, 1969.

[10] Sikka, S. K., Vohra, Y. K., Chidambaram, R. *Omega phase in materials.* Progress in material science, 27:245-310, 1982.

[11] De Fontaine, D., Paton, N. E., Williams, J. C. *The omega phase transformation in titanium alloys as an example of displacement controlled reactions.* Acta Metalurgica, 19, 1971.

[12] Bagaryatskiy, Yu. A., Tagunova, T. V., Nosova, G. I. Problem Metalloved. Fis. Metallov. (Problems of Metallography and Metal Physics), 5, 1958.

[13] Kuan, T. S., Ahrens, R. R., Sass, S. L. Metal. Trans., 6, 1975.

[14] Paris, H. G. *The relationship between microstructure and mechanical behavior in beta titanium-vanadium alloys.* Thesis, Georgia Institute of Technology, 1975.

[15] Banerjee, S., Mukhopadhyay, P. *Phase Transformations Examples from Titanium and Zirconium Alloys.* Great Britain: Elsevier, 2007. ISBN: 978-0-08-042145-2

[16] Duerig, T. W., Terlinde, G. T., Williams, J. C. *Phase Transformations and Tensile Propeties of Ti-1OV-2Fe-3A1.* Metallurgical and Materials Transactions A, 11(12):1987–1998, 1980.

[17] Williams, J. C., Blackburn, M. J. *The influence of misfit on the morphology and stability of the omega phase in titanium–transition metal alloys.* Transactions of the Metallurgical Society of AIME, 245, 1969.

[18] Ohmori, Y., Ogo, T., Nakai, K., Kobayashi S. *Effects of ω-phase precipitation on $\beta \rightarrow \alpha$, α'' transformations in a metastable β titanium alloy.* Materials Science and Engineering A312, 182–188, 2001.

[19] Nag, S., Banerjee, R., Srinivasan, R., Hwang, J. Y., Harper, M., Fraser, H.L. *ω-Assisted nucleation and growth of α precipitates in the Ti–5Al–5Mo–5V–3Cr–0.5Fe β titanium alloy.* Acta Materialia 57, 2136–2147, 2009.

[20] Prima, Vermaut, P., Texier, G., Ansel, D., Gloriant, T. *Evidence of α-nanophase heterogeneous nucleation from ω particles in a β-metastable Ti-based alloy by high-resolution electron microscopy.* Scripta Materialia 54, 645–648, 2006.

[21] Disegi, J. *Implant Materials. Wrought Titanium – 15% Molybdenum.* Synthes (USA), 2009.

[22] HyperPhysics *Band Theory of Solids.* [Online; accessed 13-July-2014].

[23] Mansfield, M., O'Sulivan, C. *Undestanding Physics.* [Online; accessed 13-July-2014].

[24] Wikipedia contributors. *Electrical resistivity and conductivity.* Wikipedia, the free encyclopedia, 2014. [Online; accessed 14-July-2014].

[25] Zhigilei, L.V. *Introduction to the Science and Engineering of Materials.* Lecture notes.

[26] NETZSCH. *Functional principle of a heat-flux DSC.* [Online; accessed 14-July-2014].

[27] Schawe, J., Riesen, R., Widmann, J., Schubnell, M., Jörimann, U. *Interpreting DSC curves.* METTLER TOLEDO GmbH (Schweiz), 2000.

[28] Nebesářová, J. *Elektronová mikroskopie pro biology.* [Online; accessed 16-July-2014].

[29] Fyzikální praktikum MFF UK. *Určení strukturních parametrů krystalických látek metodami scanovací elektronové mikroskopie (SEM).* [Online; accessed 13-July-2014].

[30] Gordon England. *Vickers Hardness Test.* [Online; accessed 15-July-2014].

[31] Wikipedia contributors. *Vickers hardness test.* Wikipedia, the free encyclopedia, 2014. [Online; accessed 15-July-2014].

[32] Wikipedia contributors. *Kilogram-force.* Wikipedia, the free encyclopedia, 2014. [Online; accessed 15-July-2014].

[33] Pavlina, E.J., Van Tyne, C.J. *Correlation of Yield Strength and Tensile Strength with Hardness for Steels.* Journal of Materials Engineering and Performance 17, 888–893, 2008.

[34] Poková, M. *Mikrostruktura nerovnovážných tuhých roztoků na bázi Al-Mn.* Master thesis, MFF UK, 2010.

[35] Pennock, G.M., Flower, H.M., West, D.R.F. *The Thinning Transformation in β Ti-Mo Alloys.* Metallography 10, 43-53, 1977.

[36] Ho, J. C., Collings, E. W. *Anomalous Electrical Resistivity in Titanium-Molybdenum Alloys.* Phys. Rev. B 6, 3727-3738, 1972.

[37] Gloriant, T., Texier, G., Sun, F., Thibon, I., Prima, F., Soubeyroux, J.L. *Characterization of nanophase precipitation in a metastable β titanium-based alloy by electrical resistivity, dilatometry and neutron diffraction.* Scripta Materialia 58, 271-274, 2008.

[38] Ho, W. *Effect of Omega Phase on Mechanical Properties of Ti-Mo Alloys for Biomedical Application.* Journal of Medical and Biological Engineering 28, 47-51, 2007.

[39] Prima, F., Vermaut, P., Thibon, I., Ansel, D., Debuigne, J., Gloriant, T. *Nanostructured Metastable β-Titanium based Alloy.* Materials Science Forum Vols. 386-388, 307-314, 2002.

[40] Prima, F., Thibon, I., Ansel, D., Debuigne, J., Gloriant, T. *ω precipitation in a beta metastable titanium alloy, resistometric study.* Materials transactions-JIM 41(8), 1092–1097, 2000.

[41] Fujii, H. *Strengthening of $\alpha + \beta$ titanium alloys by thermomechanical processing* . Materials Science and Engineering A243, 103–108, 1998.

List of Tables

List of Figures

List of Abbreviations

CP	commercially pure
hcp	hexagonal close-packed
bcc	body-centered cubic
G	Gibbs free energy
ST	solution treated
RT	room temperature
SEM	scanning electron microscopy
BSE	back-scattered electrons
SE	secondary electrons
EDX	energy-dispersive X-ray
DSC	differential scanning calorimetry
BF	bright field
DF	dark field
TRC	temperature resistivity coefficient
R	electrical resistance
T	temperature
STA	solution treatment and ageing

Attachments

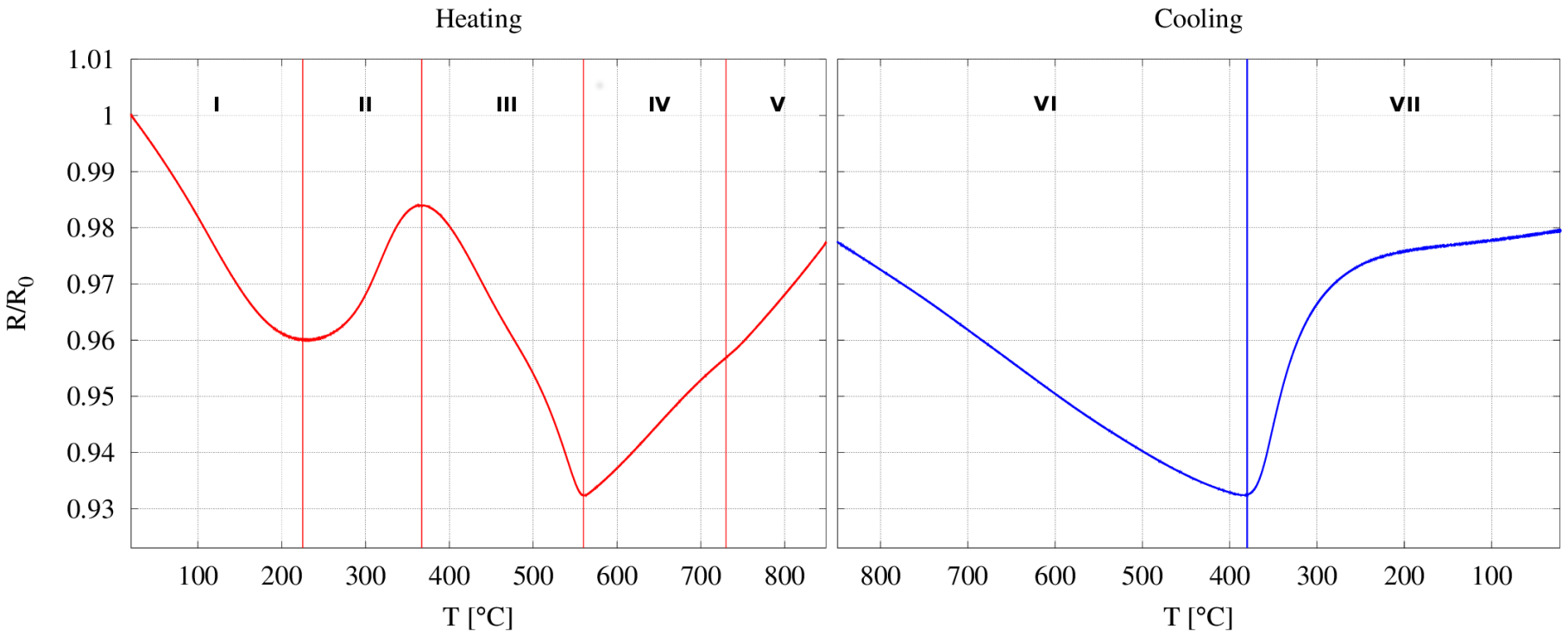

Figure 4.25: The dependence of electrical resistance on temperature.

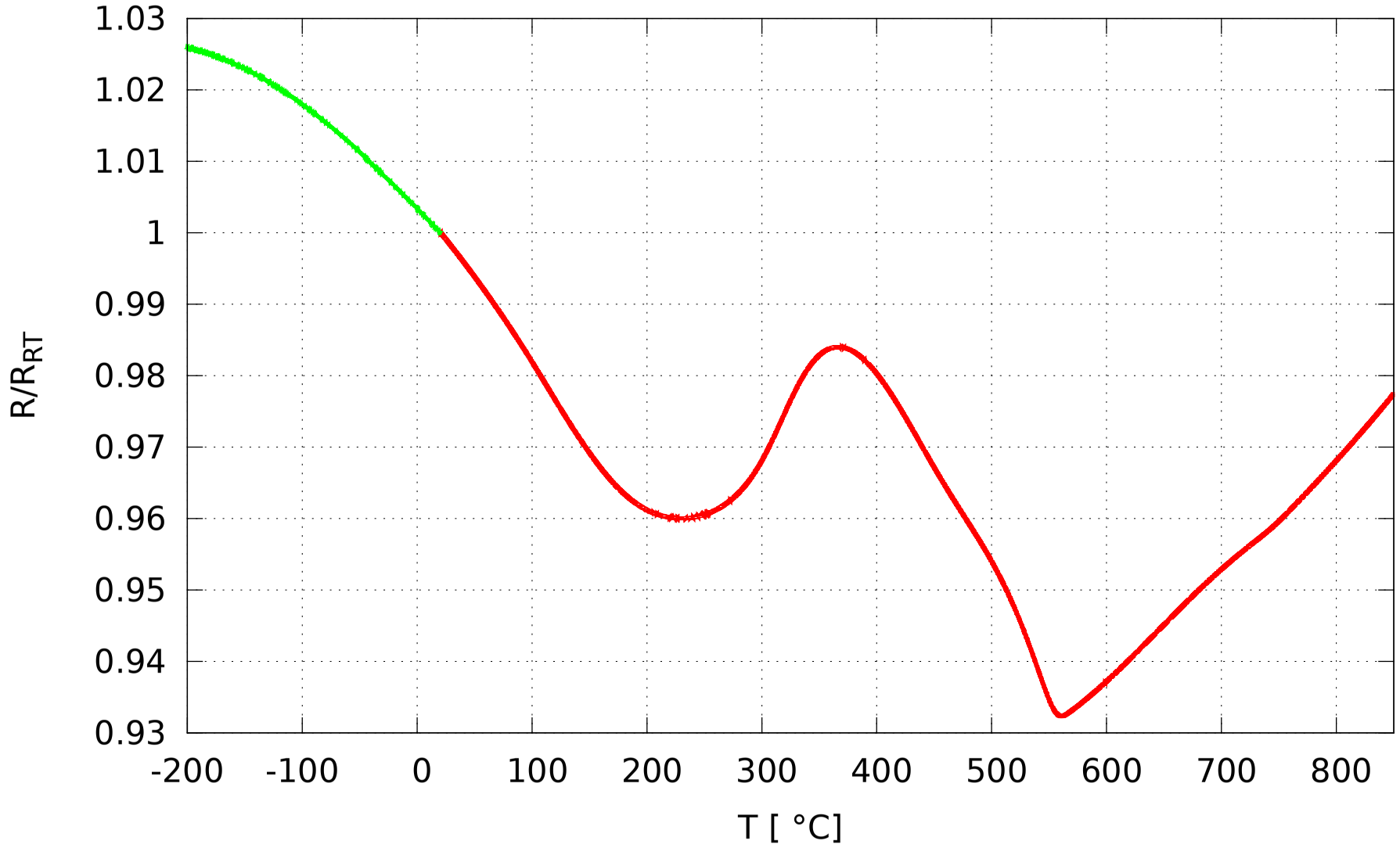

Figure 4.26: The dependence of electrical resistance on temperature from -200 °C to 850 °C.

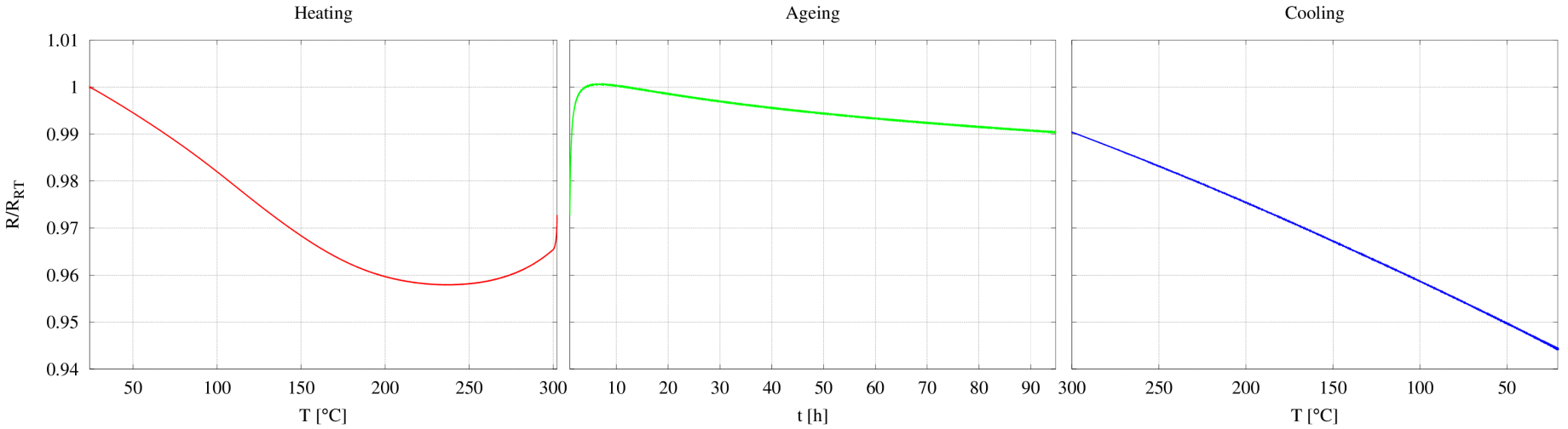

Figure 4.27: The record of measurement of electrical resistance during heating, ageing (at 300 °C) and cooling back to RT.

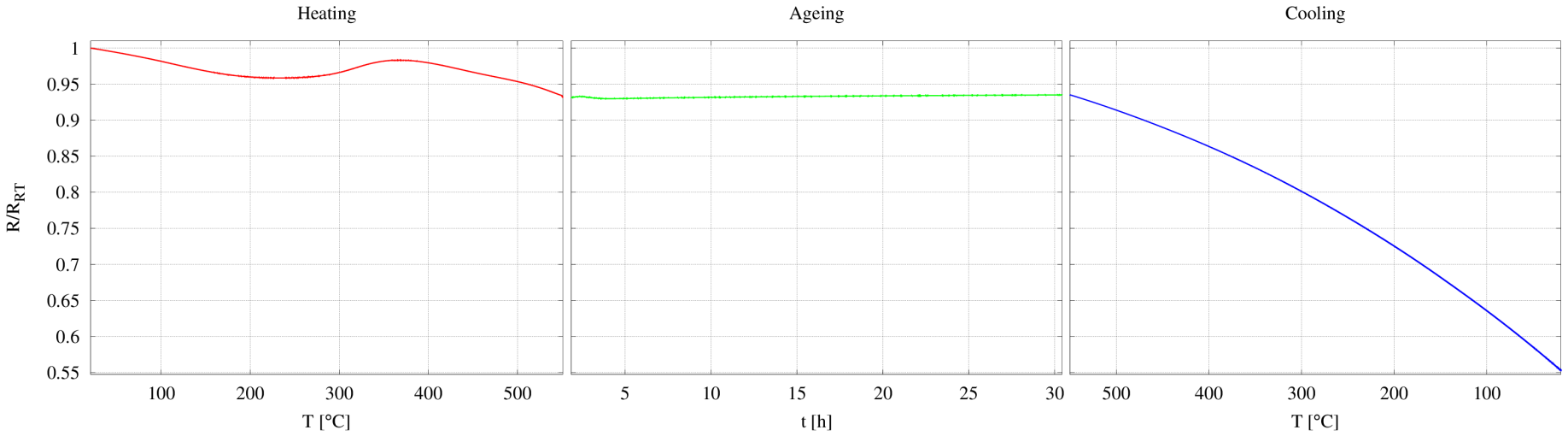

Figure 4.28: The record of measurement of electrical resistance during heating, ageing (at 550 °C) and cooling back to RT.

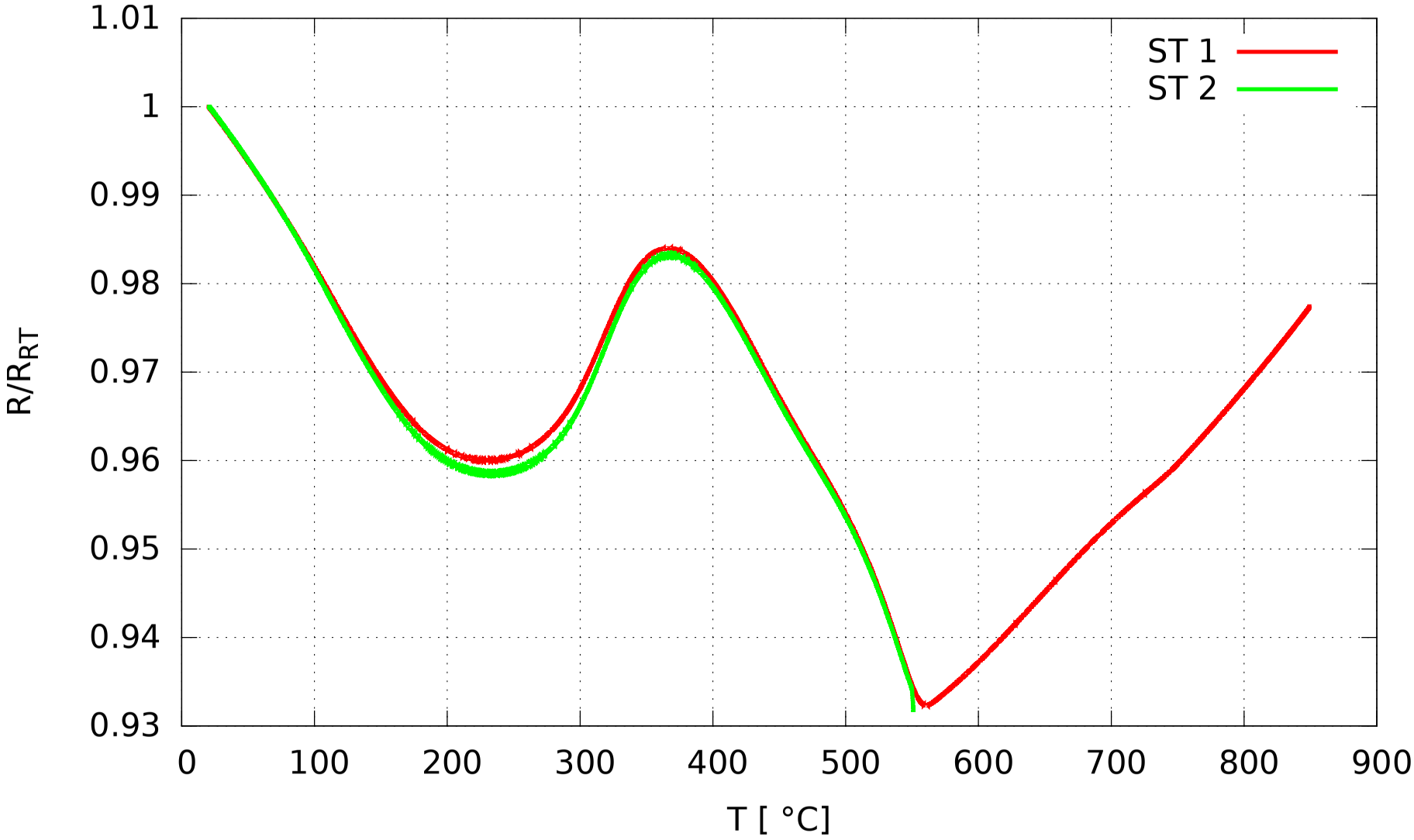

Figure 4.29: Comparison of the electrical resistance for two solution treated samples, where the sample 2 is the aged one.

Materials Science & Engineering A 651 (2016) 886–892

Contents lists available at ScienceDirect

Materials Science & Engineering A

journal homepage: www.elsevier.com/locate/msea

Thermal stability of ultrafine-grained commercial purity Ti and Ti–6Al–7Nb alloy investigated by electrical resistance, microhardness and scanning electron microscopy

Pavel Zháňal [a], Kristína Václavová [a], Branislav Hadzima [b], Petr Harcuba [a], Josef Stráský [a], Miloš Janeček [a,*], Veronika Polyakova [c], Irina Semenova [c], Michal Hájek [a], Kaveh Hajizadeh [d]

[a] Department of Physics of Materials, Charles University, Ke Karlovu 5, 12116 Prague, Czech Republic
[b] University of Žilina, Žilina, Slovak Republic
[c] Ufa State Aviation Technical University, Ufa, Russia
[d] Sahand University of Technology, Tabriz, Iran

ARTICLE INFO

Article history:
Received 3 September 2015
Received in revised form
1 November 2015
Accepted 9 November 2015
Available online 10 November 2015

Keywords:
Ti alloys
Thermal stability
Electrical resistance
Microhardness

ABSTRACT

Ultrafine-grained (UFG) commercial purity Ti and Ti–6Al–7Nb alloy produced by equal channel angular pressing (ECAP) were investigated in this study. In-situ electrical resistance measurements conducted on ultra-fine grained and coarse grained material during linear heating revealed different behaviors of UFG material. Electrical resistance measurements were capable to detect recovery and recrystallization processes in UFG material. Thermal stability of UFG structure was further investigated by microhardness measurements and scanning electron microscopy.

1. Introduction

Titanium and titanium alloys are increasingly used for load bearing orthopedic implants of big joints as well as for dental implants [1–3]. Main advantages of these materials include extreme corrosion resistance, sufficient biocompatibility, and moderate elastic modulus [4]. The demand for smaller load-bearing and dental implants formulates a need for stronger material. However, high-strength β-Ti alloys developed for an aircraft industry cannot be used for biomedical applications because of high content of toxic elements, such as vanadium [5,6].

An alternative option for strength and fatigue resistance enhancement is manufacturing ultra-fine grained Ti and Ti alloys by severe plastic deformation (SPD) [7,8].

The UFG commercial purity titanium (CP Ti) and Ti–6Al–4V alloy have already been prepared by SPD techniques and extensively investigated by many authors [9–11]. Improved mechanical properties of UFG Ti and Ti alloys were already reported. For example, the fatigue limit of UFG Ti–6Al–4V alloy is increased by 10–15% compared to the coarse-grained material [12–14] and the strength is increased by 20% [15]. Moreover, UFG materials exhibit also higher corrosion resistance and improved biocompatibility as compared to their coarse grained (CG) counterparts [16,17].

Ti–6Al–7Nb alloy has been developed as a biocompatible alternative to the common Ti–6Al–4V alloy. It belongs to α+β alloys which contain both phases at room temperature. Its β-transus temperature is 1010 °C [18]. UFG microstructure of Ti–6Al–7Nb alloy has already been studied and superior mechanical properties of UFG material were reported [19,20]. Recently, other biocompatible UFG β-Ti alloys have also been thoroughly investigated [21–24].

In contrast to a wide range of studies analyzing mechanical properties of the UFG Ti and its alloys, the thermal stability has rarely been addressed, despite its importance for further processing of UFG material. In their study Hoseini et al. showed that UFG commercially pure titanium is thermally stable after isothermal annealing at 450 °C for 6 h [25].

The principal objective of this study is to investigate the UFG microstructure and thermal stability of CP Ti and Ti–6Al–7Nb alloy focusing on the recovery and recrystallization. Precise electrical resistance measurement in-situ during linear heating was utilized. Recovery and recrystallization were previously studied by in-situ electrical resistance measurements in copper based alloys and composites or in the Ni–Ti compound [26–28]. To our knowledge, there was no attempt to study the recovery and recrystallization

* Corresponding author.
E-mail address: janecek@met.mff.cuni.cz (M. Janeček).

http://dx.doi.org/10.1016/j.msea.2015.11.029
0921-5093/

by in-situ electrical resistance measurements in UFG Ti and its alloys.

2. Experimental

Commercial purity Ti Grade 4 (CP Ti) and Ti–6Al–7Nb alloy were procured by ATI Alvac Ltd. in as-rolled condition and processed by equal channel angular pressing [29]. The chemical composition of both studied materials is listed in Tables 1 and 2.

2.1. Preparation of CP Ti

The rod of CP Ti was pressed through the round channel ECAP die with the diameter of 15 mm. The channel angle was $\Phi = 105°$ and the corner angle $\Psi = 20°$. The temperature of the die during pressing ranged between 300 and 310 °C. The billets were pressed six times via the route B_C at a constant ram speed of 1 mm/s. A detailed study of the ECAP processing of CP Ti can be found in [30]. Reference coarse-grained material was prepared by annealing of the as received material at 800 °C/2 h followed by slow furnace cooling.

2.2. Preparation of Ti–6Al–7Nb alloy

Ti–6Al–7Nb alloy was thermally treated before processing by ECAP. The thermal treatment consisted of two annealing steps. The first step included annealing at 985 °C (a temperature just below β-transus) for one hour followed by water quenching. In the second step annealing at 780 °C for 4 h was applied. After this thermal treatment the material has a standard 'duplex' structure, which consists of 18 vol% of primary α-phase. This microstructure condition allowed the successful material processing by ECAP.

The round ECAP die with the diameter of 20 mm and angles $\Phi = 120°$ and $\Psi = 0°$ was employed. The samples were also pressed six times (6 passes) at 600 °C. Subsequently, extrusion to 10 mm was applied at 300 °C. Finally the material was aged at 500 °C for 1 h to achieve the maximum strength. More details about material and its processing can be found in [31]. Reference coarse-grained material which underwent the same thermal treatment path without subsequent working was used for microhardness comparison. For resistivity measurements, as-received material in as-rolled condition was used as a coarse-grained counterpart of the material after ECAP.

2.3. Experimental procedure and sample preparation

The principal experimental method used in this study is the in-situ measurement of electrical resistance by employing a precise self-made apparatus. A standard four-point method was employed. Voltage and electrical current were measured simultaneously using nanovoltmeter Keithley 2182 and SourceMeter Keithley 2400 devices, respectively. The samples were placed in a specially designed furnace which allows precise heating of the sample in a protective argon atmosphere. The relative error of such measurement is lower than 10^{-4} within each measured point and two experimental values are acquired per second [32]. The dynamics of microstructural changes can be thus assessed.

The electrical resistance was measured during linear heating with the rate of 5 °C/min up to 700 °C and 800 °C for CP Ti and Ti–6Al–7Nb alloy, respectively. UFG conditions of both materials were investigated along with their annealed (non-deformed) counterparts.

Table 1
Chemical composition of CP Ti Grade 4.

Element	Ti	Fe	C	H	N	O	Others
wt%	Balance	0.50	0.08	0.0125	0.05	0.40	0.40

Table 2
Chemical composition of Ti–6Al–7Nb alloy.

Element	Ti	Nb	Al	Fe	V	C	O	N	Others
wt%	Balance	6.94	6.06	0.15	< 0.05	0.01	0.17	0.0027	< 0.05

The evolution of the microhardness in specimens heated to three different temperatures in both materials was studied. A force of 0.5 kgf and the dwell time of 10 s were applied. Microhardness was evaluated at the plane perpendicular to processing direction. The resulting values of microhardness, as well as the standard deviation were computed from 20 indentations. At least 0.2 mm was ground from the surface before each measurement to remove possible oxidic surface layer.

For CP Ti LECO M-400-A microhardness tester was employed and the data were evaluated by Lucia Hardness program. Measurements were carried out in a single sample, which was repeatedly aged for 30 min at a given temperature and then quenched into water. The microhardness of Ti–6Al–7Nb alloy was measured by QNESS A10+ tester with automatic indentation and evaluation using QPix Control program. The microhardness of Ti–6Al–7Nb alloy was measured in three different samples heated up to three different temperatures based on electrical resistivity measurement results described below.

Microstructure changes in both materials were observed by high resolution scanning electron microscope FEI Quanta 200 FEG operated at 20 kV using backscattered electrons. Employing of Z-contrast allowed distinguishing of α and β phases in Ti–6Al–7Nb alloy and the channeling contrast revealed the grain structure of the material. The microstructure evolution of both materials in UFG condition before and after subsequent heating was investigated.

The samples for scanning electron microscopy (SEM) observations were heated with the heating rate of 5 °C/min up to selected temperatures and then water quenched. The temperatures were selected according to the results of electrical resistance measurements, cf. Figs. 1 and 2. The linear heating using the same rate assures that the sample is in a comparable microstructural condition as during the in-situ resistance measurement at the same temperature. Specimens for SEM observations were prepared by automatic grinding using special grinding mode in Struers Accutom 50 precision cut-off machine (0.3 mm removed), followed by standard metallographic grinding and three-step vibratory polishing.

3. Results

3.1. In-situ electrical resistance measurements

Fig. 1a shows the temperature dependence of resistance of CP Ti after ECAP and of the reference coarse-grained material. The relative resistance R/R_0, where R is the resistance measured at the given temperature T and R_0 is the resistance at room temperature, is plotted at the vertical axis. During linear heating up to 700 °C the resistance increases almost three times. Initially, the resistance increases linearly, whereas above 300 °C it deviates slightly from linearity. Small difference between annealed and ECAPed samples is observed.

The first and the second derivatives of relative resistance with respect to temperature, which were computed numerically and

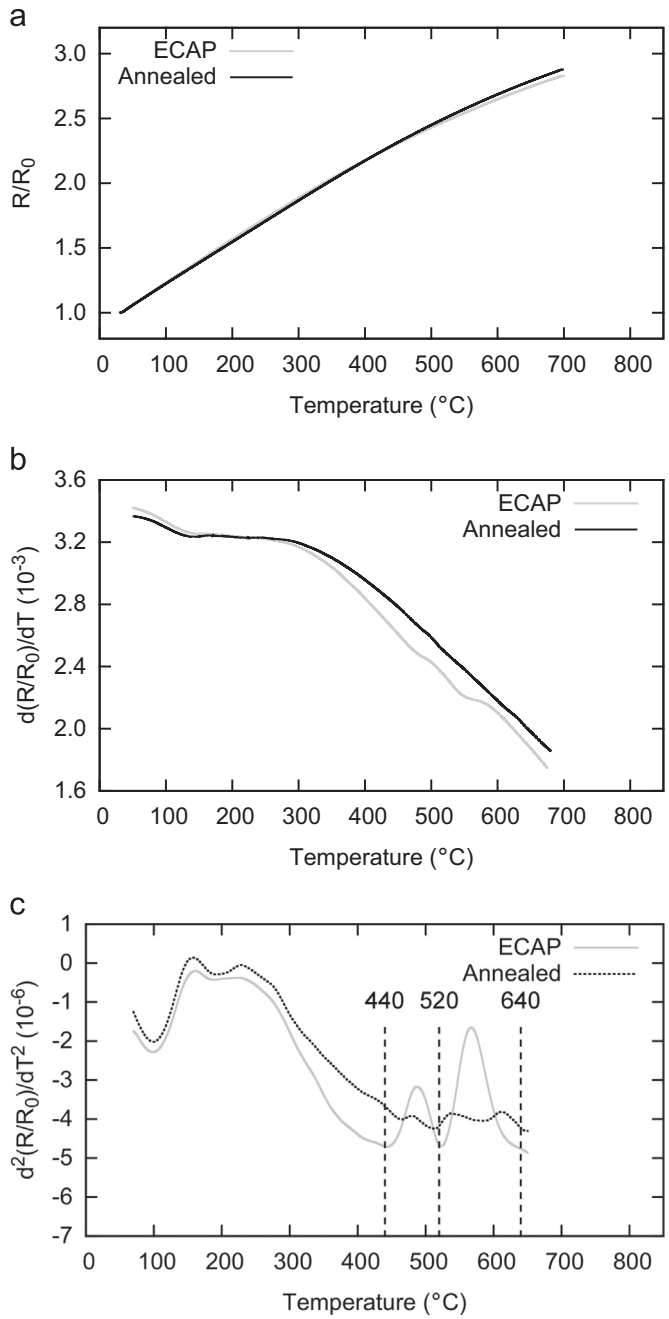

Fig. 1. Relative resistance variations of CP Ti during heating (a) linear temperature dependence, (b) the first derivative of relative resistance, and (c) the second derivative of relative resistance (temperatures chosen for SEM observations are highlighted).

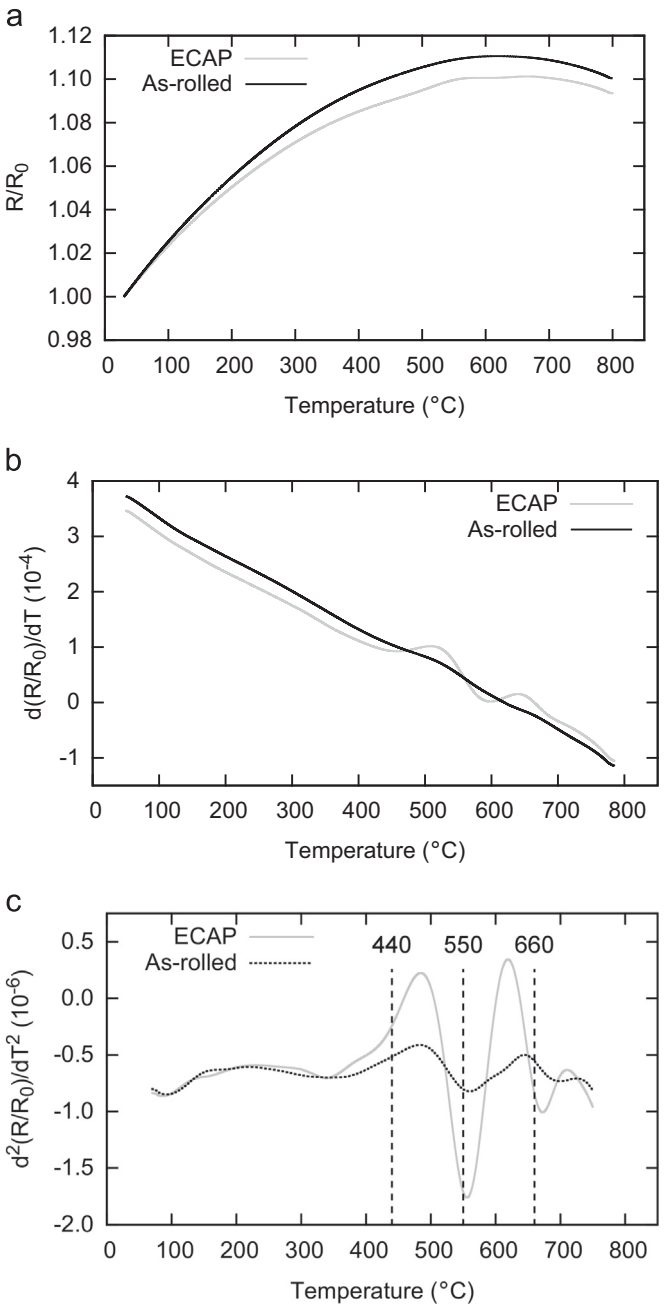

Fig. 2. Relative resistance variations of Ti–6Al–7Nb alloy during heating (a) linear temperature dependence, (b) the first derivative of relative resistance, and (c) the second derivative of relative resistance (temperatures chosen for SEM observations are highlighted).

smoothed using Savitzky–Golay algorithm [33], are shown in Fig. 1b and c, respectively. Fig. 1b shows the first derivative. Both curves are similar except for two small deviations for ECAPed specimen at about 500 °C and 600 °C. Those deviations appear as clear peaks in the plot of the second derivative in the Fig. 1c. Based on the assumption that these peaks correspond to undergoing microstructural changes, the temperatures of 440 °C, 520 °C and 640 °C were chosen for subsequent heating and microstructural observations. The other peaks in the second derivative appear in both curves and therefore they do not represent differences caused by ECAP processing of the material.

The results of the resistance measurements of Ti–6Al–7Nb alloy are presented in the similar way as for CP Ti. Fig. 2a shows the temperature dependence of the relative resistance for the UFG Ti–6Al–7Nb alloy after ECAP and in the as-rolled condition. The relative resistance increases only by approx. 10%, which contrasts to almost 300% increase in CP Ti, cf. Fig. 1. The difference between the ECAP condition and the reference material is therefore better visible in Fig. 2a. Both curves are similar (concave) up to 650 °C and for higher temperatures the electrical resistance even declines. Fig. 2b shows the first derivative with respect to the temperature with two distinct peaks around 500 °C and 650 °C for the ECAPed material. The differences between the two conditions are accentuated by plotting the second derivative of the electrical resistance in Fig. 2c. The temperatures of 440 °C, 550 °C and 660 °C were chosen for microstructure observations by SEM.

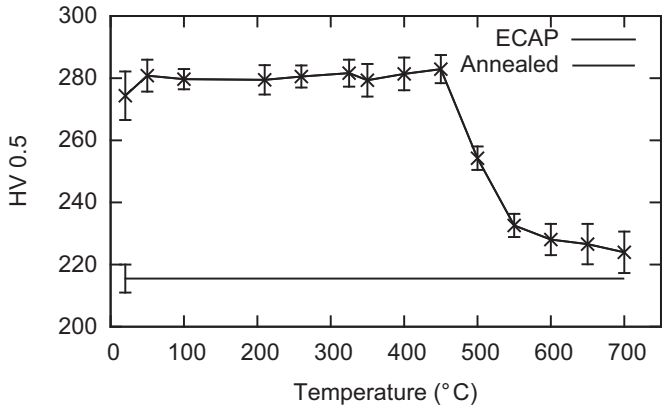

Fig. 3. Evolution of microhardness of ECAPed and annealed CP Ti with temperature.

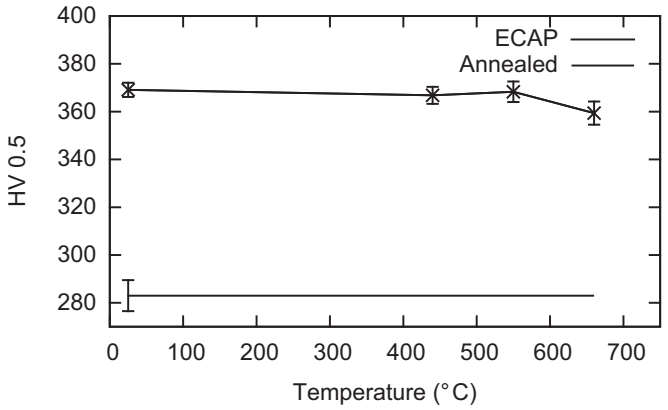

Fig. 4. Evolution of microhardness of ECAPed and annealed Ti–6Al–7Nb with temperature.

3.2. Microhardness measurements

The thermal stability of ECAPed samples was studied by microhardness measurements. The evolution of microhardness of CP Ti sample processed by ECAP with ageing temperature is shown in Fig. 3.

As expected the microhardness of the ultra-fine grained material after ECAP is significantly higher than that of the annealed sample. The values of microhardness remain constant (HV∼280) up to the ageing temperature of 450 °C and then decrease rapidly approaching values of annealed material (HV∼215) at 700 °C. This behavior is consistent with the resistance measurement, which shoved a small bump in the first derivative at around 500 °C, cf. Fig. 1b.

The Vickers microhardness as a function of ageing temperature of the Ti–6Al–7Nb alloy in the as-annealed and ECAPed specimens is shown in Fig. 4. The microhardness variations in specimens heated up to the three different temperatures specified by electrical resistance measurement (440 °C, 550 °C and 660 °C) was investigated. The annealed sample exhibited the lowest microhardness (HV∼283) which was almost independent of the temperature of ageing. The deformation by ECAP resulted in the increase of the microhardness of the sample up to HV∼370. The microhardness of ECAPed specimen remained almost constant in specimens heated to 400 °C and 550 °C. Only heating to the highest temperature (660 °C) resulted in a slight decrease of HV. However, the decrease of HV is much lower than in CP Ti, cf. Fig. 3. Moreover, the microhardness of ECAPed specimens remains much higher than that of the annealed material in the whole investigated temperature range.

3.3. SEM observations

Microstructure changes of the UFG material after ECAP occurring during linear heating were investigated by scanning electron microscopy. Three conditions corresponding to linear heating to the three temperatures selected from electrical resistance measurements were selected for SEM observations.

Fig. 5 displays the microstructure of CP Ti. In Fig. 5a the ultra-fine grained microstructure of material after ECAP is shown. White dots in the SEM micrograph represent iron enriched β-Ti particles, which are common in commercially pure Ti. Enhanced Fe content (10 wt%) in these particles was proved by EDAX analysis. Due to the very low volume fraction of these particles one may assume that they influence the electrical resistance evolution only marginally. Moreover, from micrographs in Fig. 5 it is evident that these particles did not evolve during used thermal treatment.

The microstructure of the material is typically heavily deformed containing grains of the average size around 1 μm [8,29]. No significant change of the microstructure was observed in the sample aged up to 440 °C, see Fig. 5b. On the other hand, the microstructure of the sample aged to 520 °C differs significantly as can be seen in Fig. 5c. The grains are much clearer, which indicates that some recovery process, probably annihilation of dislocations, occurred during heating between 440 °C and 520 °C. Grain size also slightly increased, which indicates limited grain growth. The dark spots in the micrograph are artifacts caused by polishing, namely parts of grains which disengaged from the surface during vibratory polishing. The microstructure of the specimen heated up to 640 °C is shown in Fig. 5d. Material is completely recrystallized with grains of the average size of approximately 5 μm.

The microstructures of UFG Ti–6Al–7Nb alloy are shown in Fig. 6. The material after ECAP, shown in Fig. 6a has the typical ultra-fine grained duplex microstructure consisting of approximately 20% of heavily deformed primary α-phase and significantly fragmented α+β region, which contains slightly elongated β-phase particles appearing white in the micrograph due to the Z-contrast. Fig. 6b shows the microstructure of ECAPed specimen, which was subsequently heated up to 440 °C. There are no observable changes in the microstructure as compared to the as ECAPed specimen. Fig. 6c corresponds to the material heated up to 550 °C. Detail inspection of the micrograph reveals very low fraction of small grains in α+β region with very clear contrast suggesting that these are newly formed dislocation-free grains. Also β-phase particles are slightly more equiaxed. Finally, in Fig. 6d the microstructure of the specimen heated up to 660 °C is displayed. The microstructure is partly recrystallized containing grains >1 μm in the originally heavily fragmented α+β region. White β-phase particles are significantly bigger and more equiaxed.

4. Discussion

4.1. Resistance evolution

The electrical resistance of CP Ti during heating up to 700 °C increased approximately three times as compared to the room temperature. This is a typical behavior of commercial purity titanium. More specifically, the resistivity increase in CP Ti depends on the amount of impurities (mainly oxygen). Our results for CP Ti Grade 4 are consistent with other authors [34]. Much smaller increase of resistance (by only 10%) in Ti–6Al–7Nb alloy as compared to CP Ti confirms the well-known fact that the structural/compositional component of resistance in alloyed systems is of higher magnitude than the temperature dependent component [35].

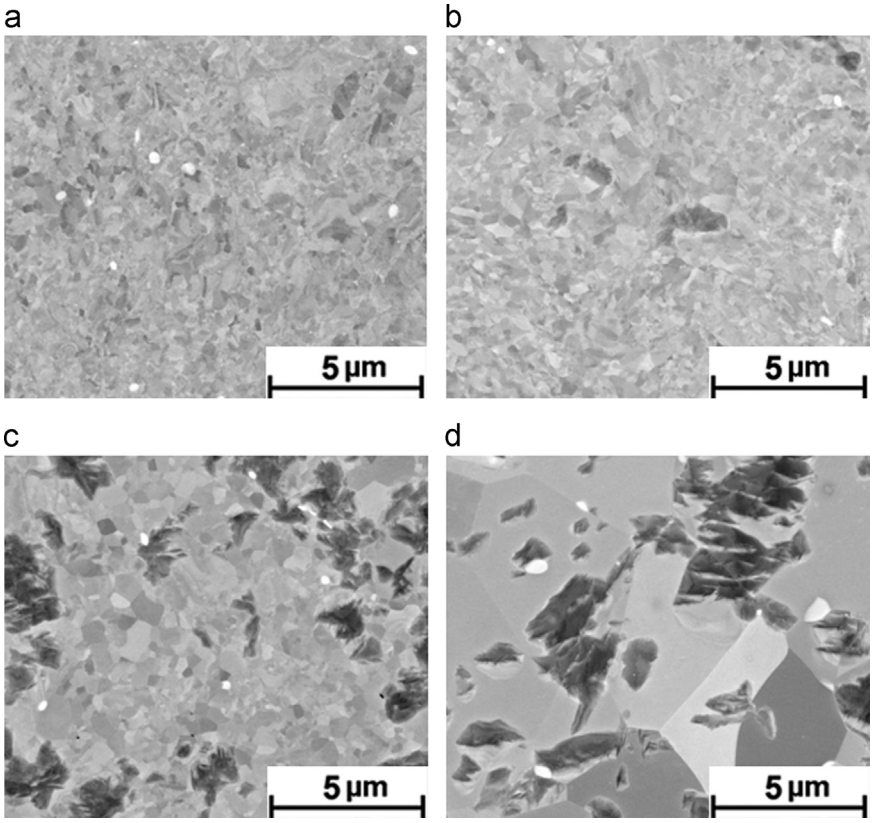

Fig. 5. Microstructure evolution of ultra-fine grained CP Ti (a) as ECAPed, (b) heated to 440 °C, (c) heated to 520 °C, and (d) heated to 640 °C.

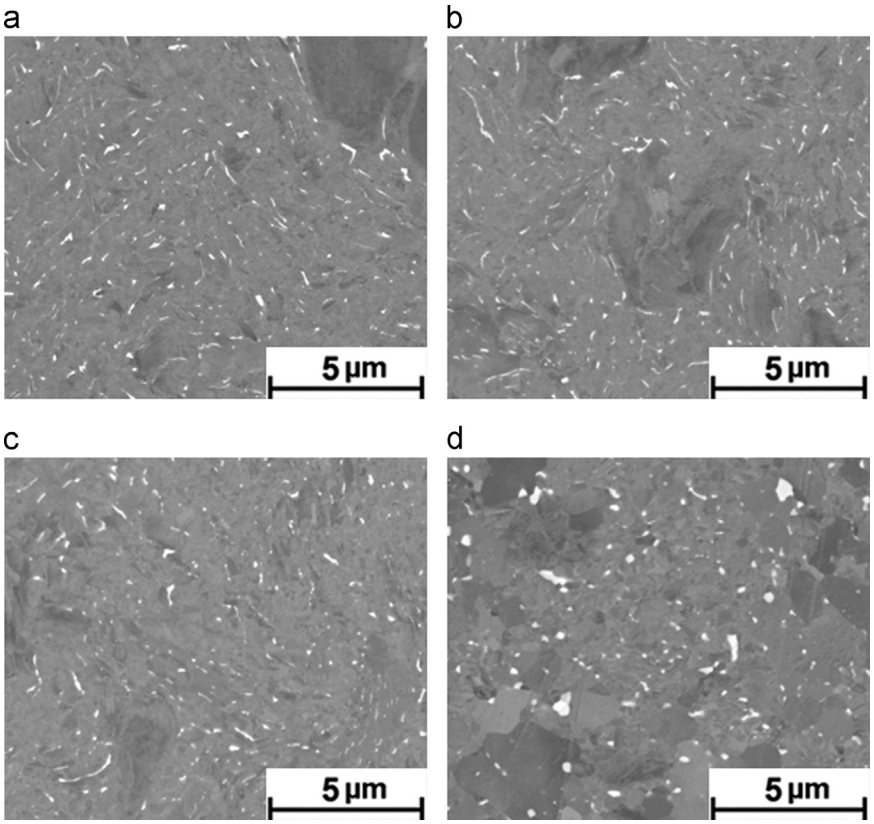

Fig. 6. Microstructure evolution of ultra-fine grained Ti–6Al–7Nb (a) as ECAPed, (b) heated to 440 °C, (c) heated to 520 °C, and (d) heated to 640 °C.

The decrease in the resistance in Ti–6Al–7Nb alloy above 700 °C is caused by increasing equilibrium amount of β-phase with increasing temperature. Note, that the alloy Ti–6Al–4V containing approximately 15% of β-phase particles at 750 °C and 20% of β-phase particles at 800 °C, exhibited the similar resistance decrease [36].

The most important result is the clear difference in resistance evolution between ultra-fine grained materials and their coarse-grained counterparts. The difference is more apparent in the Ti–6Al–7Nb alloy and is probably caused by more pronounced structural effect on overall resistance than in CP Ti. In the CP Ti, the difference in resistance evolution is almost certainly caused by recovery and/or recrystallization as no structure changes occur in the investigated temperature range. We assume that recrystallization and/or recovery is also responsible for the differences in resistivity evolution in Ti–6Al–7Nb. However, in this alloy other effects including changes in β-phase morphology, reduced amount of phase interfaces and also increasing equilibrium amount of β-phase at elevated temperatures are expected to influence the resistance.

4.2. Effect of thermal processing on microhardness of both materials

The ECAPed samples of CP Ti heated up to 450–500 °C exhibit nearly constant values of microhardness. Around these temperatures, the recovery of the material begins and the microhardness declines. The microhardness data are consistent with the resistance measurements. The SEM revealed that material recovery/recrystallization is responsible for the first bump in the first derivative of resistance and the decrease of materials microhardness.

Similarly as in CP Ti, the microhardness of the UFG Ti–6Al–7Nb alloy remains constant during heating up to 440 °C and 550 °C. Note that both annealed and ECAPed samples of Ti–6Al–7Nb alloy were in the last step heat treated at 500 °C for 1 h, which is considered as a strength increasing heat treatment [37,38]. Heating of ECAPed samples up to 440 °C and 550 °C does not affect the microhardness, despite an obvious response of resistivity, which is attributed to the recovery process. It is therefore assumed that an initial stage of the recovery process has only a negligible effect on microhardness. Heating of the sample up to 660 °C leads to the slight decrease of the microhardness. The effect of heating on microhardness is much lower in Ti–6Al–7Nb alloy than in CP Ti partly due to solid solution strengthening and more importantly due to strengthening by phase interfaces.

4.3. Microstructural changes in CP Ti observed by SEM

SEM observations of CP Ti did not reveal any microstructure change after heating up to 440 °C. It is consistent with the resistance and microhardness measurements and also with other authors' observations [25]. No thermally activated process in CP Ti during heating up to 440 °C was observed.

Further heating up to 520 °C caused significant recovery and possibly even the initial stage of recrystallization and/or grain growth. These processes are responsible for significant decrease in microhardness. Heating up to 640 °C caused the complete recovery and significant grain growth. These processes were apparently detected by in-situ measurement of electrical resistance. The results proved that high sensitivity in-situ measurement of electrical resistance is capable of detecting recovery and/or recrystallization processes in temperature regions that are decisive for microstructure stability of UFG CP Ti.

4.4. Microstructural changes studied by SEM in Ti–6Al–7Nb

The comparison of resistance measurements and SEM observations is less convincing in Ti–6Al–7Nb alloy than in CP Ti. The microstructure remains unchanged in specimens heated up to 440 °C, which is consistent with resistance measurements. However, no obvious microstructure changes were observed in the specimen heated up to 550 °C, despite resistance evolution suggests that some microstructural transformation should occur. On the other hand, other authors reported the occurrence of some recovery process (identified by X-ray diffraction) and even the beginning of recrystallization (observed by TEM) in Ti–6A–7Nb alloy prepared by ECAP and annealed at 500 °C for 1 h [31]. Our sample heated up to 550 °C was in fact exposed to temperatures above 500 °C only for 10 min. This relatively short time of exposure to temperatures above 500 °C might be insufficient for recovery process to be observed by SEM. Fig. 6d shows a partially recrystallized structure of the sample annealed up to 660 °C. It is consistent with resistance measurements and observations of the same UFG material annealed at 600 °C for 1 h [31]. Due to these facts, we believe that resistance measurement captured the recovery and recrystallization processes also in Ti–6Al–7Nb, despite the beginning of the process could not be unambiguously proven by SEM observations.

5. Summary

Microstructure changes and thermal stability in two ultrafine-grained materials (CP Ti Grade 4 and Ti–6Al–7Nb alloy) occurring during linear heating were investigated by SEM and correlated with in-situ electrical resistance variations and microhardness changes. The results of this study can be summarized as follows:

- In-situ electrical resistance measurements during linear heating revealed differences in resistance evolution between UFG (prepared by ECAP) and coarse-grained material of both CP Ti and Ti–6Al–7Nb alloy.
- The changes in electrical resistance evolution of UFG CP Ti were identified by SEM observations as recovery and/or recrystallization.
- According to electrical resistivity measurements, recovery processes in Ti–6Al–7Nb alloy occur in the similar temperature range, even if it is observed only at higher temperatures using SEM.
- ECAP processing significantly increased the hardness of both CP Ti and Ti6Al7Nb alloy. The recovery of the CP Ti material caused significant decrease in microhardness after annealing at temperatures around 500 °C.
- UFG structure of CP Ti and Ti–6Al–7Nb alloy is stable up to 440 °C.

Acknowledgment

This work was financially supported by the Czech Science Foundation under the project GB14-36566G. Partial financial support by the Czech Ministry of Education, Youth a Sports under the project Kontakt II LH12217 is also acknowledged. B. Hadzima acknowledges financial support by the European Regional Development Fund and Slovak State Budget under the project "Research Centre of the University of Žilina" with ITMS code 26220220183. P. Zháňal and K. Václavová also acknowledge financial support by the Student Project SVV-2015-260213.

References

[1] M. Geetha, A.K. Singh, R. Askomanani, A.K. Gugia, Ti based biomaterials, the ultimate choice for orthopaedic implants – review, Prog. Mater. Sci. 54 (2009)

397–425, http://dx.doi.org/10.1016/j.pmatsci.2008.06.004.
[2] M. Long, H.J. Rack, Titanium alloys in total joint replacement – a materials science perspective, Biomaterials 19 (1998) 1621, http://dx.doi.org/10.1016/S0142-9612(97)00146-4.
[3] C.N. Elias, M.A. Meyers, R.Z. Valiev, S.N. Monteiro, Ultrafine grained titanium for biomedical applications: an overview of performance, J. Mater. Res. Technol. 2 (4) (2013) 340–350 (October–December).
[4] G. Welsch, R. Boyer, E.W. Collings (Eds.), Materials Properties Handbook: Titanium Alloys, ASM International, 1993.
[5] E. Eisenbarth, D. Velten, M. Müller, R. Thull, J. Breme, Biocompatibility of β-stabilizing elements of titanium alloys, Biomaterials 25 (26) (2004) 5705–5713, http://dx.doi.org/10.1016/j.biomaterials.2004.01.021.
[6] J. Yu, Z.J. Zhao, L.X. Li, Corrosion fatigue resistances of surgical implant stainless steel and titanium alloys, Corros. Sci. 35 (1–4) (1993) 587–591, http://dx.doi.org/10.1016/0010-938X(93)90193-K 593-597, ISSN 0010-938X.
[7] R.Z. Valiev, R.K. Islamgaliev, I.V. Alexandrov, Bulk nanostructured materials from severe plastic deformation, Prog. Mater. Sci. 45 (2000) 103–189, http://dx.doi.org/10.1016/S0079-6425(99)00007-9.
[8] T.G. Langdon, Twenty-five years of ultrafine-grained materials: achieving exceptional properties through grain refinement, Acta Mater. 61 (2013) 7035–7059, http://dx.doi.org/10.1016/j.actamat.2013.08.018.
[9] V.V. Stolyarov, Y.T. Zhu, T.C. Lowe, R.K. Islamgaliev, R.Z. Valiev, A two-step SPD processing of ultrafine-grained titanium, NanoStruct. Mater. 11 (1999) 947–954, http://dx.doi.org/10.1016/S0965-9773(99)00384-0.
[10] R.K. Islamgaliev, V.I. Kazyhanov, L.I. Shestakova, A.V. Sharafutdinov, R. Z. Valiev, Microstructure and mechanical properties of titanium (Grade 4) processed by high-pressure torsion, Mater. Sci. Eng. A 493 (2008) 190–194, http://dx.doi.org/10.1016/j.msea.2007.08.084.
[11] Y.C. Wang, T.G. Langdon, Influence of phase volume fractions on the processing of a Ti–6Al–4V alloy by high-pressure torsion, Mater. Sci. Eng. A 559 (2013) 861–867, http://dx.doi.org/10.1016/j.msea.2012.09.034.
[12] L.R. Saitova, H.W. Hoppel, M. Goken, I.P. Semenova, R.Z. Valiev, Cyclic deformation behavior and fatigue lives of ultrafine-grained Ti–6Al–4V ELI alloy for medical use, Int. J. Fatigue 31 (2009) 322–331, http://dx.doi.org/10.1016/j.ijfatigue.2008.08.007.
[13] S. Zherebtsov, G. Salishchev, R. Galeyev, K. Maekawa, Mechanical properties of Ti–6Al–4V titanium alloy with submicrocrystalline structure produced by severe plastic deformation, Mater. Trans. 46 (2005) 2020–2025, http://dx.doi.org/10.2320/matertrans.46.2020.
[14] A.V. Polyakov, I.P. Semenova, R.Z. valiev, High fatigue strength and enhanced biocompatibility of UFG CP Ti for medical innovative applications, IOP Conf. Ser.: Mater. Sci. Eng. (2014), http://dx.doi.org/10.1088/1757-899X/63/1/012113.
[15] I.P. Semenova, G.I. Raab, L.R. Saitova, R.Z. Valiev, The effect of equal-channel angular pressing on the structure and mechanical behaviour of Ti–6Al–4V alloy, Mater. Sci. Eng. A 387–389 (2004) 805–808, http://dx.doi.org/10.1016/j.msea.2004.02.093.
[16] R.Z. Valiev, I.P. Semenova, E. Jakushina, V.V. Latysh, H. Rack, T.C. Lowe, J. Petruzelka, L. Dluhos, D. Hrusak, J. Sochova, Nanostructured SPD processed titanium for medical implants, Mater. Sci. Forum 584–586 (2008) 49–54, http://dx.doi.org/10.4028/www.scientific.net/MSF.584-586.49.
[17] H.S. Kim, S.J. Yoo, J.W. Ahn, D.H. Kim, W.J. Kim, Ultrafine grained titanium sheets with high strength and high corrosion resistance, Mater. Sci. Eng. A 528 (2011) 8479–8485, http://dx.doi.org/10.1016/j.msea.2011.07.074.
[18] C. Leyens, M. Peters, Titanium and Titanium Alloys, Wiley-VCH (2003), p. 2, http://dx.doi.org/10.1002/3527602119.
[19] M. Janeček, J. Stráský, J. Čížek, P. Harcuba, K. Václavová, V.V. Polyakova, I. P. Semenova, Mechanical properties and dislocation structure evolution in Ti6Al7Nb alloy processed by high pressure torsion, Metall. Mater. Trans. A 45A (2014) 7–15, http://dx.doi.org/10.4028/www.scientific.net/MSF.667-669.943.
[20] V.V. Polyakova, V.N. Anumalasetty, I.P. Semenova, R.Z. Valiev, Influence of UFG structure formation on mechanical and fatigue properties in Ti–6Al–7Nb alloy, IOP Conf. Ser.: Mater. Sci. Eng. (2014), http://dx.doi.org/10.1088/1757-899X/63/1/012162.
[21] M. Janeček, J. Čížek, J. Stráský, K. Václavová, P. Hruška, V. Polyakova, S. Gatina, I. Semenova, Microstructure evolution in solution treated Ti15Mo alloy processed by high pressure torsion, Mater. Charact. 98 (2014) 233–240, http://dx.doi.org/10.1016/j.matchar.2014.10.024.
[22] K.S. Suresh, N.P. Gurao, D.S. Singh, S. Suwas, K. Chattopadhyay, S.V. Zhrebtsov, G.A. Salishchev, Effect of equal channel angular pressing on grain refinement and texture evolution in a biomedical alloy Ti–13Nb–13Zr, Mater. Charact. 82 (2013) 73–85, http://dx.doi.org/10.1016/j.matchar.2013.05.003.
[23] Z.B. Zhang, Y.L. Hao, S.J. Li, R. Yang, Fatigue behavior of ultrafine-grained Ti–24Nb–4Zr–8Sn multifunctional biomedical titanium alloy, Mater. Sci. Eng. A 577 (2013) 225–233, http://dx.doi.org/10.1016/j.msea.2013.04.051.
[24] H. Yilmazer, M. Niiomi, M. Nakai, K. Cho, J. Hieda, Y. Todaka, T. Miyazaki, Mechanical properties of a medical β-type titanium alloys with a specific microstructural homogenization through high-pressure torsion, Mater. Sci. Eng. C 33 (2013) 2499–2507, http://dx.doi.org/10.1016/j.msec.2013.01.056.
[25] M. Hoseini, M.H. Pourian, F. Bridier, H. Vali, J.A. Szpunar, P. Bocher, Thermal stability and annealing behaviour of ultrafine grained commercially pure titanium, Mater. Sci. Eng. A 532 (2012) 58–63, http://dx.doi.org/10.1016/j.msea.2011.10.062.
[26] J. Freudenberg, A. Kaufmann, H. Klauss, T. Marr, K. Nenkov, V. Sarma Subramanya, L. Schultz, Studies on recrystallization of single-phase copper alloys by resistance measurements, Acta Mater. 58 (2010) 2324–2329, http://dx.doi.org/10.1016/j.actamat.2009.12.018.
[27] M. Liang, Y.F. Lu, L.F. Sun, X.Y. Yu, P.F. Wang, G.Q. Liu, C.S. Li, Investigation on recrystallization of Cu–Nb micro-composites by the method of resistance, Phys. Procedia 45 (2013) 105–108, http://dx.doi.org/10.1016/j.phpro.2013.04.063.
[28] K. Kazemi-choobi, J. Khalil-allafi, V. Abbasi-chianeh, Investigation of the recovery and recrystallization processes of Ni50.9Ti49.1 shape memory wires using in situ electrical resistance measurement, Mater. Sci. Eng. A 551 (2012) 122–127, http://dx.doi.org/10.1016/j.msea.2012.04.106.
[29] V.M. Segal, V.I. Reznikov, A.E. Drobyshevskiy, V.I. Koplyov, Plastic working of metals by simple shears, Russ. Metall. (1981) 99–105.
[30] K. Hajizadeh, B. Eghbali, K. Topolski, K.J. Kurzydlowski, Ultra-fine grained bulk CP-Ti processed by multi-pass ECAP at warm deformation region, Mater. Chem. Phys. 143 (2014) 1032–1038, http://dx.doi.org/10.1016/j.matchemphys.2013.11.001.
[31] V. Polyakova, I.P. Semenova, R.Z. Valiev, Influence of annealing on the structure and mechanical properties of ultrafine-grained alloy Ti–6Al–7Nb, processed by severe plastic deformation, Mater. Sci. Forum 667–669 (2010) 943–948, http://dx.doi.org/10.4028/www.scientific.net/MSF.667-669.943.
[32] M. Hájek, J. Veselý, M. Cieslar, Precision of electrical resistivity measurements, Mater. Sci. Eng. A 462 (1–2) (2007) 339–342, http://dx.doi.org/10.1016/j.msea.2006.01.175.
[33] A. Savitzky, M.J.E. Golay, Smoothing and differentiation of data by simplified least squares procedures, Anal. Chem. 36 (8) (1964) 1627–1639, http://dx.doi.org/10.1021/ac60214a047.
[34] M. Cormier, F. Claisse, Composition dependence of the thermal coefficient of electrical resistivity of c.p.h. titanium-oxygen alloys, J. Less Common Met. 48 (1976) 309–314, http://dx.doi.org/10.1016/0022-5088(76)90010-2.
[35] R.W. Powell, R.P. Tye, The thermal and electrical conductivity of titanium and its alloys, J. Less Common Met. 48 (1961) 309–314, http://dx.doi.org/10.1016/0022-5088(61)90064-9.
[36] S. Malinov, P. Markovsky, W. Sha, Z. Guo, Resistivity study and computer modelling of the isothermal transformation kinetics of Ti–6Al–4V and Ti–6Al–2Sn–4Zr–2Mo–0.08Si alloys, J. Alloy. Compd. 314 (2001) 181–192, http://dx.doi.org/10.1016/S0925-8388(00)01227-5.
[37] G. Welsch, G. Lütjering, K. Gazioglu, W. Bunk, Deformation characteristics of age hardened Ti–6Al–4V, Metall. Trans. A 8 (1977) 169–177, http://dx.doi.org/10.1007/BF02677278.
[38] S. Guo, Q. Meng, G. Liao, X. Zhao, Microstructural evolution and mechanical behaviour of metastable β-type Ti–25Nb2–Mo–4Sn alloy with high strength and low modulus, Prog. Nat. Sci.: Mater. 23 (2013) 174–182, http://dx.doi.org/10.1016/j.pnsc.2013.03.008.

Proceedings of the International Symposium on Physics of Materials (ISPMA13)

Phase Transformations in Ti–15Mo Investigated by *in situ* Electrical Resistance

P. Zháňal*, P. Harcuba, J. Šmilauerová, J. Stráský, M. Janeček, B. Smola, M. Hájek

Department of Physics of Materials, Charles University in Prague, Prague, Czech Republic

In this study phase transformations in metastable beta Ti–15Mo alloy were investigated by an *in situ* electrical resistance measurement in a wide range of temperatures from −196 °C to 850 °C. Different temperature ranges of the evolution of electrical resistance were correlated with underlying phase transformations. In the low temperature range, stage I (from −196 °C to 220 °C) the decrease of electrical resistance with increasing temperature is caused by the dissolution of ω_{ath} (formed during quenching by athermal shuffle transformation) which is accompanied by the relaxation of lattice strain, while the diffusional assisted growth of ω_{iso} in the range from 220 °C to 380 °C (stage II) is the main mechanism causing the increase of resistance. Another decrease of the resistance in the range from 380 °C to 550 °C (stage III) is explained by the dissolution or transformation of ω_{iso}. The increase of resistance above 550 °C (stage IV) is related to the growth of α-phase particles. The fully reversible character of ω_{ath} growth and dissolution during heating and cooling in the stage I up to 100 °C was confirmed by temperature cycling during repeated *in situ* resistance runs from RT. Pre-ageing of samples at 300 °C promotes the formation of ω_{iso} particles. Subsequently, ω_{ath} particles are not created, which is fully consistent with electrical resistance measurements. The presence of ω_{ath} and the orientation relationship between ω and β were identified by the electron diffraction.

DOI: 10.12693/APhysPolA.128.779

PACS: 64.70.kd

1. Introduction

Titanium and its alloys exhibit high specific strength, excellent corrosion resistance, and enhanced biocompatibility. Due to the low specific density, which is approximately half of that of steels and Ni-based superalloys, titanium alloys are successfully used in the aerospace, chemical industry and biomedicine. A wide range of application of titanium may be also found in other branches such as architecture, chemical processing, medicine, power generation, marine and offshore, sports and leisure, and transportation [1]. The only disadvantage, which hinders wider use of titanium, e.g. in automobile industry, is its comparatively high cost, which is caused by high processing costs. This paper presents a study of phase transformations, which occur in the metastable β-Ti alloy Ti–15Mo (titanium alloy with 15 wt% (8.1 at.%) of molybdenum). Ti–15Mo alloy was chosen for this experimental study, because it is designed for biomedical use [2], and represents a simple binary system that has been already widely investigated [3, 4] and undergoes several phase transformations. A detailed understanding of these transformations is of particular importance due to the impact of the resulting microstructures on the mechanical properties of the alloy.

Titanium is a polymorphic material. The high-temperature phase has the body-centered cubic structure and is referred to as β-phase. The ambient temperature phase has the hexagonal close-packed structure and is referred to as α-phase. Recently, the main interest focuses on development and investigation of the so-called metastable β alloys. These alloys contain sufficient amount of β-stabilizing elements such that β-phase can be retained at room temperature after quenching. The β-phase is in a metastable state and ultimately equilibrium $\alpha + \beta$ composition can be achieved by annealing treatment [5]. Several other structural phases can be found in metastable β-Ti alloys. In the investigated Ti–15Mo, the formation of ω-phase is an important process for controlling microstructure. The ω-phase has a hexagonal symmetry and is formed by a diffusionless shuffle transformation described in [6]. This phase is formed already during quenching and is referred to as ω_{ath} (ω athermal). The formed particles are coherent, few nanometers in diameter and considered to have the same chemical composition as the β-matrix [7]. Upon subsequent ageing (around 300 °C), ω particles become chemically stabilized by expelling β-stabilizing elements — Mo in the case of Ti–15Mo alloy. This phase is referred to as ω_{iso} (ω isothermal). Particles ω_{iso} grow during annealing and become more chemically stabilized — i.e. they differ from surrounding β-matrix in composition [8]. Upon further annealing (around 500 °C), α-phase particles precipitate. ω particles serve as preferential nucleation sites for α-phase particles precipitation and therefore the size and mainly the distribution of α-phase particles can be controlled by controlling the formation of ω-phase particles. The principal experimental method employed in the present study is the electrical

*corresponding author; e-mail: pavel.zhanal@mff.cuni.cz

resistance. It was shown that the electrical resistance is very sensitive to ω-phase evolution during heating [9].

The most related study to the present work identifies ω_{ath} dissolution, ω_{iso} formation and α precipitation by *in situ* electrical resistance measurements in a TIMET LCB titanium alloy [10]. The evolution of electrical resistivity in this alloy that undergoes similar consequent phase transitions is further discussed using more direct methods as transmission electron microscopy (TEM), X-ray diffraction (XRD) and neutron-diffraction [9, 11, 12]. Very similar Ti–12Mo alloy was investigated in [13].

2. Experimental

The metastable Ti–15Mo (with 15 wt% (8.1 at.%) of Mo) was used in this investigation. The material was sealed in a quartz tube and solution treated (ST) at 900 °C for 4 h and subsequently quenched in water.

The four-point method was employed for electrical resistivity measurements allowing simultaneous measurement of the voltage and the electrical current. The sample of approximate thickness of 1 mm and the size of 20 × 10 mm^2 is cut to a special shape to increase the effective length of the sample for current flow and four contacts are appropriately jointed. The sample is then placed in a specially designed furnace which allows precise heating of the sample in a protective argon atmosphere up to high temperatures as well as defined cooling back to room temperature. The cooling can be further extended to –200 °C (liquid nitrogen, LN). By utilizing Keithley 2182A nanovoltmeters we are able to achieve measurement with relative error better than 0.0001 within each measured point while obtaining about 2 points per second [14]. The evolution of relative resistivity (related to room temperature (RT) resistivity) can be evaluated from measured data.

Thin foils for TEM were prepared by mechanical grinding on fine emery papers to the thickness of 150 μm followed by ion polishing. TEM observations were performed on JEOL JEM 2000FX microscope at 200 kV.

3. Results and discussion

The presence of the ω-phase in the ST specimen was proved by TEM. The detailed inspection of electron diffraction patterns revealed the extra spots corresponding to the ω-phase [8] and confirmed the orientation relationship between the hexagonal ω and bcc grains [15], see Fig. 1:

$$[(111)_\beta \| (0001)_\omega$$
$$[110]_\beta \| [11\bar{2}0]_\omega$$

The evolution of electrical resistance was measured *in situ* during linear heating with the heating rate of 5 °C/min from RT to 850 °C. The result of this measurement is shown in Fig. 2. The solid line corresponds to the resistivity evolution. Dashed line is the first derivation of the same curve — computed numerically. Furthermore, the evolution of resistivity was also measured during cooling from room temperature to approximately –196 °C. This is illustrated in Fig. 2 by a dotted line. Several stages corresponding to the monotonous increase and/or decrease of the resistance can be identified during heating from RT. At low temperatures (RT–220 °C) — stage I — the decrease of electrical resistance with increasing temperature was observed. This can be attributed to the dissolution of ω_{ath}. In the vicinity of the coherent β/ω interface, the elastic strain field is formed which acts as the scattering zone for conducting electrons [16]. Therefore, during the dissolution of ω_{ath} phase particles, the elastic strain fields are released, which clears the matrix for electron drift. This leads to the decrease in conduction electron scattering and therefore to the resistance drops.

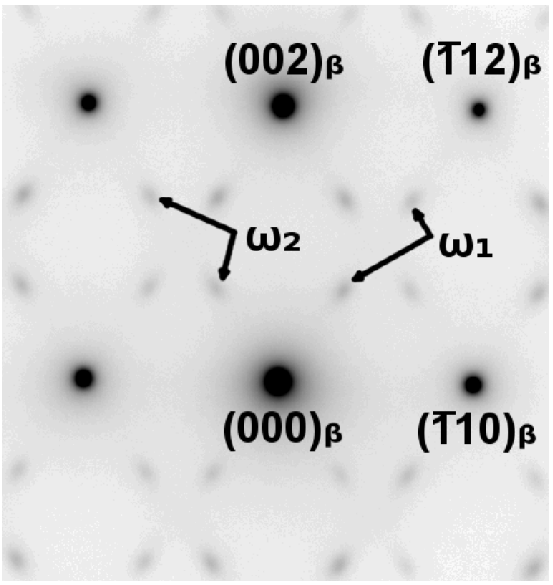

Fig. 1. TEM diffraction pattern of solution treated Ti–15Mo, showing the presence of two phases: β and ω.

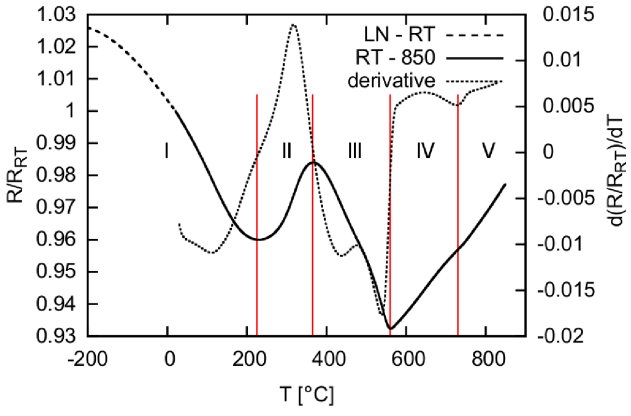

Fig. 2. The dependence of electrical resistance on temperature for ST sample and its derivative.

In stage II (220 °C–380 °C) the resistance increases

with increasing temperature. In this temperature range, particles, referred to as ω_{iso}, grow due to diffusion-driven chemical stabilization [7]. This process is accompanied by the increasing amount of β/ω interfaces, and therefore resistivity increases [13]. Note that resistivity also partly increases during heating due to lattice vibrations.

In stage III (380 °C–550 °C) the resistance declines with increasing temperature. The main reason is the decreasing volume fraction of semicoherent ω_{iso} particles. This can be caused either due to precipitation of α particles [13] (sometimes referred to as α-nano [10]) or simply by dissolution of ω_{iso} particles back to β matrix due to lower stability of the ω-phase in this temperature range [17].

The dissolution of ω particles can be also confirmed from dilatometry measurements [9]. In stage IV, the α-particles precipitate and grow directly in β-matrix [13] until the equilibrium volume fraction of α-phase is reached. The volume fraction of α-phase is decreasing towards the β-transus temperature that was found at 730 °C. This agrees well with the β-transus temperature given in the binary equilibrium phase diagram of Ti–Mo system [18].

The *in situ* measurement of electrical resistance of ST sample was extended to the cryogenic range from –196 °C to RT. As seen from left-hand side of Fig. 2 the resistance in the cryogenic range decreases with increasing temperature up to RT and merges smoothly the curve in stage I to 225 °C.

It is argued that even more ω_{ath} phase particles are formed during cooling from RT to –196 °C. The dissolution of these particles with increasing temperature causes the resistance decrease and even dominates over the common resistance increase with temperature due to lattice vibrations. Furthermore, it can be concluded that no α-phase particles are formed even at –196 °C. This proves that no α phase is created martensitically during cooling from RT to –196 °C in Ti–15Mo alloy.

Figure 2 also shows the derivative of the resistance evolution. The change of the slope in the resistance evolution as described above suggests that a new process already dominated over the previous one (e.g. more β/ω_{iso} interfaces are formed than β/ω_{ath} interfaces disappear). On the other hand, the onset of the new process can be identified as the peak of the first derivative. Therefore it can be concluded that ω particles become chemically stabilized already from 110 °C. Similarly the dissolution (or transformation) of ω_{iso} particles starts at 340 °C.

The minimum at the derivative of the resistivity curve in stage I (see Fig. 2) at around 110 °C also suggests that the resistance evolution up to this temperature should be reversible. This was indeed experimentally proven by cyclic repeated heating and cooling (heating/cooling rate of 5 °C/min) of the sample in a sequence up to 80, 90, and 100 °C. The results in Fig. 3 show that the lines for cooling and heating follow the same path and the resistance always returns to its original value. The minimum at the derivative of the resistivity curve (see Fig. 2) may be therefore considered as the limit of reversibility. Above this point ($T > 100$ °C) the diffusion controlled (thus irreversible) growth of ω phase resumes.

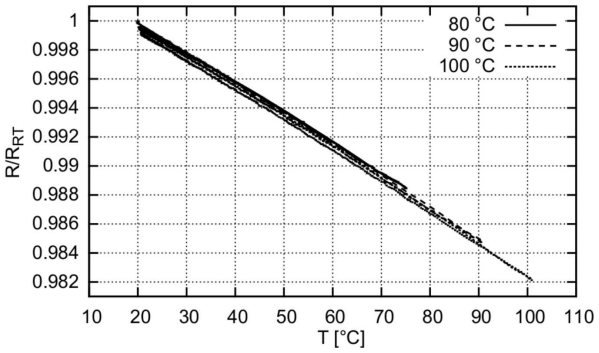

Fig. 3. The electrical resistance (normalized to R at RT) dependence on temperature during heating and cooling.

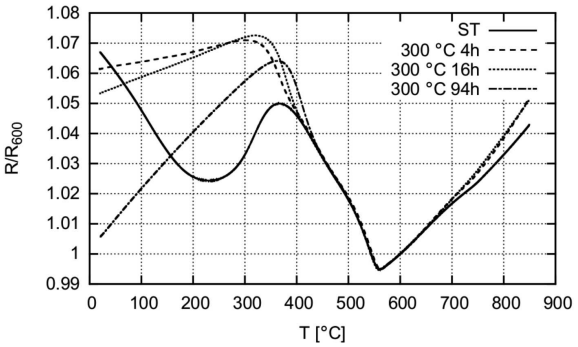

Fig. 4. The electrical resistance (normalized to R at 600 °C) dependence on temperature for samples aged at 300 °C for 4, 16, and 94 h compared with solution treated state.

We have already discussed that the course of resistivity curve in stage II is influenced by the growth of ω_{iso} phase and that this growth is irreversible. The slope of the resistivity curve at the stage II may be related to the transferred volume of ω_{iso}. In order to inspect this influence we have pre-aged solution treated specimens at 300 °C for 4, 16, and 94 h. These samples must differ in the volume fraction and in sizes of ω_{iso}. The resistivity curves measured in these specimens from RT to 850 °C are shown in Fig. 4. Note that since the microstructural conditions at room temperature are very different, it is more reasonable to normalize the relative resistance at temperature of 600 °C. At this temperature we assume similar microstructural condition in all samples, because the ω_{iso} particles created during pre-ageing are completely dissolved. As a result we can compare the different evolution in the lower temperature ranges.

For pre-aged samples we do not observe any resistivity decrease with increasing temperature. The ω_{ath} particles are obviously not formed in pre-aged samples that contain ω_{iso} particles. Furthermore, the decreasing slopes of these curves with increasing time of preaging in stage

II may be directly related to the increasing volume fraction of ω_{iso} after pre-ageing. The sample pre-aged for 94 h shows only slight increase of resistivity up to 350 °C. This means that either only very limited amount of ω_{iso} particles is formed or this increase can be attributed to common thermal increase of resistivity due to lattice vibrations.

4. Summary

The main results of the present work can be summarized as follows:

- The evolution of *in situ* resistivity of Ti–15Mo alloy was measured from –196 °C to 850 °C.
- During heating from room temperature, the temperature ranges of consequent processes can be identified, namely I: ω_{ath} particles dissolution, II: ω_{iso} particles formation, III: ω_{iso} particles dissolution, IV: α particles precipitation and finally V: α particles dissolution.
- Cooling to cryogenic temperatures showed that more ω_{ath} is created during cooling from RT. Furthermore, it is suggested that no α phase is created martensitically during cooling from RT to –196 °C in Ti–15Mo alloy.
- The dissolution of ω_{ath} is fully reversible below 110 °C.
- During pre-ageing at 300 °C the ω_{iso} particles are created. Therefore ω_{ath} are not created at room temperature, which is fully consistent with electrical resistance measurements. The longer the time of pre-ageing the lower the resistivity increase, because less ω_{iso} particles are created during *in situ* measurement.
- The resistance drop starting at approximately 350 °C is caused by dissolution or transformation of ω_{iso} particles.
- The β-transus was detected at 730 °C.

Acknowledgments

This work was financially supported by the Grant Agency of the Czech Republic under grant P107/12/1025. Pavel Zháňal acknowledges financial support by the grant SVV 2014-267303.

References

[1] C. Leyens, M. Peters, *Titanium and Titanium Alloys. Fundamentals and Applications*, Wiley-VCH, Weinheim 2003.

[2] J.R.S. Martins Jr., R.A. Nogueira, R.O. de Araújo, T.A.G. Donato, V.E. Arana-Chavez, A.P.R.A. Claro, J.C.S. Moraes, M.A.R. Buzalaf, C.R. Grandini, *Mater. Res.* **14**, 107 (2011).

[3] S. Banerjee, U.M. Naik, *Acta Mater.* **44**, 3667 (1996).

[4] S. Nag, R. Banerjee, H.L. Fraser, *Mater. Sci. Eng. C* **25**, 357 (2005).

[5] G. Lütjering, J.C. Williams, *Titanium*, Springer, 2003.

[6] D. de Fontaine, N.E. Paton, J.C. Williams, *Acta Metall.* **19**, 1153 (1971).

[7] H.P. Ng, A. Devaraj, S. Nag, C.J. Bettles, M. Gibson, H.L. Fraser, B.C. Muddle, R. Banerjee, *Acta Mater.* **59**, 2981 (2011).

[8] A. Devaraj, S. Nag, R. Srinivasan, R.E.A. Williams, S. Banerjee, R. Banerjee, H.L. Fraser, *Acta Mater.* **60**, 596 (2012).

[9] F. Prima, P. Vermaut, I. Thibon, D. Ansel, J. Debuigne, T. Gloriant, *J. Metastable Nanocryst. Mater.* **13**, 307 (2002).

[10] F. Prima, I. Thibon, D. Ansel, J. Debuigne, T. Gloriant, *Mater. Trans. JIM* **41**, 1092 (2000).

[11] F. Prima, P. Vermaut, G. Texier, D. Ansel, T. Gloriant, *Scr. Mater.* **54**, 645 (2006).

[12] T. Gloriant, G. Texier, F. Sun, I. Thibon, F. Prima, J.L. Soubeyroux, *Scr. Mater.* **58**, 271 (2008).

[13] F. Sun, F. Prima, T. Gloriant, *Mater. Sci. Eng. A* **527**, 4262 (2010).

[14] M. Hajek, J. Vesely, M. Cieslar, *Mater. Sci. Eng. A* **462**, 339 (2005).

[15] J.M. Silcock, M.H. Davies, K. Hardy, *The Mechanisms of Phase Transformations in Metals*, Vol. 18, Institute of Metals Monograph, 1955, p. 93.

[16] P.L. Rossiter, *The Electrical Resistivity of Metals and Alloys*, Cambridge Univ. Press, 1991.

[17] A. Devaraj, R.E.A. Williams, S. Nag, R. Srinivasan, H.L. Fraser, R. Banerjee, *Scr. Mater.* **61**, 701 (2009).

[18] S. Banerjee, P. Mukhopadhyay, *Phase Transformations Examples from Titanium and Zirconium Alloys*, Elsevier, 2007.

Microstructural Changes in β-Ti Alloy Investigated by Electrical Resistance

P. Zháňal, P. Harcuba, M. Hájek

Charles University, Faculty of Mathematics and Physics, Prague, Czech Republic.

Abstract. Evolution of electrical resistance of metastable β titanium alloy Ti-15Mo was measured *in-situ* during linear heating. It was shown that this method can be successfully used to detect phase transformations in studied alloys. The trend of electrical resistance changes at 225, 356 and 560 °C, which is connected to ω and α phase precipitation and dissolution in β phase matrix. Different heating rates were used to identify non-diffusional transformations which occur at the same temperature regardless of the heating rate. Differential scanning calorimetry measurement showed an abrupt change in heat capacity at 550 °C, which is associated with sudden dissolution of the ω phase as shown by scanning and transmission electron microscopy.

Introduction

Titanium and its alloys are known for their high specific strength and excellent corrosion resistance. These properties together with low specific density, which is approximately half of that of steels and Ni-based superalloys, allow successful employment in the aerospace and chemical industry. Moreover, a number of applications of titanium increases also in other markets such as architecture, chemical processing, medicine, power generation, marine and offshore, sports and leisure, and transportation [*Leyens and Peters*, 2003]. The main disadvantage, which hinders the wider use of titanium, is its relatively high cost which is caused by expensive production process. In present study phase transformations in metastable β-Ti alloy Ti-15Mo (titanium alloy with 15 wt. % (8.1 at. %) of molybdenum) were investigated during linear heating. Ti-15Mo has prospective biocompatible properties [*Martins Júnior et al.*, 2011]. Moreover, it represents a simple binary system which has been already investigated by different techniques [*Ho et al.*, 1999; *Ho*, 2008b].

Since titanium is a polymorphic material, phase formation depends on several conditions, such as temperature, pressure, amount of alloying elements and cooling rate. At room temperature, titanium crystallizes in a hexagonal close packed structure (hcp) referred to as α phase. Above 882 °C the structure transforms into a body-centered cubic (bcc) and is referred to as β phase.

Different phases can be formed in Ti alloys. Final microstructure and mechanical properties are strongly influenced by phase transitions. Thus their detailed investigation is very important.

Titanium alloys are divided into α, $\alpha + \beta$ and β alloys depending on type and amount of the alloying elements. Recently, there is great interest in the development and investigation of the so-called metastable β alloys. These alloys contain a sufficient amount of β-stabilizing elements for retention of β phase at room temperature after quenching (Mo in case of Ti-Mo alloys). Since, the β phase is in a metastable state ultimate equilibrium $\alpha+\beta$ composition can be achieved by annealing [*Gerd Lütjering*, 2007].

The formation of ω phase was explained by *Hickman* [1969]. His conclusions also apply for Ti-15Mo alloy. The ω phase can occur in two different modifications. The first one is the so-called athermal ω (ω_{ath}), which is formed upon quenching from the β phase by (diffusionless) shuffle transformation [*Fontaine et al.*, 1971]. The formed particles have a coherent interface with the β phase. They are several nanometers in diameter and have the same chemical composition as the β phase matrix [*Ng et al.*, 2011]. The second state of the ω phase, the so-called isothermal ω (ω_{iso}), grows during ageing at temperature range about 300–400 °C [*Sikka et al.*, 1982; *Šmilauerová et al.*, 2013]. The growth of ω_{iso} particles is a diffusion controlled process which is accompanied by a shift of lattice parameter of the β phase. Thus, an enrichment of the β phase with alloying elements is observed [*Devaraj et al.*, 2012]. Both modifications of the ω phase have the same hexagonal elementary cell and the terms athermal and isothermal are used to describe the thermal conditions upon which the ω phase forms.

The ω phase was observed in several alloys during deformation. The pressure aids the formation of the ω phase and extends the range of compositions in which the ω phase is observed [*Bagaryatskiy et al.*, 1958; *Kuan et al.*, 1975].

The over-ageing of $\omega + \beta$ results in α phase precipitation. Different mechanisms have been proposed describing the role of ω particles in the nucleation of α precipitates.

Blackburn and Williams [1968] showed that when the critical misfit of the ω/β interface is exceeded, interfacial edge dislocations can be formed in $\langle 110 \rangle_\beta$ directions. The formation of a dislocation is then followed by nucleation of an α rod-shape precipitate which lies in the same orientation as the corresponding dislocation. The nucleation at the dislocation or its proximity occurs due to stress fields induced by the dislocation. Thus, ageing results in a growth of the α phase at the expense of the ω phase.

There are also two different models of $\omega \rightarrow \alpha$ transformation in the systems with a lower ω/β misfit [*Nag et al.*, 2009]:

- The nucleation of α precipitates at certain distance from the ω/β interface is caused by local rejection of the ω destabilizers (i. e. α stabilizers) during the isothermal ageing.
- Displacive transformation within the core of the ω precipitates leads to the formation of α platelets. There is a strict orientation relationship at the α/ω interface which results in a perfect planar interface between the two phases, and the α phase is able to grow from the ω phase. *Prima et al.* [2006] showed two possible kinetics regimes and proposed a model explaining the nucleation and growth mechanism of the α phase.

Electrical resistance measurement was used for detection of phase transformations. This method is very sensitive to phase transitions in titanium alloys [*Prima et al.*, 2002].

Experimental

Material

Composition limits of the investigated metastable β titanium alloy Ti-15Mo are specified by a standard and are listed in Table 1. The material was solution treated (ST) at 900 °C for 4 hours and quenched in water. This condition also referred to as ST condition corresponds to the initial state for further investigation.

Table 1. Composition limits of the Ti-15Mo alloy [*Disegi*, 2009].

Element	Ni	C	H	Fe	O	Mo	Ti
Wt. %	<0.05	<0.1	<0.015	<0.1	<0.2	14.0–16.0	Balance

In-situ electrical resistance measurement and differential scanning calorimetry (DSC) were used to detect phase transformations. The kinetics of these transformations were determined using heating rates of 5 and 50 K/min. The evolution of phases was studied by scanning and transmission electron microscopy (SEM and TEM).

Electrical resistance measurement

The samples of the thickness of about 1 mm and of the dimensions 15×10 mm^2 were cut to a S shape to increase the effective length of the sample for current flow. In order to eliminate any deformation or contamination of the surface layer, approximately 0.2 mm was removed by grinding using grit SiC grinding papers.

Four-point method was used for measurements of electrical resistance. The voltage and electrical current were measured simultaneously using nanovoltmeter Keithley 2182 and SourceMeter Keithley 2400 device, respectively. The samples were placed in a specially designed furnace which allows precise heating of the sample in a protective argon atmosphere. The relative error of such measurement is lower than 10^{-4} within each measured point and two experimental values are acquired per second [*Hájek et al.*, 2007]. The evolution of electrical resistance during heating was measured from room temperature to 850 °C.

Differential scanning calorimetry

DSC was carried out in a Netzsch DSC 404 Pegasus calorimeter using specimens of about 30 mg of weight. Samples were put into Pt pans with Al_2O_3 liner inside. Measurements were performed in an argon atmosphere with the flow rate of ∼40 ml min^{-1} to avoid oxidation. The reference baseline was measured with empty pans. Data were collected in temperature ranges from room temperature up to 750 °C and 700 °C for the heating rate 5 K/min and 50 K/min, respectively.

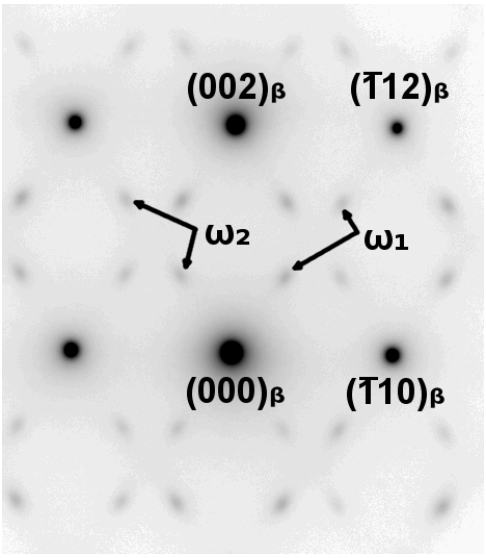

Figure 1. TEM diffraction pattern of ST Ti-15Mo, showing the presence of the β and the ω phase.

Scanning electron microscopy

The samples for SEM were polished by grinding papers. Vibratory polisher employing 0.3 µm and 0.05 µm aqueous alumina suspensions (Al_2O_3) and 0.05 µm colloidal silica or ion polishing was applied for final polishing. The samples were studied using FEI QUANTA 200 FEG and Zeiss Auriga Compact electron microscopes.

Transmission electron microscopy

Thin foils for TEM were prepared by mechanical grinding with fine emery papers to the thickness of 150 µm followed by ion polishing using Gatan PIPS device. TEM observations were performed on JEOL JEM 2000FX microscope at 200 kV.

Results and discussion

The presence of the ω_{ath} in the ST sample was investigated by TEM. The diffraction pattern of ST sample is shown in Fig. 1. The less intense reflections correspond to two different crystallographic orientations of the ω phase [*Devaraj et al.*, 2012]. Diffraction pattern in Fig. 1 confirms the presence of ω_{ath} phase and also indicates the orientation relationship between the β and the ω phase [*Banerjee and Mukhopadhyay*, 2007].

$$(111)_\beta \parallel (0001)_\omega$$
$$[110]_\beta \parallel [11\bar{2}0]_\omega$$

It was shown by *Schryvers and Tanner* [1991] that ω_{ath} particles have elipsoidal shape and are smaller than 1.5 nm (in length).

In Figures 2 and 3, the temperature dependence of electrical resistance (normalized by the value of the resistance of the sample at room temperature), its derivative with respect to temperature and DSC measurement during heating of ST sample at the rates of 5 K/min and 50 K/min are shown, respectively. Note that vertical axis for the derivative of resistivity is not shown since we are interested only in positions of local extremes. The zero value for the derivative is drawn as thin black line.

Fig. 2 shows that the electrical resistance curve changes its trend at 225 °C, 356 °C and 560 °C during heating. This result is in an agreement with earlier studies on Ti alloys [*Prima et al.*, 2000]. The change of monotonicity of resistance indicates that new transformation (scattering mechanism) prevails over previous one. The first derivative of resistance curve allows to determine the temperature range of the respective phase transformations. DSC curve has peaks at 340 °C and 420 °C. The curve has minimum at 550 °C. The transformations detected corresponding to the peaks at 340 and 420 °C are exothermic. The step change at 550 °C indicates abrupt change of heat capacity capacity of the material.

One can see, that the derivative of R and the DSC curve have local extremes at similar values of temperature. However, they are shifted in temperature with respect to each other. It is apparent at

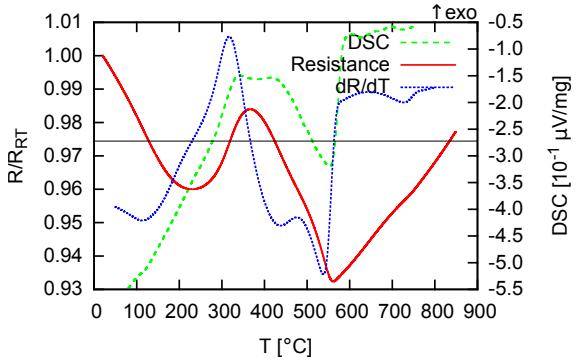

Figure 2. The temperature dependence of electrical resistance at the heating rate of 5 K/min and a corresponding DSC curve of ST sample.

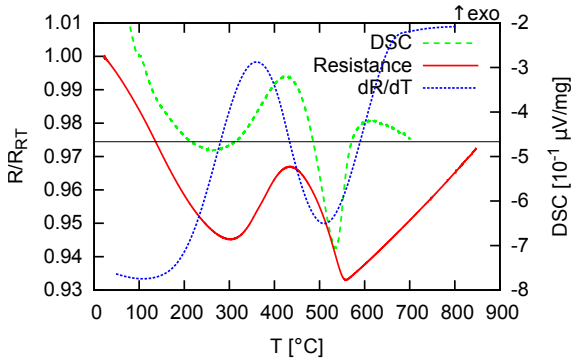

Figure 3. The temperature dependence of electrical resistance at the heating rate of 50 K/min and a corresponding DSC curve of ST sample.

temperatures about 340 and 550 °C. The difference is probably caused by the fact that each method detects changes in various thermodynamics quantities.

In order to compare transformation kinetics different heating rates were used. Fig. 3 shows a comparison of temperature dependence of electrical resistance and DSC curve of the ST sample during heating with 50 K/min rate.

The first two local extremes of resistance curve are shifted to higher temperatures (300 and 435 °C). Also the two transformations detected by DSC for the slower heating rate as two small peaks now overlap, which results in one peak with maximum at 430 °C. It may be assumed that the processes which cause these changes are thermally activated phase transformations of the first order. On the other hand, the process which causes the abrupt change of both resistance and the DSC values occurs at the same temperature for different heating rates. It means, that a phase transformation of second order occurs at around 550 °C. The initial decrease of DSC values (up to cca 250 °C) is caused by inability of apparatus to immediately achieve the high heating rate.

According to *Ho and Collings* [1972]; *Rossiter* [1991] the initial anomalous decrease of electrical resistance with increasing temperature is related to the dissolution of the ω_{ath} phase, which is formed from the β phase by a shuffle transformation during cooling. This transformation is fully reversible up to approximately 110 °C. The dissolution of ω_{ath} phase is accompanied by the decrease of the materials resistivity.

Significant increase of the electrical resistance is observed between 225 and 356 °C for heating rate of 5 K/min and between 300 and 430 °C for heating rate of 50 K/min. It is not caused only by thermal vibrations, which increase resistivity of a material with increasing temperature, but also by the formation of the ω_{iso} phase. Increasing resistivity values correspond to the interface bonds between the β matrix and the coherent ω precipitates [*Prima et al.*, 2000; *Ho and Collings*, 1972].

The decrease of resistance of sample between 356 and 560 °C for lower heating rate might be caused by the growth of ω particles which is accompanied by the rejection of β-stabilizing molybdenum from these particles and the loss of coherency. This mechanism originally described for Al alloys by Gunier–Preston [*Pollock*, 1993] operates also in our alloy. In addition, the growth of α phase starts preferentially from grain boundaries. Fig. 4 shows the microstructure of the material heated up to 550 °C (with heating

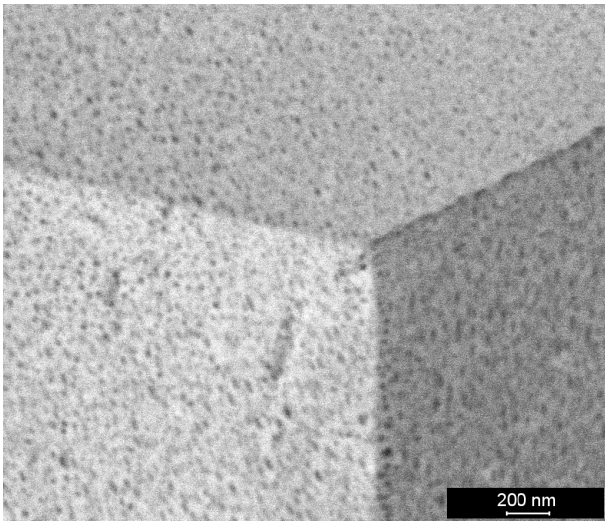

Figure 4. SEM micrograph of sample quenched from 550 °C.

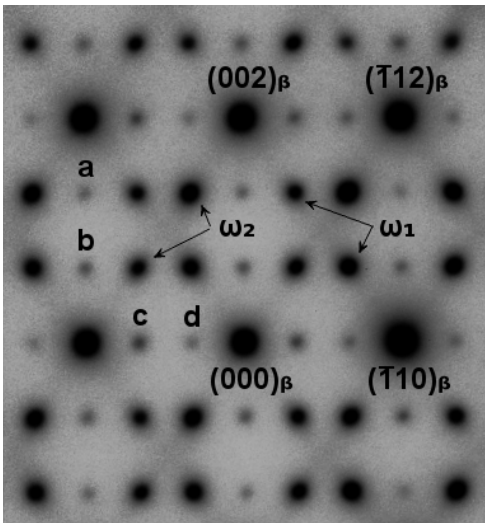

Figure 5. TEM diffraction pattern of sample quenched from 550 °C, showing the presence of the β and ω phase.

rate of 5 K/min) and quenched into water. The black dots indicate grown ω particles. Their presence was confirmed by TEM diffraction and is shown in Fig. 5. Diffractions from the ω phase in Fig. 4 are much more distinct than in Fig. 1. This is caused by larger ω particles, which are about 40 nm in diameter as can be seen in Fig. 4. The extra reflections marked as "a, b, c ,d" in Fig. 5 are the result of the double diffraction [*Ho*, 2008a].

In order to thoroughly investigate the process occurring at around 550 °C, which does not depend on heating rate (see Fig. 2 and 3), the ST samples were also heated up to 580 °C with heating rate 5 K/min and then quenched into water. SEM micrograph of the material is shown in Fig. 6. In this figure the rod-like α precipitates are presented. The absence of the ω particles is caused by their dissolution at temperatures between 550 and 580 °C. The abrupt dissolution of ω_{iso} causes the reversal of the trend in resistivity measurements and sudden change in thermal capacity. Both measured effects are heating rate independent, which suggests that the ω_{iso} dissolution is not driven by diffusion and does not consume any latent heat. Despite the ω_{ath} particles appear again during quenching, they are not visible since they do not give any contrast and are too small to be seen in SEM.

Summary

The evolution of electrical resistance was measured *in-situ* from RT up to 850 °C.
DSC measurement was carried out from RT up to 750 or 700 °C (for high heating rate).

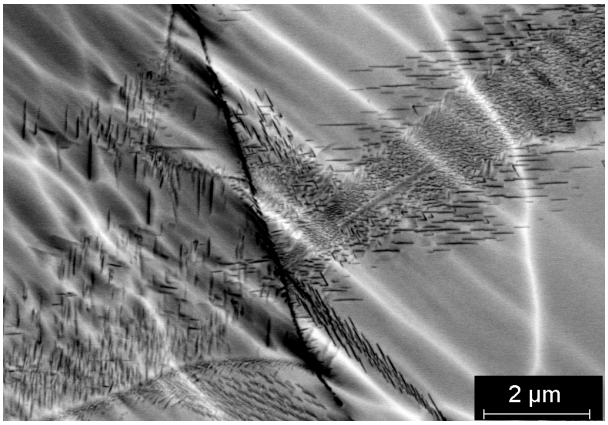

Figure 6. SEM micrograph of sample quenched from 580 °C.

The main results of the present work can be summarized as follows:

- During the heating from RT several ongoing processes were detected and identified, namely:
  1. ω_{ath} particles dissolution (which causes the decrease of resistance up to 225 °C).
  2. The growth of coherent ω_{iso} particles (together with thermal vibrations) causing the increase of resistance from 225 up to 356 °C).
  3. Loss of coherency of ω_{iso} particles and precipitation of α phase (resulting in the decrease of resistance in between 356 and 560 °C).
  4. Complete dissolution of ω phase, causing the abrupt change in resistance and in DSC curve at around 550 °C.
- The starting temperatures of phase transformations described in points 1–3 strongly depend on the heating rate. Higher heating rate shifts the temperatures to the higher values.
- Complete dissolution of the ω phase does not depend on the heating rate and always occurs at the same temperature. This transformation does not consume any latent heat and is accompanied by abrupt change of heat capacity.

Acknowledgment. This work was financially supported by the Czech Science Foundation under the project GB14-36566G. Pavel Zháňal acknowledges financial support by SVV (project no. SVV-2015-260213).

References

Bagaryatskiy, Y. A., Tagunova, T. V., and Nosova, G. I., *Problemy Metallovedenija i Fisiki Metallov*, *5*, 210, 1958.

Banerjee, S. and Mukhopadhyay, P., *Phase Transformations Examples from Titanium and Zirconium Alloys*, vol. 12 of *Pergamon Materials Series*, Pergamon, 2007.

Blackburn, M. and Williams, J., Phase transformations in Ti–Mo and Ti–V alloys, *Transactions of the Metallurgical Society of AIME*, *242*, 1968.

Devaraj, A., Nag, S., Srinivasan, R., Williams, R., Banerjee, S., Banerjee, R., and Fraser, H., Experimental evidence of concurrent compositional and structural instabilities leading to ω precipitation in titanium–molybdenum alloys, *Acta Materialia*, *60*, 596–609, 2012.

Disegi, J., *Implant Materials. Wrought Titanium –15% Molybdenum*, Synthes, 2009.

Fontaine, D. D., Paton, N., and Williams, J., The omega phase transformation in titanium alloys as an example of displacement controlled reactions, *Acta Metallurgica*, *19*, 1153–1162, 1971.

Gerd Lütjering, J. C. W., *Titanium*, Springer Berlin Heidelberg, 2007.

Hickman, B., The formation of omega phase in titanium and zirconium alloys: A review, *Journal of Materials Science*, *4*, 554–563, 1969.

Hájek, M., Veselý, J., and Cieslar, M., Precision of electrical resistivity measurements, *Materials Science and Engineering: A*, *462*, 339–342, international Symposium on Physics of Materials, 2005, 2007.

Ho, J. C. and Collings, E. W., Anomalous electrical resistivity in titanium-molybdenum alloys, *Phys. Rev. B*, *6*, 3727–3738, 1972.

Ho, W., Effect of omega phase on mechanical properties of Ti-Mo alloys for biomedical applications, *Journal of Medical and Biological Engineering*, *28*, 47–51, 2008a.

Ho, W., Ju, C., and Lin, J. C., Structure and properties of cast binary Ti–Mo alloys, *Biomaterials*, *20*, 2115–2122, 1999.

Ho, W. F., A comparison of tensile properties and corrosion behavior of cast Ti–7.5Mo with c.p. Ti, Ti–15Mo and Ti–6Al–4V alloys, *Journal of Alloys and Compounds*, *464*, 580–583, 2008b.

Kuan, T., Ahrens, R., and Sass, S., The stress-induced omega phase transformation in Ti-V alloys, *Metallurgical Transactions A*, *6*, 1767–1774, 1975.

Leyens, C. and Peters, M., *Titanium and Titanium Alloys: Fundamentals and applications*, Wiley-VCH Verlag GmbH & Co. KGaA, 2003.

Martins Júnior, J. R. S., Nogueira, R. A., Araújo, R. O. d., Donato, T. A. G., Arana-Chavez, V. E., Claro, A. P. R. A., Moraes, J. C. S., Buzalaf, M. A. R., and Grandini, C. R., Preparation and characterization of Ti-15Mo alloy used as biomaterial, *Materials Research*, pp. 107–112, 2011.

Šmilauerová, J., Janeček, M., Harcuba, P., and Stráský, J., Ageing study of timetal lcb titanium alloy, in *METAL 2013 - 22nd International Conference on Metallurgy and Materials, Conference Proceedings*, pp. 1592–1596, 2013.

Nag, S., Banerjee, R., Srinivasan, R., Hwang, J., Harper, M., and Fraser, H., ω-assisted nucleation and growth of α precipitates in the Ti–5Al–5Mo–5V–3Cr–0.5Fe β titanium alloy, *Acta Materialia*, *57*, 2136–2147, 2009.

Ng, H., Devaraj, A., Nag, S., Bettles, C., Gibson, M., Fraser, H., Muddle, B., and Banerjee, R., Phase separation and formation of omega phase in the beta matrix of a Ti–V–Cu alloy, *Acta Materialia*, *59*, 2981–2991, 2011.

Pollock, D. D., *Physical properties of materials for engineers*, CRC press, 1993.

Prima, F., Vermaut, P., Ansel, D., and Debuigne, J., ω precipitation in a beta metastable titanium alloy, resistometric study, *Materials Transactions, JIM*, *41*, 1092–1097, 2000.

Prima, F., Vermaut, P., Thibon, I., Ansel, D., Debuigne, J., and Gloriant, T., Nanostructured metastable β-titanium based alloy, *Journal of Metastable and Nanocrystalline Materials*, *13*, 307–314, 2002.

Prima, F., Vermaut, P., Texier, G., Ansel, D., and Gloriant, T., Evidence of α-nanophase heterogeneous nucleation from ω particles in a β-metastable Ti-based alloy by high-resolution electron microscopy, *Scripta Materialia*, *54*, 645–648, 2006.

Rossiter, P. L., *The electrical resistivity of metals and alloys*, Cambridge University Press, 1991.

Schryvers, D. and Tanner, L., High resolution electron microscopy observations of athermal omega phase in Ti-Mo alloys, *Materials Science Forum*, *56–58*, 329–334, 1991.

Sikka, S., Vohra, Y., and Chidambaram, R., Omega phase in materials, *Progress in Materials Science*, *27*, 245–310, 1982.